

An X-ray Search for the Missing Population of Period-Bounce Cataclysmic Variables

Dissertation

der Mathematisch-Naturwissenschaftlichen Fakultät
der Eberhard Karls Universität Tübingen
zur Erlangung des Grades eines
Doktors der Naturwissenschaften
(Dr. rer. nat.)

vorgelegt von
Daniela Muñoz Giraldo
aus Bogota/Kolumbien

Tübingen
2024

Gedruckt mit Genehmigung der Mathematisch-Naturwissenschaftlichen Fakultät der
Eberhard Karls Universität Tübingen.

Tag der mündlichen Qualifikation:

06.12.2024

Dekan:

Prof. Dr. Thilo Stehle

1. Berichterstatter/-in:

Prof. Dr. Beate Stelzer

2. Berichterstatter/-in:

Prof. Dr. Andrea Santangelo

Zusammenfassung

Kataklysmische Veränderliche sind wechselwirkende Doppelsterne, die aus einem Weißen Zwerg bestehen, der Masse von einem massearmen Begleiter akkretiert. Solche Systeme entwickeln sich durch Verlust an Drehimpuls von langen zu kurzen Umlaufzeiten. Kurzperiodische kataklysmische Veränderliche mit einem Braunen Zwerg als Begleiter stellen das letzte Stadium in der Entwicklung dieser Objektklasse dar. In kurzperiodischen Systemen kann der Begleiter, aufgrund des kontinuierlichen Massenverlustes, das Wasserstoffbrennen nicht aufrechterhalten und entartet. Die Entartung des Begleiters kehrt die Entwicklung der Umlaufzeit in Richtung längerer Perioden um, weshalb solche Systeme auch als *Period-bouncers* bezeichnet werden. Populationsstudien zeigen, dass die Mehrheit der kataklysmischen Veränderlichen, zwischen 40 % und 80 %, als *Period-bouncers* vorhergesagt werden, aber nur 18 dieser Systeme wurden bisher beobachtet und sicher identifiziert. Das Hauptaugenmerk dieser Arbeit liegt auf der Entdeckung dieser fehlenden Population von *Period-bouncers*.

Die Detektion von *Period-bouncers* im Röntgenbereich ist nützlich zur Identifizierung dieses unterrepräsentierten Typs von kataklysmischen Veränderlichen, da die individuelle Röntgenemission sowohl von Weißen als auch von Braunen Zwergen unterhalb der Empfindlichkeit heutiger Instrumente liegt und somit einen Beweis für Akkretion im System liefert. Um die fehlende *Period-bouncer* Population zu identifizieren, wurde im Rahmen dieser Dissertation ein dreistufiger Ansatz verfolgt. Zunächst wurde eine detaillierte Röntgenuntersuchung einer kleinen Stichprobe von magnetischen *Period-bouncers* durchgeführt, die zum ersten Nachweis von *Period-bouncers* mit Hilfe des Extended ROentgen Survey with an Imaging Telescope Array (eROSITA) an Bord der Spektrum-Röntgen-Gamma-Mission (SRG) führte, wie in Muñoz-Giraldo et al. (2023) berichtet. Dabei wurden die spezifischen Röntgeneigenschaften dieser schwer fassbaren Klasse von kataklysmischen Veränderlichen bestimmt. Zweitens wurde ein Literaturkatalog der bekannten kataklysmischen Veränderlichen um den *period-bounce*, einschließlich der 18 bisher bekannten *period-bouncers*, zusammengestellt, um eine "Scorecard" zu erstellen, die jedem System eine Wahrscheinlichkeit zuweist, ein *Period-bouncer* zu sein, wie von Muñoz-Giraldo et al. (2024) berichtet. Die Röntgendaten der letzten Himmelsdurchmusterungen mit eROSITA wurden systematisch analysiert. Hierdurch wurden 12 neue *period-bouncers* bestätigt, was zu einem Anstieg der bekannten Population von *Period-bouncers* um $\sim 66\%$ führte. Nach der Bestätigung der neuen *Period-bouncers* aus dem letzten Schritt macht dieser Untertyp von kataklysmischen Veränderlichen immer noch nur $\sim 11\%$ der Gesamtpopulation aus. Im dritten Schritt wurde ein Katalog neuer *period-bounce* Kandidaten aus kühlen Weißen Zwergen mit eROSITA-Detektionen zusammengestellt, die mittels einer reduzierten Version der Scorecard identifiziert wurden. Die Bestätigung dieser *period-bounce* Kandidaten durch Folgeuntersuchungen könnte zur Entdeckung der fehlenden Population von *Period-bouncers* führen.

Abstract

Cataclysmic variables are interacting binaries composed of a white dwarf that is accreting mass from a low-mass donor, evolving from longer to shorter orbital periods through angular momentum loss. Short-period cataclysmic variables with brown dwarf donors represent the final stage in the evolution of cataclysmic variables. Due to continuous mass loss, the donor in these short-period systems can not sustain hydrogen burning and becomes degenerate. The degeneracy of the donor reverses the orbital period evolution back towards longer periods, where such systems are, therefore, dubbed period-bouncers. According to population studies, the majority of cataclysmic variables, between 40 % and 80 %, are predicted to be period-bouncers, however, only 18 of these systems have been observed and confidently identified so far. The main focus of this thesis is to uncover the missing population of period-bouncers in order to provide observational support to the evolutionary theories of cataclysmic variables. An X-ray detection of period-bouncers is a powerful tool in order to identify this under-represented sub-type of cataclysmic variables, as it provides proof of the accretion in the system as the individual X-ray emission coming from either the white dwarf or the brown dwarf is below the sensitivity of current instruments. In order to identify the missing population of period-bouncer a three-step approach was implemented. First, a detailed X-ray study of a pilot-sample of magnetic period-bouncers was performed, leading to the first ever detection of period-bouncers using the extended ROentgen Survey with an Imaging Telescope Array (eROSITA) onboard the Spektrum-Roentgen-Gamma spacecraft (SRG) reported by Muñoz-Giraldo et al. (2023). Hereby, specific X-ray characteristics of this elusive class of cataclysmic variables were established. Second, a literature catalog of known cataclysmic variables around the period-bounce was compiled, including the 18 previously known period-bouncers, in order to produce a “scorecard” reported by Muñoz-Giraldo et al. (2024) which assigns to each system the probability of being a period-bouncer. The X-ray data from the recent all-sky surveys carried out with eROSITA was systematically analysed to confirm 12 new period-bouncers, leading to a $\sim 66\%$ increase in the population of period-bouncers. After the confirmation of new period-bouncers from the last step this sub-type of cataclysmic variables still corresponds to only $\sim 11\%$ of the overall cataclysmic variable population. In the third step, a catalog of new period-bounce candidates was compiled from cool white dwarf candidates with an eROSITA detection that have a high likelihood of being a period-bouncer according to a “reduced” version of the scorecard. Confirmation from follow-up surveys of these period-bounce candidates could lead to the identification of the missing population of period-bouncers.

List of Publications

1. D. Muñoz-Giraldo, B. Stelzer, D. de Martino, and A. Schwobe, *New X-ray detections of magnetic period-bounce cataclysmic variables from XMM-Newton and SRG/eROSITA*, 2023, *Astronomy & Astrophysics*, Volume 676, A7.
2. D. Muñoz-Giraldo, B. Stelzer, and A. Schwobe, *Cataclysmic variables around the period-bounce: An eROSITA-enhanced multi-wavelength catalog*, 2024, *Astronomy & Astrophysics*, Volume 687, A305.

Nr.	Accepted publication	List of authors	Author position	Scientific ideas %	Data generation %	Analysis and interpretation %	Paper writing %
1	Yes	D. Muñoz-Giraldo B. Stelzer D. de Martino A. Schwobe	1	40	90	80	80
2	Yes	D. Muñoz-Giraldo B. Stelzer A. Schwobe	1	60	90	80	80

Contents

Zusammenfassung	IV
Abstract	v
List of Publications	vii
1. Introduction	2
1.1. Cataclysmic Variables	3
1.2. Evolution of Cataclysmic Variables	4
1.3. Magnetism in Cataclysmic Variables	7
1.3.1. Non-Magnetic Cataclysmic Variables	7
1.3.2. Magnetic Cataclysmic Variables	10
2. Period-Bounce Cataclysmic Variables	13
2.1. Observational Characteristics of Period-Bounce Cataclysmic Variables	13
2.2. Searching for Period-Bounce Cataclysmic Variables	18
3. X-ray Satellites, Detections, and Analysis	19
3.1. Historical Context	19
3.2. Satellites and Missions	20
3.2.1. <i>XMM-Newton</i>	20
3.2.2. SRG-eROSITA	23
3.3. Analysis of X-ray data	24
3.4. Population Outlook	27
4. Results and discussion	30
4.1. Study of a Pilot Sample of Period-Bounce Cataclysmic Variables in X-rays	30
4.1.1. Characterization of the Pilot Sample	31
4.1.2. <i>XMM-Newton</i> detections	35
4.1.3. SRG-eROSITA detections	37
4.2. Catalogue of Known Cataclysmic Variables Around the Period-bounce	39
4.2.1. Constructing the Catalog	39
4.2.2. Scorecard for Likelihood of Being a Period-Bouncer	40
4.2.3. SRG-eROSITA detections	45
4.3. Search for New Period-Bounce Cataclysmic Variables with eROSITA	51

4.4. Outlook	54
Bibliography	57
A. New Systems in the Catalog of Known Cataclysmic Variables Around the Period-Bounce	71
B. Published Papers	73

1. Introduction

Around a third of the bodies in the Milky Way are found in binary systems, which are known for being composed of two bodies that are gravitationally bound to and in orbit around each other. The study of binaries is an important part of astronomical research as it not only pertains to a considerable number of objects in our neighborhood, but they also represent an ideal laboratory to study different physical processes. If the binary system is what is referred to as a “interacting binary” the most important physical process occurring is mass accretion.

Accretion can occur through different mechanisms, but it typically involves a mass-gaining hot component and a mass-losing cold component (Nagae et al. 2004). Wind accretion is characteristic of systems like high mass X-ray binaries and symbiotic stars, where the mass-losing components are fast-rotating giants capable of expelling large amounts of mass through stellar winds (Shakura et al. 2014). A considerable amount of binaries are not able to fulfill or sustain these conditions, leading to Roche-lobe overflow being more commonly occurring. Roche-lobe overflow describes the loss of mass from the mass-losing secondary to a mass-gaining primary through the inner Lagrangian point due to the fact that the secondary is overflowing its Roche lobe (Fig. 1-1).

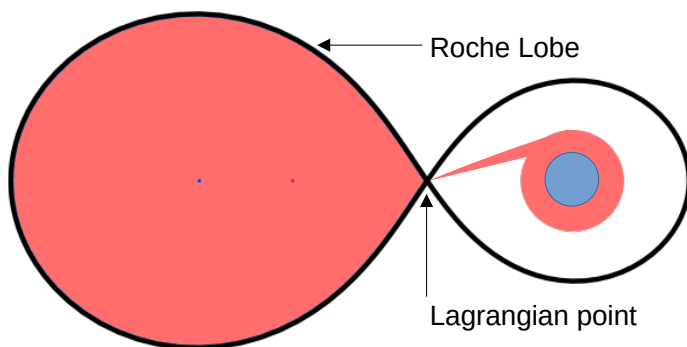


Figure 1-1.: Sketch of Roche-lobe overflow in a binary system. The mass-gaining primary is represented in blue, while the mass-losing secondary overflowing its Roche lobe and the mass transferred onto the mass-gaining primary are represented in light red.

The Roche-lobe is defined as a region of equal gravitational potential, formed around a component in a binary system, within which orbiting material is gravitationally bound to it. The critical region of equal gravitational potential, after which the orbiting material is no longer gravitationally bound to the component, intersects itself at the inner Lagrangian point of the system, forming a two-lobed structure with the two components at the center

of the two lobes. The Lagrange points are points of gravitational equilibrium, meaning that at this position the gravitational forces of the components in the binary and the centrifugal force balance each other. For all types of binaries, there are five Lagrange points (L_1 through L_5 in Fig. 1-2) located in the orbital plane of the two large bodies. L_1 , also known as the inner Lagrangian point, is where accretion occurs through.

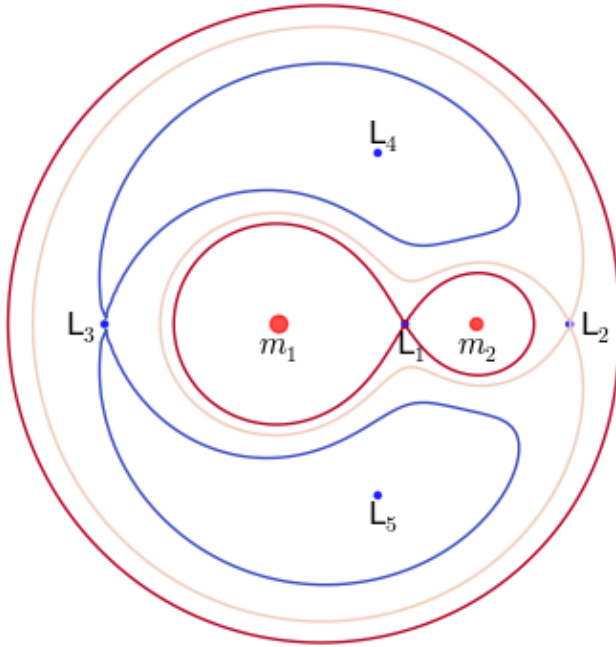


Figure 1-2.: Sketch of the location of the five Lagrange points in a binary system (Bannikova and Capaccioli 2022).

The overall shape of the Roche-lobe depends on parameters of the binary, specifically the mass ratio ($\epsilon = M_{\text{primary}}/M_{\text{secondary}}$) and the orbital separation of the binary (Eggleton 1983). A large binary mass ratio means that the Roche lobe of the secondary contracts rapidly as it loses mass, leading to large mass transfer rates (Temmink et al. 2023). On the other hand, in binaries with small mass ratios the Roche lobe of the secondary contracts slower as it loses mass leading to considerably smaller mass transfer rates.

1.1. Cataclysmic Variables

Cataclysmic variables are interacting compact binaries where a white dwarf, or primary, accretes matter from a late-type donor, or secondary (Warner 1995). This binary interaction occurs through accretion which can take place as wind accretion or Roche-lobe overflow, the latter being the most common in cataclysmic variables. Depending on various system parameters, most importantly the magnetism of the white dwarf, accretion in cataclysmic variables can form different structures like accretion disks or columns and hot-spots which will be discussed later in this section (Fig 1-1 shows a cataclysmic variable with an accretion disk).

According to Paczynski (1976), cataclysmic variables are the result of a common envelope phase in the evolution of a wide long-period binary (values range from 1AU to 6AU), where the envelope of a Roche-lobe filling, more massive primary star (typically a $\sim 2M_{\odot}$ red giant) expands beyond the outer Lagrangian point (L_2 in Fig. **1-2**) engulfing the secondary (usually a low mass main sequence star). The envelope is then ejected from the binary, leaving a post-common envelope binary composed by the evolved core of the primary (now a white dwarf) and a low mass companion still on the main-sequence as the secondary. At the end of the common envelope phase the orbital separation, and therefore the orbital period, of the binary system has been significantly reduced due to friction in the common envelope which extracts angular momentum and energy from the system. Once the binary separation is close enough to allow mass transfer from the secondary onto the white dwarf, the system morphs into a cataclysmic variable.

1.2. Evolution of Cataclysmic Variables

In terms of evolution, all cataclysmic variables follow a track from longer orbital periods towards shorter ones driven by angular momentum loss which causes the orbital separation, and therefore the orbital period, of the system to decrease (Paczynski 1976, Kolb 1993, Warner 1995). Figure **1-3** presents the results from the population synthesis study of cataclysmic variables by Goliaş and Nelson (2015), where the evolution of cataclysmic variables from longer orbital periods (top right corner) to shorter periods (bottom left corner) can be observed.

Angular momentum loss, the driving force in the evolution of cataclysmic variables, can occur via two mechanisms: magnetic wind braking and gravitational wave radiation. Magnetic wind braking arises from the stellar wind associated with the secondary’s magnetic activity (see e.g Mestel 1968, Verbunt and Zwaan 1981) which ejects material and angular momentum from the system. Gravitational wave radiation refers to the removal of angular momentum from the system via the emission of gravitational waves (Paczynski 1976). Presently, the individual contribution that each angular momentum loss mechanism has during the evolution of cataclysmic variables is still unclear, and a number of “recipes” describing different contributions have been suggested (Verbunt and Zwaan 1981, Rappaport et al. 1983, Kawaler 1988, Mestel and Spruit 1987, Andronov et al. 2003, Ivanova and Taam 2003, Irwin et al. 2007, Barnes and Kim 2010, Sarkar et al. 2024). The most commonly used recipe is referred to as the “standard model”, which will be used in the next few paragraphs to illustrate the evolution of cataclysmic variables.

Overall the evolution of cataclysmic variables can be divided in four stages. The first stage is known as the long-period regime ($P_{\text{orb}} > 3\text{h}$), which comprises systems that contain white dwarfs with effective temperatures of $\sim 20000\text{K}$ to $\sim 60000\text{K}$ (Knigge et al. 2011, Pala et al. 2022) and donors with spectral type from late G to early M (Giovannelli 2008, Knigge et al. 2011), with mass transfer rates typically ranging from $\sim 10^{-9}$ to $10^{-8} M_{\odot}/\text{yr}$ (Knigge et al.

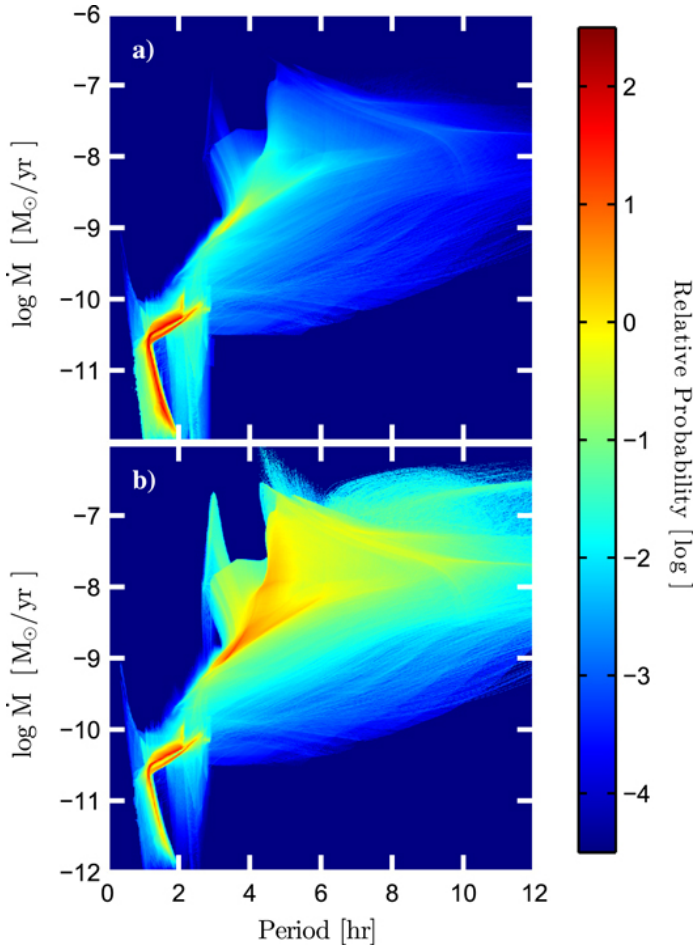


Figure 1-3.: Probability density of the population synthesis study of cataclysmic variables by Goliasch and Nelson (2015) in the orbital period versus mass transfer rate (\dot{M}) plane. **Upper panel:** Model intrinsic cataclysmic variable population. **Lower panel:** Model cataclysmic variable population scaled by the mass transfer rate to approximately take into account observational selection effects.

2011, Pala et al. 2022). The dominant angular momentum loss mechanism in the long-period regime according to the “standard model” is magnetic wind braking (Knigge et al. 2011).

At an orbital period of ~ 3 hours the donor becomes fully convective and, according to the “standard model”, magnetic wind braking abruptly stops leaving gravitational wave radiation as the only mechanism for angular momentum loss, which causes a reduced mass transfer rate in the system (King 1988, Ritter 1991, Schreiber et al. 2023). These changes lead to the donor no longer being bloated from mass loss, shrinking compared to its previous size. As a result the donor no longer fills its Roche-lobe, and therefore accretion stops in the system. This marks the beginning of the second stage in the evolution of cataclysmic variables known as the period-gap ($3\text{h} \lesssim P_{\text{orb}} \lesssim 2\text{h}$; grey band in Fig. 1-4). During this stage the system evolves as a detached binary until an orbital period of ~ 2 hours at which point the donor is once again able to fill its Roche-lobe allowing mass transfer to re-start in the system.

The re-start of accretion marks the beginning of the third stage in the evolution of a cataclysmic variable, known as the short-period regime ($2\text{h} \lesssim P_{\text{orb}} \lesssim 80\text{min}$). This stage is comprised of systems that contain white dwarfs with effective temperatures of $\sim 14000\text{K}$ to

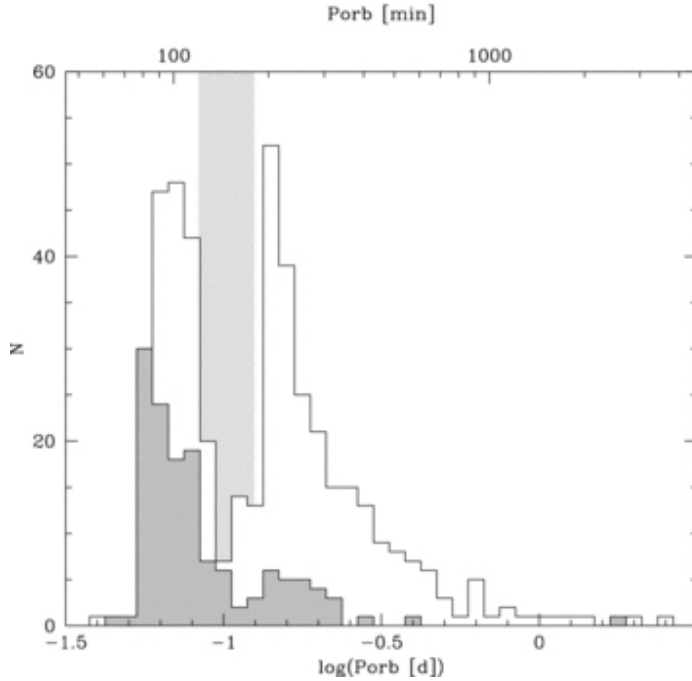


Figure 1-4.: The orbital period distribution compiled by Gänsicke et al. (2009) of: 454 cataclysmic variables from Ritter and Kolb (2003) which have no spectroscopic observation in SDSS DR6 (in white), and 137 SDSS-detected cataclysmic variables (in grey). The orbital period gap is marked as a grey band.

$\sim 20000\text{K}$ (Knigge et al. 2011, Pala et al. 2022) and donors with spectral type from early to late-M (Knigge et al. 2011), with mass transfer rates of $\sim 10^{-10} M_{\odot}/\text{yr}$ (Knigge et al. 2011, Pala et al. 2022). According to the “standard model” angular momentum losses in the short-period regime are taking place exclusively through gravitational wave radiation, specially considering that the donors in the system are expected to be fully convective and therefore have no significant magnetic field (Knigge et al. 2011).

At the period minimum, which is predicted to be located at $\simeq 65$ min, the donor is out of thermal equilibrium due to its mass loss timescale becoming much shorter than its thermal timescale (King 1988). Because the thermal timescale is defined as the timescale at which the star adjusts to structural changes, this means that the star is losing mass at a faster rate than it is able to adjust, causing it to fall out of thermal equilibrium. The donor, not being able to sustain hydrogen burning, becomes a brown dwarf (Howell et al. 2001). This change in internal structure, as the donor becomes degenerate and is characterized by a mass-radius relationship with a negative index, results in the donor no longer shrinking in response to mass-loss leading to an increase of the system’s orbital separation and consequently to the cataclysmic variable bouncing back towards longer orbital periods. The systems that go through this process of “bounce-back” to longer periods are known as period-bouncers (Patterson 1998). Population synthesis studies based on the “standard model” (like the one presented in Fig. 1-3) predict that period-bouncers make-up between 40 % and 80 % of the cataclysmic variables population.

Removal of angular momentum from a system has different efficiencies depending on the mechanism through which it takes place (Politano and Weiler 2006, Pala et al. 2022). Magnetic wind braking is a more efficient mechanism for angular momentum loss which leads to

a rapidly contracting Roche lobe resulting in the high mass accretion rates expected by the “standard model” in long-period cataclysmic variables (see Fig. 1-3). On the other hand, gravitational wave radiation is a less efficient mechanism for angular momentum loss, leading to a slowly contracting Roche lobe that keeps the mass accretion rates of systems below the period gap about one order of magnitude lower compared to those of long-period cataclysmic variables (see Fig. 1-3).

Apart from the “standard model” additional recipes like the “empirical model for consequential angular momentum loss” (eCAML; Schreiber et al. 2016) have been gaining popularity as they tend to address some of the discrepancies between observations and the standard evolutionary track of cataclysmic variables. The main issues that the “standard model” faces are: The theoretically predicted period minimum ($P_{\min} \simeq 65\text{min}$) is considerably shorter than the observed value ($P_{\min} \simeq 82\text{min}$; Gänsicke et al. 2009, Muñoz-Giraldo et al. 2024), the theoretically predicted large population of period-bouncers making up the majority of cataclysmic variables has not been observed, and the lack of magnetic fields in M dwarfs necessary to explain the abrupt stop of angular momentum losses through magnetic wind braking at the beginning of the period gap is at odds with the observed presence of magnetic fields in M dwarfs (Morin et al. 2008, Morin et al. 2010, Kochukhov 2021).

The evolution of cataclysmic variables is predicted by population models to slow down in the area approaching the period minimum as well as in the period-bounce area, which should lead to an accumulation of systems near the period minimum known as the “period minimum spike” (Paczynski and Sienkiewicz 1983, Howell et al. 2001, Rappaport et al. 1982, Kolb and Baraffe 1999). Early studies of cataclysmic variables failed at observing the “period minimum spike” (see in Fig. 1-4 the white population), with evidence supporting its existence only emerging with the Sloan Digital Sky Survey (SDSS) study of cataclysmic variables by Gänsicke et al. (2009) (see in Fig. 1-4 the grey population). It was suggested that earlier cataclysmic variable samples did not include a sufficient number of systems around the period minimum in order to distinguish it (Inight et al. 2023a), which is supported by the detection of the “period minimum spike” in more recent and comprehensive short-period cataclysmic variable samples like the one presented in this thesis (Muñoz-Giraldo et al. 2024).

1.3. Magnetism in Cataclysmic Variables

Cataclysmic variables can be divided into two main classes according to the magnetism of the white dwarf: non-magnetic and magnetic cataclysmic variables (see Fig. 1-5), with each of these classes having specific characteristics that are related to different accretion structures.

1.3.1. Non-Magnetic Cataclysmic Variables

The negligible magnetic field of the white dwarf in non-magnetic cataclysmic variables allows for accretion to occur through an accretion disk. Material leaving the donor has angular

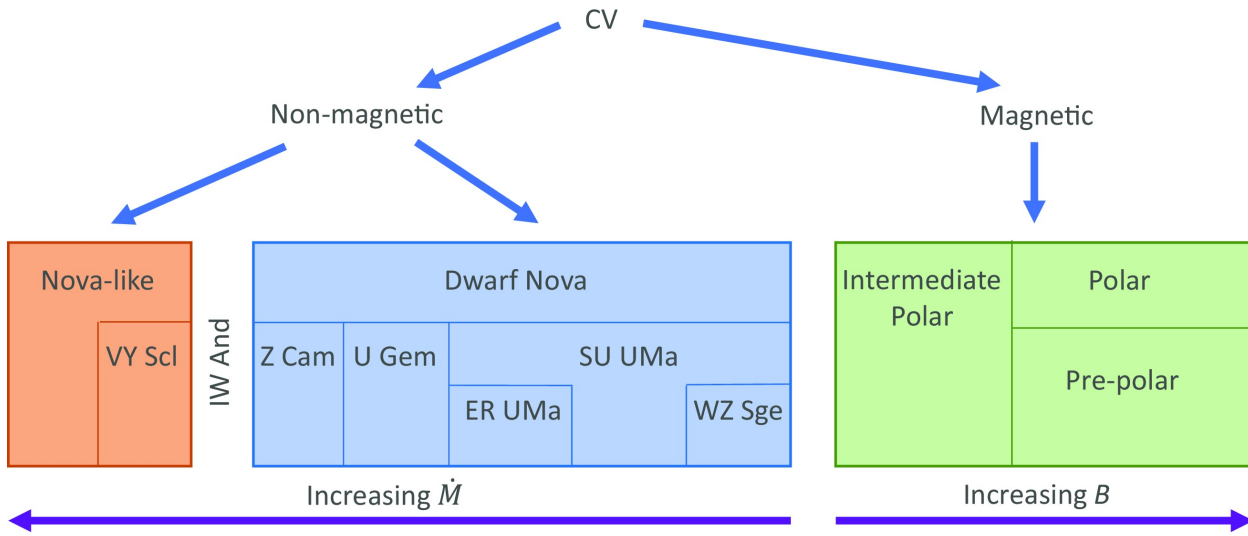


Figure 1-5.: Diagram depicting the classification of cataclysmic variables according to the magnetism of the white dwarf (Inight et al. 2023a). The physical parameters defining the boundaries between different sub-classes are mass accretion rate of the system (\dot{M}) and magnetic field strength of the white dwarf (B).

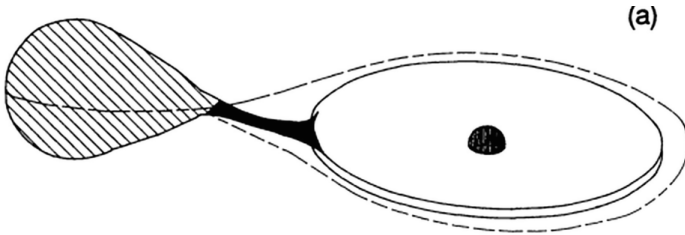


Figure 1-6.: Sketch of a non-magnetic cataclysmic variable with a full accretion disk (Norton 1993).

momentum from the binary motion meaning that accretion cannot take place in a straight line. Because of angular momentum conservation, as well as the fact that the binary is revolving around a common center of mass, the accreting matter from the donor goes into an orbit around the white dwarf forming an accretion disk (Fig. 1-6).

A wide number of observational behaviors, mainly dictated by the mass accretion rate present in the system, allow for the classification of non-magnetic cataclysmic variables into several sub-classes like classical novae, nova-like variables, and, the most relevant for this thesis, dwarf novae (Fig. 1-5).

Dwarf novae are characterized by the presence of an accretion disk around the white dwarf, and they can be observationally identified due to the quasi-periodic changes in brightness known as “outbursts” (Meyer and Meyer-Hofmeister 1984) and the significantly brighter “superoutbursts” (Fig. 1-7). A useful characteristic of “superoutbursts” in dwarf novae is that they are accompanied by the presence of “superhumps” which originate from donor-induced tidal dissipation of an eccentric accretion disk in a 3:1 orbital resonance (Whitehurst 1988, Osaki 1989). The period of these “superhumps”, which is expected to be a few percent

longer than the orbital period (Patterson et al. 2005a), has been established to scale with the mass ratio of the system ($q = M_{\text{donor}}/M_{\text{WD}}$), making it an useful tool to estimate the masses of the individual components in cataclysmic variables (Patterson et al. 2005a, Kato and Osaki 2013).

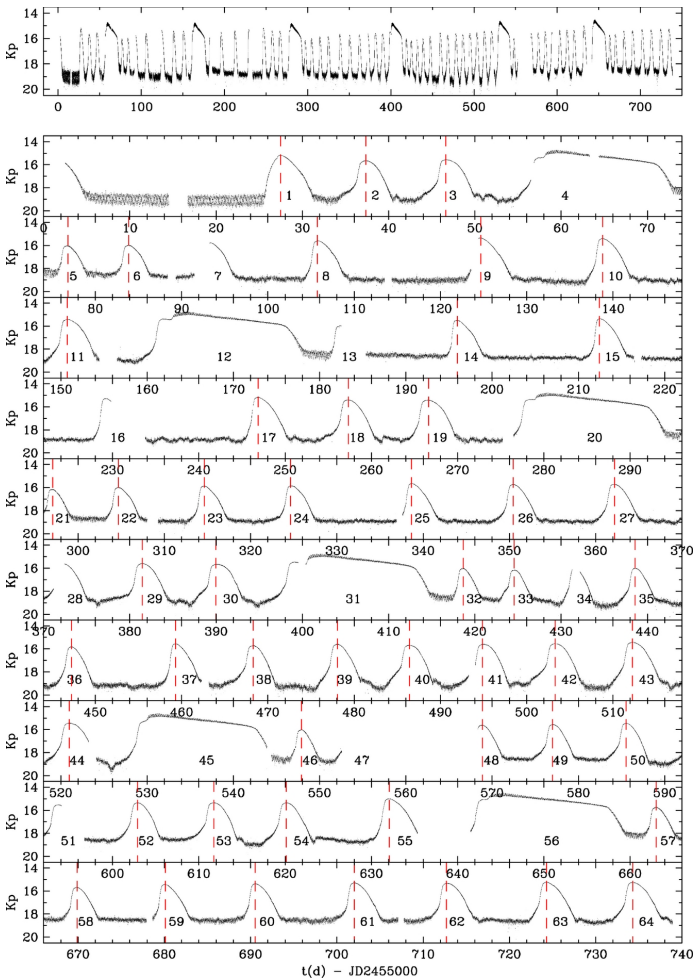


Figure 1-7.: Kepler light curve for SU UMa-type dwarf novae V344 Lyr, spanning 736 days. The light curve shows 6 “superoutbursts” and 58 “outbursts” (Canizso et al. 2012).

The behaviour of these “outbursts” and “superoutbursts” can be used to distinguish between different types of dwarf novae (Fig. 1-5). For this work, the focus is on the dwarf novae types composed by short-period systems closer to the period-bounce: the highly active ER UMa, the somewhat active SU UMa, and the scarcely active WZ Sge. ER UMa systems, commonly found just below the period gap, are characterized by having unusually short superoutburst recurrence times, leading them to spend more than a third of their time in this state (Inight et al. 2023a). SU UMa systems, which present occasional “superoutbursts”, are typically found below the period gap with donors that are usually M-type or later (Kato et al. 2009 and further papers in this series). WZ Sge systems are known for having extremely long outburst recurrence times (in the order of years to decades), very low mass accretion rates (in the order of $10^{-11}M_{\odot}/\text{yr}$) and low mass donors (Patterson et al. 2002, Kato 2015). WZ Sge-type cataclysmic variables usually have the shortest orbital periods of the whole non-

magnetic cataclysmic variable population with very low mass ratios, and have been suggested as harboring low mass donors consistent with being brown dwarfs (Kato 2022).

The majority of systems found in the “period minimum spike” have been classified as WZ Sge-type cataclysmic variables (Gänsicke et al. 2009), which might indicate that this population is a good starting point for finding new period-bounce candidates. However, WZ Sge-type objects have been detected primarily through photometric studies of optical superoutbursts in their light curves. While this can lead to the determination of the mass ratio of the system using the “superhump” method, it also means they are not easily observed in quiescence due to their faintness and, therefore, have remained largely undetected at other wavelengths. This lack of additional information makes a straightforward classification as a period-bouncer challenging, considering that a mass ratio consistent with the period-bounce area ($q \leq 0.078$; Kato 2022) should be supported by a spectroscopic detection of the very low-mass donor, or at least by multi-wavelength properties similar to what is expected of period-bouncers.

In non-magnetic cataclysmic variables, the area where the mass from the accretion disk settles onto the white dwarf is known as the boundary layer. The boundary layer, irregardless of the accretion rate presented by the cataclysmic variable, has an optically thin portion located near the top and bottom of the disk (dotted area in Fig. 1-8) which radiates a bremsstrahlung component observed as medium to hard ($kT \sim 2\text{-}100\text{ keV}$) X-rays (Patterson and Raymond 1985), and an optically thick portion located near the white dwarf (shaded area in Fig. 1-8) which radiates a blackbody component observed as soft ($0.1\text{-}2\text{ keV}$) X-rays (Patterson and Raymond 1985).

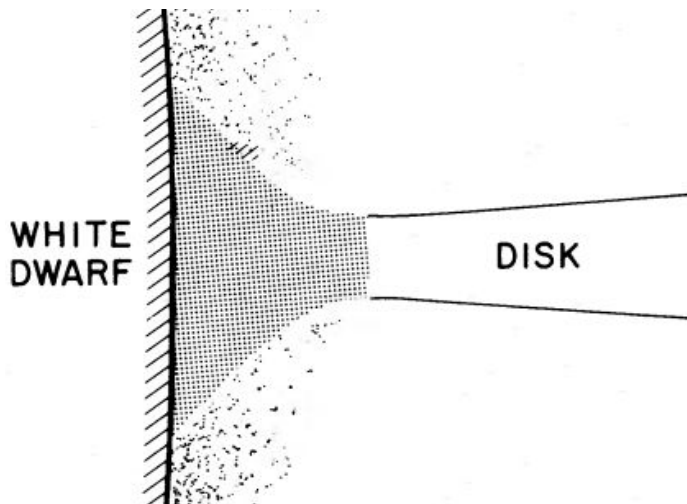


Figure 1-8.: Sketch of the boundary layer between the accretion disk and white dwarf in non-magnetic cataclysmic variables (Patterson and Raymond 1985). Dotted area of the boundary layer is optically thin while the shaded area of the boundary layer is optically thick.

1.3.2. Magnetic Cataclysmic Variables

Magnetic cataclysmic variables have a white dwarf that harbors a magnetic field, making up a population that has been estimated to be around one-third of cataclysmic variables (Wickramasinghe and Ferrario 2000, Pretorius et al. 2013, Pala et al. 2020). Depending on

the field strength they can be further divided into two sub-classes: if the white dwarf is weakly magnetized (characterized by magnetic field strengths $|B| \lesssim 10\text{MG}$) the magnetic cataclysmic variable is known as an intermediate polar, while magnetic cataclysmic variables with strongly magnetized white dwarfs (characterized by magnetic field strength $|B| \gtrsim 10\text{MG}$) are known as polars (Fig. 1-5).

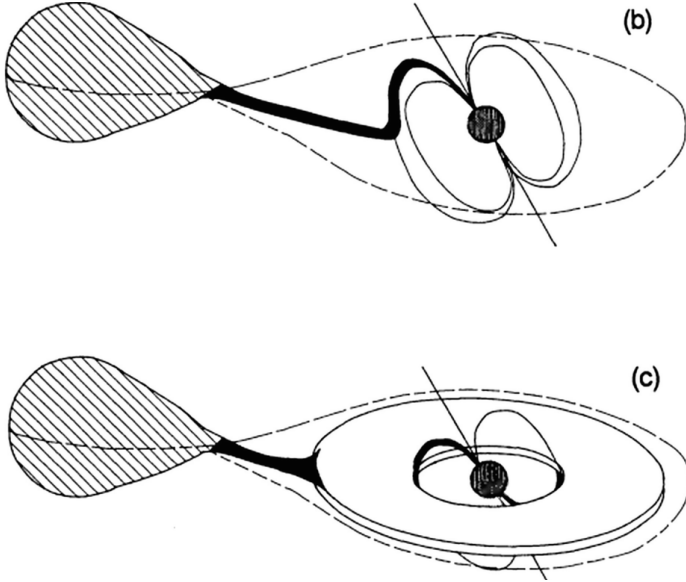


Figure 1-9.: Sketch of magnetic cataclysmic variables (Norton 1993). **Top panel:** A polar characterized by the lack of an accretion disk around the white dwarf. **Bottom panel:** An intermediate polar exhibiting an accretion disk interrupted by the weak magnetic field of the white dwarf.

In magnetic cataclysmic variables the accretion stream coming from the donor is directly affected by the field strength of the white dwarf. Intermediate polars, with their weakly magnetized white dwarfs, have an Alfvén radius, defined as the point after which the magnetic field of the white dwarf exerts negligible influence (Belenkaya et al. 2015), that is smaller than the circularization radius but greater than the white dwarf radius, leading to the formation of an accretion disk which is being disrupted at its inner region (Ulla et al. 1999; see Fig. 1-9). Material is captured in the inner region of the accretion disk and directly transported through the magnetic field lines to the surface of the white dwarf, specifically the magnetic poles, creating what is known as a hot-spot. Intermediate polars are found amongst long-period systems which have just recently started their evolution as cataclysmic variables meaning that the system did not have enough time to synchronize. This, together with the weak magnetic field of the white dwarf, result in intermediate polars where the rotating white dwarf is asynchronous with the binary orbital period ($P_{\text{spin}} \ll P_{\text{orb}}$).

On the other hand, polars, with their strongly magnetized white dwarfs, have an Alfvén radius that is greater than the circularization radius, preventing the formation of an accretion disk all-together (see Fig. 1-9). Material coming from the donor gets immediately captured and transported through the magnetic field lines straight to the magnetic poles of the white dwarf leading to the formation of a hot-spot (Ulla et al. 1999). Polars are found amongst short-period systems which are towards the end of their evolution as cataclysmic variables meaning that the system has had enough time to synchronize itself. This, together with the

strong magnetic field of the white dwarf, result in polars where the rotating white dwarf is synchronous with the binary orbital period ($P_{\text{spin}} = P_{\text{orb}}$; Cropper 1990). A small group of polars, known as asynchronous polars, present white dwarfs with spin periods that are slightly ($\sim 2\%$) shorter than the binary orbital periods. It is believed that the synchronicity of this type of polars was perturbed by a nova eruption, and they are evolving back to synchronized periods on times scales of 100 to 13000 years (Myers et al. 2017, Littlefield et al. 2023). Polars are known to switch between high and low mass-accretion rate states spending roughly half their time in low states, as seen in the case of the prototype AM Her (Hessman et al. 2000), making their identification and characterization challenging (Pretorius et al. 2013). Even though the cause of high/low state transitions is not certain, the most likely explanation at the moment is star spots of the donor drifting in front of the inner Lagrangian point which cause a significant decrease in the mass transfer rate of the system (Livio and Pringle 1994, Kafka and Honeycutt 2005).

In both polars and intermediate polars, the accretion flow close to the white dwarf is channeled along the magnetic field lines, as shown in Fig. 1-10, reaching supersonic velocities that produce a shock front above the white dwarf surface (Aizu 1973). The emitted radiation spectrum arising from this shock front has three components: hard X-rays, cyclotron emission, and soft/medium X-rays (Mukai 2017). The hard X-rays are emitted from the post shock flow in the column (see Fig. 1-10), which is optically thin to hard X-rays, by thermal Bremsstrahlung, also producing cyclotron radiation that can be observed in the optical and near-infrared band. Roughly half of the hard X-rays will escape into space (Rothschild et al. 1981), with the other half being emitted towards the white dwarf surface where they are absorbed and then thermalized and re-emitted (see Fig. 1-10) as an approximate blackbody spectrum in the ultraviolet or soft X-rays (Lamb and Masters 1979), also presenting emission features in medium X-rays (~ 6.5 keV) that are possibly due to fluorescence caused by reflection from the white dwarf (Rothschild et al. 1981).

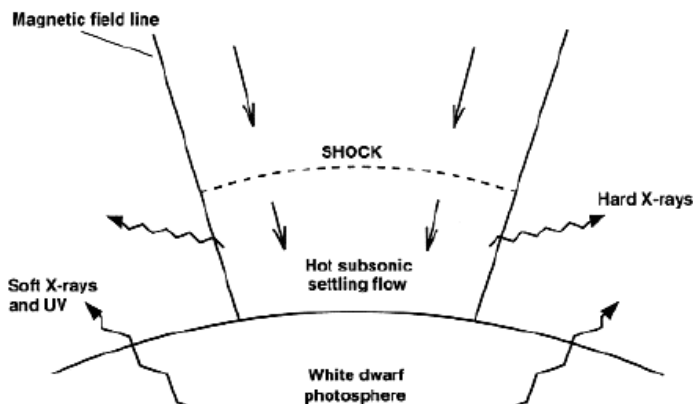


Figure 1-10.: Sketch of the accretion flow in magnetic cataclysmic variables (Potter 1998) showing the origin of the different types of X-ray emissions.

2. Period-Bounce Cataclysmic Variables

Period-bouncers represent the last stage in the evolution of cataclysmic variables, and are characterized by having a very cool white dwarf ($T_{\text{eff}} \sim 10000\text{K}$) and a very evolved donor (L to T type). As stated in Sect. 1.2, mass accretion rates of cataclysmic variables decrease with age, meaning that period-bouncers have extremely low mass accretion rates and are very faint systems. Because of the low mass accretion rates, period-bouncers are expected to be largely non-variable, only experiencing outbursts on timescales of decades or longer (Patterson 2011).

The actual contribution from period-bouncers to the total cataclysmic variable population is highly disputed. One of the key predictions in theoretical models of cataclysmic variable evolution is that period-bouncers are expected to make-up the majority of the cataclysmic variable population, with estimates ranging between 40 % and 80 %, depending heavily on the formation and evolution model used as well as the adopted initial parameters (see e.g., Kolb 1993, Goliašch and Nelson 2015, Schreiber et al. 2016, Belloni et al. 2020). However, from a volume-limited sample study of cataclysmic variables by Pala et al. (2020) within 150pc, the observed fraction of period-bouncers is only between 7 % and 14 %. To date there are only 18 cataclysmic variables with a detected late-type donor which have been securely classified as period-bouncers (see Table 2-1). This under-representation may be due to selection biases against period-bouncers, as their defining characteristics of being old and faint cataclysmic variables with low luminosity and mass transfer rates make their identification challenging (Patterson 2011).

2.1. Observational Characteristics of Period-Bounce Cataclysmic Variables

In order to increase the observed population of period-bouncers it is important to first consider their characteristics in each spectral band. To illustrate these characteristics, examples of confirmed period-bouncers from the X-ray to the infrared band are discussed here.

Fig. 2-1 presents the X-ray spectrum of the confirmed period-bouncer SDSS J103533.02+055158.4 taken using *XMM-Newton*. The very low-mass donors (L and T dwarfs) and cool white dwarfs of period-bouncers have extremely weak or even no coronal X-ray emission, which is below the sensitivity of present-day instruments (Audard et al. 2007; De Luca et al. 2020). The X-ray emission of period-bouncers, therefore, comes from the accretion structures present in

Table 2-1.: Confirmed period-bouncers with detected late-type donors. Included is the confirmation of a brown dwarf (BD) or late-type donor in the system through spectroscopy (S) or photometry (P) with the corresponding reference.

Period-bouncer	Donor SpT	Reference
V379 Vir	L8 (S)	Farihi et al. (2008)
SDSS J15141+0744	L3 or later (P)	Breidt et al. (2012)
PM J12507+1549	M8 or later (P)	Breidt et al. (2012)
SDSS J10575+2759	L5 or later (P)	McAllister et al. (2017)
SDSS J14331+1011	L1 (S)	Santisteban et al. (2016)
WZ Sge	L2 (S)	Harrison (2015)
SDSS J10353+0551	L0 or later (P)	Southworth et al. (2006)
SMSS J16063-1000	L2 to L6 (P)	Kawka et al. (2021)
QZ Lib	T (S)	Pala et al. (2018)
GD 552	L0 (S)	Unda-Sanzana et al. (2008)
MT Com	Very late (P)	Patterson et al. (2005b)
V455 And	L2 or later (P)	Araujo-Betancor et al. (2005)
V406 Vir	L3 (S)	Pala et al. (2019)
BW Scl	T (S)	Neustroev and Mäntynen (2023)
EZ Lyn	L2 (P)	Zharikov et al. (2013)
CRTS J12222-3115	L0 or later (P)	Neustroev et al. (2017)
V1108 Her	L1 (S)	Ishioka et al. (2007)
SRGe J04113+6853	T (S)	Galiullin et al. (2024)

the system, either an accretion disk or a hot-spot on the surface of the white dwarf, which unequivocally distinguishes period-bouncers from single white dwarfs and detached binaries. Therefore, an X-ray detection of a period-bounce candidate is a key diagnostic of ongoing mass accretion in the system.

The X-ray spectra of period-bouncers (see Sect. 3.3) can be used to obtain the X-ray flux and used to derive the X-ray luminosity if the distance to the system is known. Both of these parameters have been used in this thesis to differentiate period-bouncers from pre-bounce short-period cataclysmic variables (see Sect. 4.2.3), which makes the X-ray flux and luminosity of cataclysmic variables a powerful tool in the identification of new period-bouncers (Muñoz-Giraldo et al. 2024).

Fig. 2-2 shows the ultraviolet spectrum of the confirmed period-bouncer QZ Lib taken using the *Hubble Space Telescope*. At these wavelengths, in low mass transfer systems, the white dwarf is visible during the quiescent state, which is expected to be the main state of period-bouncers as they rarely experience outbursts or superoutbursts. In period-bouncers the ultraviolet emission comes exclusively from the cool white dwarf which can be identified

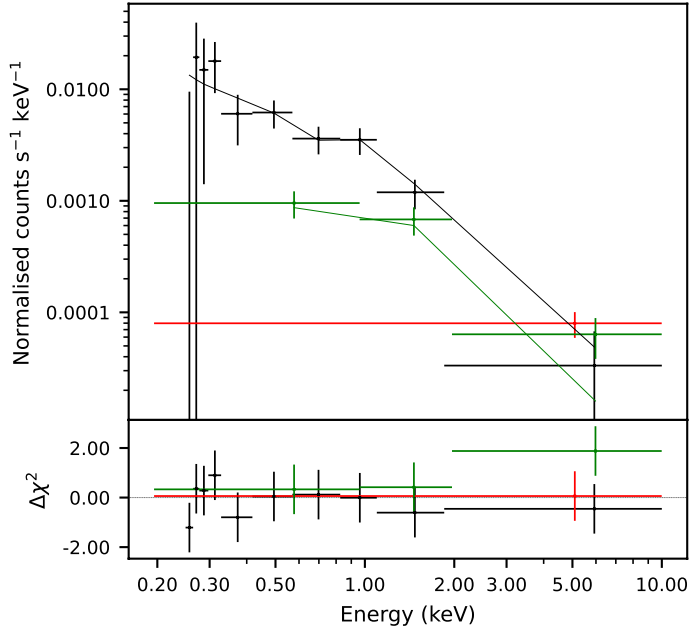


Figure 2-1.: *XMM-Newton* spectrum of the confirmed period-bouncer SDSS J103533.02+055158.4 and fitted two-temperature thermal plasma model (Schwope et al. 2021). EPIC-pn, MOS1, and MOS2 are plotted in black, red, and green, respectively.

by the presence of broad Ly α absorption (centered at 1216Å) from its photosphere (Pala et al. 2022).

Performing a fit to the ultraviolet spectra of period-bouncers gives information on the white dwarf in the system, specifically its effective temperature, $\log(g)$ and mass. Contrary to the mass of the white dwarf in cataclysmic variables, which has been observed as staying relatively constant at $\sim 0.8M_{\odot}$ throughout its evolution (Pala et al. 2022), the white dwarf temperature is expected to change with the age of the binary, as the mass accretion rate decreases, and therefore can be used to identify short-period cataclysmic variables and period-bouncers (Patterson 2011).

Fig. **2-3** presents the optical spectrum of the confirmed period-bouncer SDSS J103533.02+055158.4 taken using SDSS. Similar to the ultraviolet band, at these wavelengths the emission of period-bouncers is dominated by the white dwarf considering that they are low mass transfer systems and are very likely in a quiescent state. The cool white dwarf in period-bouncers can be identified by the presence of broad Balmer absorption lines (H δ , H γ , H β and H α). From the optical spectrum of period-bouncers we can obtain several system parameters like the effective temperature and the orbital period of the system. The effective temperature of the white dwarf can be obtained by fitting white dwarf templates to the optical spectrum of a period-bouncer with a known distance (Littlefair et al. 2008). The orbital period of the system can be determined if there are time-resolved optical spectra, as trailed spectra of emission lines (variation in time of the wavelength associated with the peak of the emission line) track orbital motion around the center of mass of the system due to the line being red or blue shifted depending on the orbital phase (Marsh and Horne 1988). Balmer emission lines, specifically the H α emission line, are the most commonly used for this purpose (Breedt et al. 2012, Pala et al. 2018).

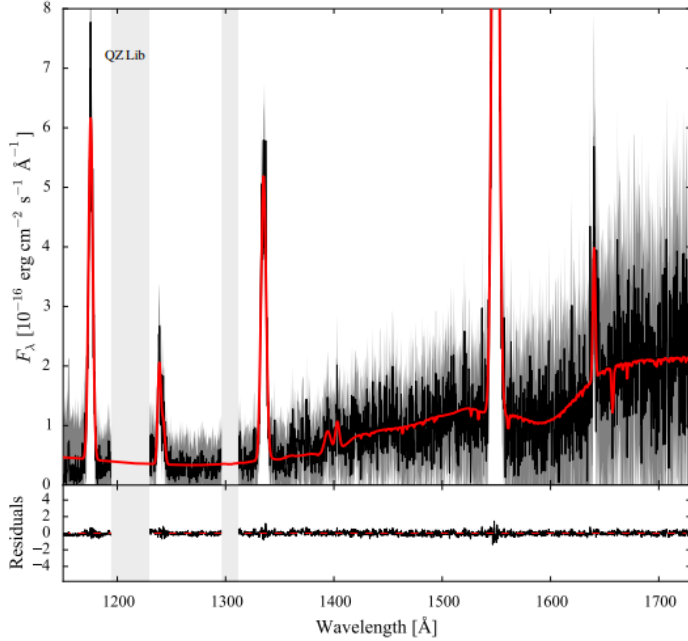


Figure 2-2.: *Hubble Space Telescope* spectrum of the confirmed period-bouncer QZ Lib in black and best-fitting synthetic atmosphere model ($T_{\text{eff}}=11419$ K, $\log(g)=8.3$ and $Z=0.01 Z_{\odot}$) in red (Pala et al. 2022).

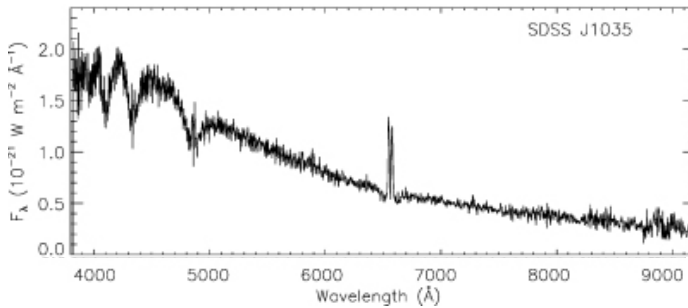


Figure 2-3.: SDSS spectrum of the confirmed period-bouncer SDSS J103533.02+055158.4 (Southworth et al. 2006).

Additionally, the presence and absence of certain features in the optical spectra can also help constrain parameters from the system. The presence of Zeeman splitting of the Balmer absorption lines indicates that the white dwarf in the system is magnetic. This is not the case for SDSS J103533.02+055158.4 shown in Fig. 2-3, a non-magnetic period-bouncer (see Sect. 4.1.1 for examples of optical spectra of magnetic period-bouncers). The absence of metal absorption bands in the optical spectrum (typically $\lambda \geq 7900\text{\AA}$) indicates the presence of a donor with a later than M spectral type in the system. This is because the optical spectra of M dwarfs are mainly dominated by diatomic metal oxides, like titanium oxide (TiO) and vanadium oxide (VO), with the strength of TiO bands specifically decreasing from early to late M dwarfs (Rajpurohit et al. 2018). SDSS J103533.02+055158.4, shown in Fig. 2-3, does not present these bands, which is expected for a confirmed period-bouncer that has a donor with a L0 or later spectral type.

Fig. 2-4 shows the spectra of the confirmed period-bouncers QZ Lib and SDSS J143317.78+101122.8 including the near-infrared band. This band, from $\sim 10000\text{\AA}$, is where the very late-type do-

nors of period-bouncers have a detectable contribution. As this example demonstrates, a spectrum of a period-bouncer which includes the infrared band can help characterize the late-type donor in the system. This can be done via two methods: direct detection through the identification of absorption lines arising from the donor, or fitting the spectrum using templates from late-type stars (Pala et al. 2018).

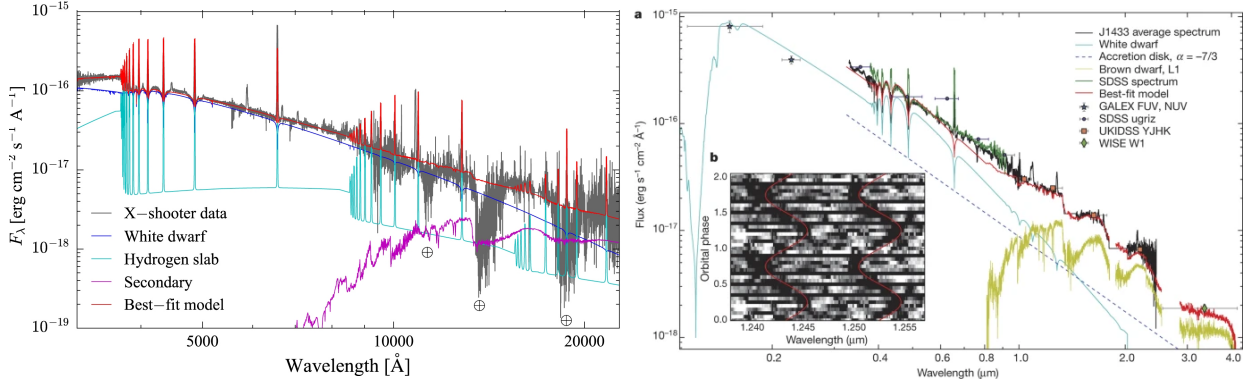


Figure 2-4.: X-shooter spectra of confirmed period-bouncers. **Left panel:** QZ Lib spectrum with best-fit model. Due to the presence of broad telluric absorption bands (marked with Earth’s symbol) the direct detection of the late-type donor was not possible (Pala et al. 2018). **Right panel:** SDSS J143317.78+101122.8 spectrum with best-fit model. Sub-panel b shows the trailed, phase-binned spectra around the KI doublet ($12432\text{\AA}/12522\text{\AA}$) which constitutes a direct detection of the late-type donor (Santisteban et al. 2016).

Even though the direct detection method through the identification of absorption lines arising from the donor provides the most secure confirmation of a late-type donor in the system as well as allowing to determine the spectral type and mass of the donor, it is extremely hard to perform successfully. This is mainly due to the faintness that is characteristic of period-bouncers which often leads to a signal to noise ratio that is insufficient for the identification of typical absorption lines that can be associated with a late-type donor. Additionally, as can be seen in Fig. 2-4, at this wavelength range telluric absorption features arising in the Earth’s atmosphere further complicate the identification of the absorption lines. In the case of QZ Lib, the direct detection of the late-type donor in the system was not possible, but this method has led to the identification of late-type donors in other period-bouncers like SDSS J143317.78+101122.8 (Fig. 2-4; Santisteban et al. 2016), WZ Sge (Harrison 2015), and V406 Vir (Pala et al. 2019). The most prominent absorption lines used for the direct identification of the donor are Na I $11381\text{\AA}/11403\text{\AA}$, K I $11690\text{\AA}/11769\text{\AA}$, and K I $12432\text{\AA}/12522\text{\AA}$ (Fig. 2-4).

On the other hand, an overall fit of the spectrum using templates, which allows to constrain the spectral type of the donor, is an easier method than the method relying on the direct detection of the donor, as it does not require a high signal to noise ratio in order to be

successful. As can be seen Fig. 2-4, the best-fit model for both confirmed period-bouncers suggests the presence of a late-type donor in the system, T-type for QZ Lib (Pala et al. 2018) and L1-type for SDSS J143317.78+101122.8 (Santisteban et al. 2016).

2.2. Searching for Period-Bounce Cataclysmic Variables

From the spectral characteristic of period-bouncers it is known that this sub-type of cataclysmic variables are strongly dominated by the cool white dwarf in the ultraviolet and optical bands, meaning that in these bands period-bouncers are most likely classified as single white dwarfs. The present day vast catalogs of white dwarfs compiled using optical surveys like SDSS or *Gaia* might include a considerable number of hidden period-bouncers.

In order to find the missing population of period-bouncers, which is the main goal of this work, it is necessary to distinguish between them and single white dwarfs. This can be achieved through two different paths, the detection of X-ray emission coming from the system, which is proof that accretion is taking place and, therefore, that the system is most likely an interacting binary, and the identification of an excess of emission over the white dwarf contribution in the infrared spectrum of the system, where such emission could be produced by a late-type donor.

Given the unprecedented advantages provided by all-sky X-ray surveys like eROSITA, which will be covered in the following chapters, an X-ray search for the missing population of period-bouncers seems like a promising path to follow and, therefore, constitutes the central theme for this work.

3. X-ray Satellites, Detections, and Analysis

This thesis is based around the search for the missing population of period-bounce cataclysmic variables using X-ray data. In this chapter I review the main instruments used for the X-ray detection of cataclysmic variables, and how they have historically fared in the detection of period-bouncers.

3.1. Historical Context

Cataclysmic variables have been historically detected due to their large changes in magnitude (see Warner 1995), but it was not until 1973, with the detection in soft X-rays of SS Cygni (Rappaport et al. 1974), that cataclysmic variables were first studied using X-rays. This detection opened the door for more comprehensive studies of cataclysmic variables using X-rays leading to the detection of a few cataclysmic variables with satellites like HEAO-1 (High Energy Astronomy Observatories; Cordova et al. 1981a), EXOSAT (European Space Agency's X-ray Observatory; Osborne 1987), and Einstein (Cordova et al. 1981b). Campaigns to detect a broader population of cataclysmic variables have been previously carried out using X-ray instruments ROSAT All Sky Survey and *Chandra*, with the detection of a few dozen cataclysmic variables with known or suspected binary periods (Verbunt et al. 1997, Schwöpe et al. 2002, Munro et al. 2006).

Most of the confirmed identifications of period-bounce cataclysmic variables (see e.g. Patterson et al. 2005b, McAllister et al. 2017, Neustroev et al. 2017, Pala et al. 2018, Schwöpe et al. 2021, Amantayeva et al. 2021, Kawka et al. 2021, Neustroev and Mäntynen 2023) have occurred through detailed observations of specific systems using different instruments in the X-ray, optical and/or infrared bands. As a result, the sample of period-bouncers with complete and reliable system parameters is quite small, and may not be representative of period-bouncers as a class. With the launch of the extended ROentgen Survey with an Imaging Telescope Array (eROSITA; Predehl et al. 2021) onboard the Spektrum-Roentgen-Gamma mission (SRG; Sunyaev et al. 2021) new studies of the X-ray activity of period-bouncers are being conducted. Even though the high sensitivity of *XMM-Newton* is required to produce a detailed study of accreting period-bounce systems, the enormous statistical samples of faint X-ray sources that are being observed by eROSITA (see Sect 3.2.2) is expected to boost

the number of new detections and new identifications among period-bounce candidates, as demonstrated in this thesis.

3.2. Satellites and Missions

X-ray radiation, in general, can be emitted by astronomical objects which are made of hot gas at temperatures of $\sim 10^6$ to 10^8 K. However, objects in binaries also represent a non-negligible part of X-ray emission, which is coming not only from hot gas but from the different interaction processes and structures arising in the system. Considering that the Earth's atmosphere absorbs incoming X-rays, space-based telescopes are required to find and study astrophysical X-ray sources. The data used in this thesis were obtained with *XMM-Newton* and eROSITA.

3.2.1. XMM-Newton

XMM-Newton was launched on December 10th 1999 by the European Space Agency (ESA) as part of the Horizon 2000 Science Programme. On board *XMM-Newton* there are three co-aligned Wolter Type I grazing incidence gold-coated imaging X-ray telescopes and one Optical Monitor (OM; Mason et al. 2001), allowing it to perform simultaneous X-ray and optical/ultraviolet observations. Each X-ray telescope supplements one of the European Photon Imaging Cameras (EPIC; Strüder et al. 2001, Turner et al. 2001), comprising one PN camera, and two Metal Oxide Semi-conductor (MOS1, MOS2) CCD arrays, as well as a Reflection Grating Spectrometer (RGS; Den Herder et al. 2001). The EPIC cameras cover a 0.15-15 keV energy range with moderate spectral resolution ($E/dE \sim 20-50$) while the RGS spectrometer covers a 0.35-2.5 keV energy range with a much higher spectral resolution ($E/dE \sim 200-800$). See Fig 3-1 for a diagram of *XMM-Newton* with the individual instruments.

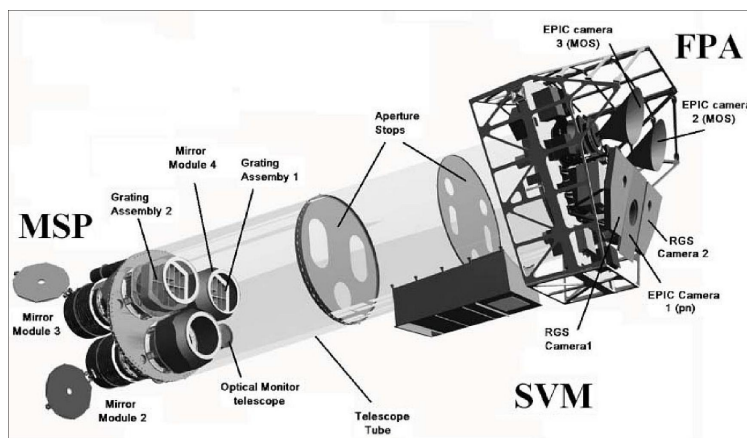


Figure 3-1.: View of the *XMM-Newton* spacecraft subsystems. External structure was removed for clarity. MPS: Mirror Support Platform, SVM: Service Module, FPA: Focal Plane Assembly (Credit: ESA).

The three EPIC cameras (EPIC/pn, EPIC/MOS1 and EPIC/MOS2) together with two RGS

spectrometers are located in the focal plane of the X-ray telescopes (FPA in Fig. **3-1**), while the OM is mounted on the mirror support platform alongside the X-ray mirror modules (MSP in Fig. **3-1**). As long as the brightness of the target does not exceed the brightness constraints for the instrument configuration, all six XMM-Newton instruments can work on their own or simultaneously, allowing imaging observations over a field of view of 30' covered by all the instruments.

All EPIC CCDs operate in photon counting mode with a fixed and mode dependent frame readout frequency, producing event lists. The event lists record single line entries for every recorded incoming photon listing position, arrival time and energy as parameters. Additionally, the two types of EPIC cameras differ in some major aspects: the quantum efficiency (EPIC/pn has a larger quantum efficiency than the EPIC/MOS cameras because its chips are back-illuminated), and the readout times (in the EPIC/pn camera each pixel column has its own readout node leading to a faster readout than the one by the EPIC/MOS camera). The EPIC cameras can operate in three different modes: full frame mode (which covers the whole field of view, meaning all pixels are read out), partial window mode (where only certain areas of the CCDs are readout), and timing mode (which keeps the spatial information only in one dimension, offering very high time resolution for all EPIC cameras). Additionally, three optical blocking filters are considered for observations because the EPIC cameras are not only sensitive to X-ray photons, but also to infrared, visible and ultraviolet light. Thick filter, which should be used if the expected visible brightness of the target would degrade the energy scale and resolution of the observation, up to $m_V = -2 - 1$. Medium filter, that is useful for preventing optical contamination from point sources as bright as $m_V = 6 - 9$. Thin filter, which should be used for very faint point sources with magnitude fainter than $m_V = 10 - 13$.

The RGS unit is made up of two Reflection Grating Assemblies (RGAs) and two RGS Focal Cameras (RFCs), located on the same X-ray telescope where the EPIC/MOS camera is mounted. When an X-ray signal is captured by this instrument, each RGA intercepts about 58 % of the total light focused by the mirror module. The RFC consists of linear arrays of nine large back-illuminated MOS CCDs (similar to the ones used in the EPIC/MOS cameras) located in the dispersion direction of the RGAs, where the CCDs are registering, for each incoming photon, the position and the energy. RGS can operate in two modes: spectroscopy mode (standard science mode of operation in which all CCDs are operating over the full energy range), and small window mode (where only the central 32 of the 128 CCDs rows are actively working and it is recommended only for very bright sources).

In addition to X-ray observations, *XMM-Newton* also allows for simultaneous optical and ultraviolet observations using the 30cm OM co-aligned with the X-ray mirror modules. The OM provides advantages such as the absence of atmospheric extinction, diffraction and background, as well as having a detector with high sensitivity, which makes the instrument very useful when detecting faint sources. However, the OM instrument can only be used when there is no bright optical source in the field of view because of how sensitive it is and

how easily it could be damaged by bright optical sources.

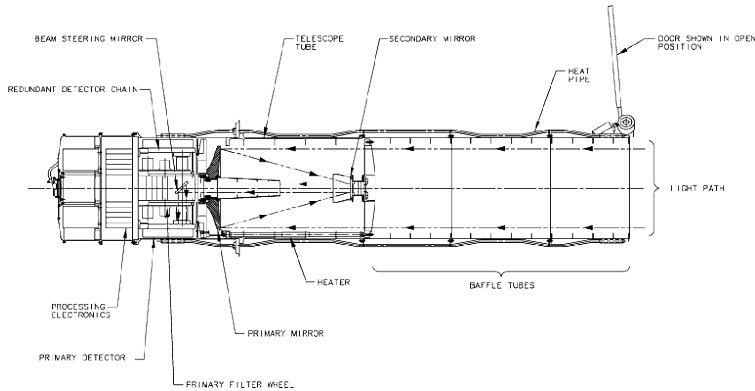


Figure 3-2.: Light path in *XMM-Newton's* optical/ultraviolet telescope (Credit: ESA).

In the OM, incoming light follows a path as shown in Fig. 3-2, where it is initially reflected by a primary mirror onto a secondary mirror from which the light is reflected onto a rotatable 45° flat mirror located behind the primary. At this point, the beam is directed onto one of two detector arrays. The OM detector in use by *XMM-Newton* is a compact image-intensified photon-counting instrument consisting of a micro-channel plate intensified CCD. A filter wheel with several optical elements (lenticular filters and two grisms) can be placed into the light path, where the set of filters covers part of the ultraviolet and optical range (see Fig. 3-3). The OM can operate using two modes, an “Image mode” that accumulates images with no timing information of the incoming photons, and a “Fast mode”, which provides an event list that gives the detected counts over time allowing for the extraction of a light curve of the target.

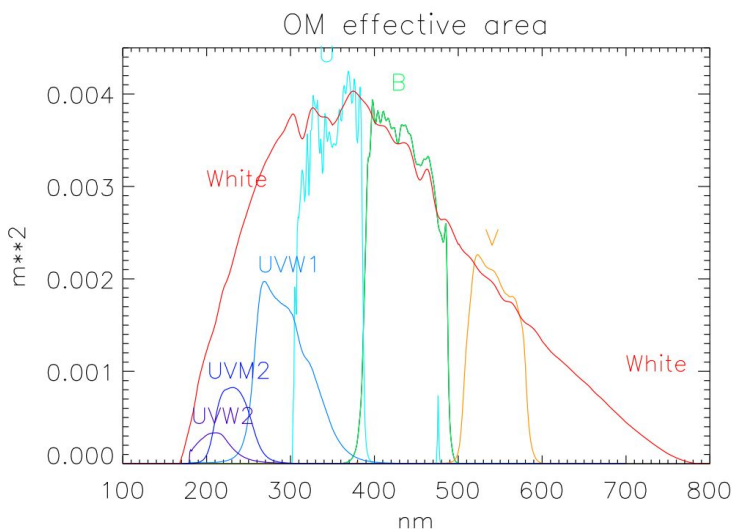


Figure 3-3.: Throughput curves for the OM filters, folded with the detector sensitivity (Credit: ESA).

3.2.2. SRG-eROSITA

The SRG satellite was launched on July 13th 2019 as part of a high energy astrophysics mission developed by Russia and Germany. On board SRG there are two instruments, eROSITA built by the Max Planck Institut für Extraterrestrische Physik (MPE) in Germany and the Astronomical Roentgen Telescope X-ray Concentrator (ART-XC) developed by Russia. This mission was designed as an all-sky survey of the X-ray sky. As part of the german consortium the data used in this thesis was acquired exclusively through the use of eROSITA, specifically using the sky area with German data rights which corresponds to the western half of the sky in terms of Galactic coordinates (Galactic longitude $l \geq 180^\circ$).

From the launch until the SRG satellite was placed in a halo orbit around the L2 point, eROSITA carried out its Calibration and Performance Verification (CalPV) program for approximately two months resulting in its first X-ray catalog, the eROSITA Final Equatorial Depth Survey (eFEDS; Brunner et al. 2022). Since December 2019, eROSITA has been performing all-sky surveys (eRASS), in which the whole celestial sphere is mapped once every six months. The first eROSITA all-sky survey (eRASS1) was completed on June 11th 2020, while the last (eRASS5) was interrupted on February 26th 2022 providing only partial all-sky coverage. The eRASS1 catalog, officially released to the public on January 31st 2024 as part of the first eROSITA data release, contains data from 930000 sources in the soft band, an increase in the number of known X-ray sources in the published literature by more than 60% (Merloni et al. 2024).

eROSITA was designed as a sensitive wide-field X-ray instrument covering the entire sky in a 0.2-10 keV energy range, consisting of seven identical co-aligned Wolter-1 telescope modules (TMs) arranged in a hexagonal shape each with 54 nested mirror shells used to focus X-rays onto a CCD detector (Fig. 3-4; Predehl et al. 2021). The spectral resolution achieved by eROSITA (~ 49) After the mission is completed, eROSITA is expected to be about 25 times more sensitive than the ROSAT all-sky survey in the soft band (0.2-2.3 keV) (Predehl et al. 2021).

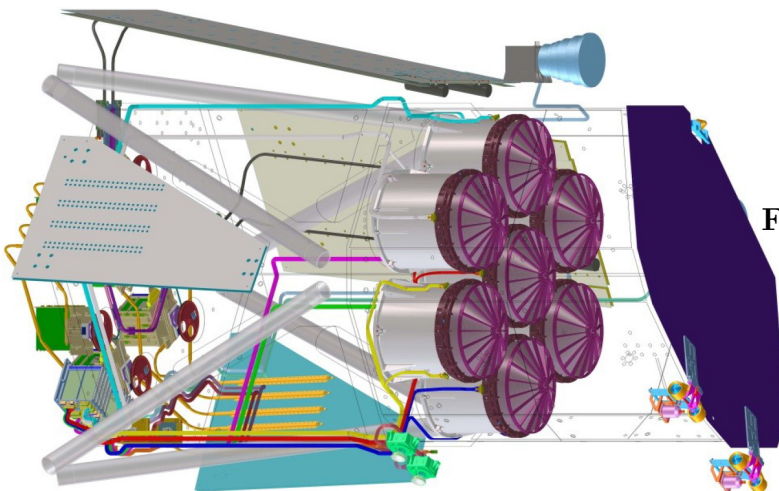


Figure 3-4.: Schematic view of the eROSITA telescope (Predehl et al. 2021).

When compared to the on-axis effective areas of the combined *XMM-Newton* cameras (PN, MOS1, and MOS2), the combined eROSITA telescope modules (TM 1-7) have almost the same effective areas between ~ 0.5 and 2.0 keV (see blue and red lines respectively in Fig. 3-5), with *XMM-Newton* having better effective areas outside of this range. Additionally, the larger field of view of eROSITA ensures that the grasp, defined as the product of effective area and observing area, is significantly greater than *XMM-Newton* below ~ 3.5 keV. However, at higher energies the grasp of *XMM-Newton* is greater (Turner et al. 2022).

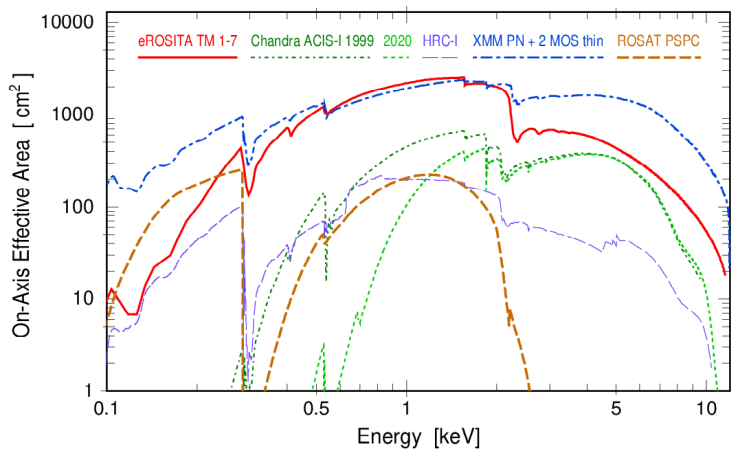


Figure 3-5.: Comparison of the on-axis effective areas as a function of energy for different X-ray telescopes (Predehl et al. 2021). Two curves are shown for *Chandra* as it has undergone significant degrading from its original launching (1999) until recent years (2020).

The driving goal of eROSITA is the detection of large samples of galaxy clusters and active galactic nuclei, up to red-shifts $z > 1$, which allows for the study of large-scale structures in the Universe as well as characterization of cosmological models including Dark Energy. The data produced by eROSITA additionally allows the investigation in a wide range of fields including research on compact objects, active stars and diffuse emission within the Galaxy.

3.3. Analysis of X-ray data

Two data products derived from an X-ray observation are the light curve and the spectrum of the source. From these two, several system parameters can be obtained including orbital period of the system, flux, temperature, abundance, luminosity, and mass accretion rate. However, in order to analyse the data products, specifically the spectrum, it is necessary to generate response matrices using the instrument specific Redistribution Matrix File (RMF), and Auxiliary Response File (ARF). The RMF is a matrix that describes the response of the instrument as a function of energy and PI channel, while the ARF matrix takes calibration information and performs the necessary corrections for instrumental factors like effective area of the telescopes together with the vignetting or the diffraction efficiency of the gratings, the transmissions of the filters, and the quantum efficiency of the detectors, amongst others.

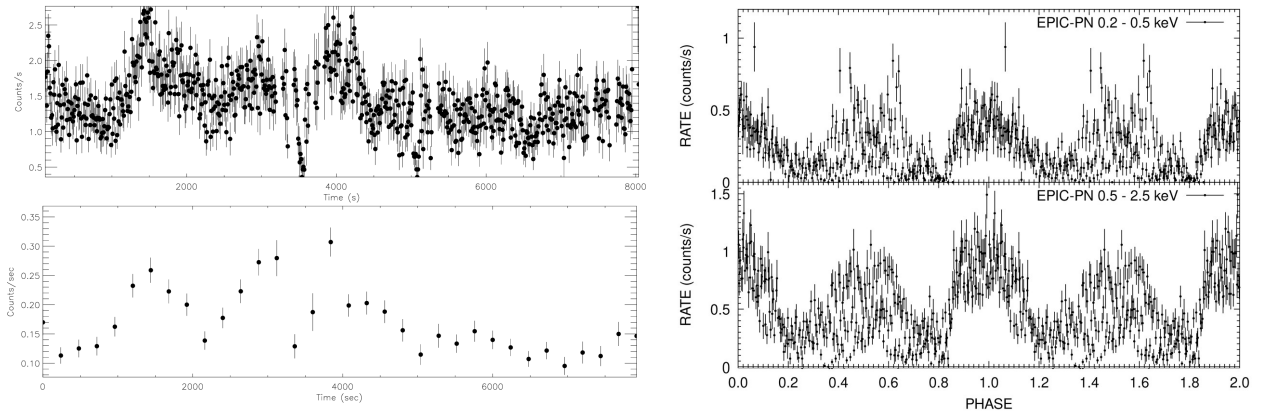


Figure 3-6.: *XMM-Newton* light curves of cataclysmic variables. **Left panel:** Confirmed period-bouncer WZ Sge, a non-magnetic cataclysmic variable, with a light curved binned using 10s (upper panel) and 240s (bottom panel) (Nucita et al. 2014). **Right panel:** V496 UMa, a polar with two-pole accretion geometry (Ok and Schwobe 2022).

The light curve of a source shows its intensity evolving with time, meaning that it keeps track of the incoming number of photons over a period of time also known as the count rate. Because of this, a light curve allows the detection of periodic changes in a system like orbital modulation in binaries. Orbital modulation tracks a specific emission region which is affected by the orbital motion of the binary, and can therefore give information on the orbital period of the system (see examples in Fig. 3-6). Depending on the types of binaries this tracking of the orbital period can be easier or more difficult. Specifically for period-bounce cataclysmic variables, as mentioned in Sect. 2.1, X-rays are emitted exclusively from the accretion structures in the system, meaning that an X-ray light curve is tracking the orbital modulation of the accretion disk and/or the hot-spot on the surface of the white dwarf. In the case of non-magnetic cataclysmic variables and intermediate polars the detection of an accurate orbital period from an X-ray light curve can be slightly challenging as the X-ray emission could be associated with different parts of the accretion disk which have a different periodicity than the system or with the spin period of the white dwarf which is not synchronized with the orbital period for either of these cataclysmic variable sub-types (see Sect.1.3.2). In Fig. 3-6 the X-ray light curve of WZ Sge, a non-magnetic confirmed period-bouncer, shows two periodicities (suggested as being associated with the spin period or pulsations from the white dwarf) in addition to an orbital modulation corresponding to the orbital period of the system (Nucita et al. 2014). On the other hand, polars are characterized by having a synchronized orbital-spin period as well as by not presenting an accretion disk, meaning that orbital modulation in an X-ray light curve easily tracks the orbital period of the system thanks to X-ray emission coming from one of the white dwarf’s magnetic poles

(see Sect. 4.1.2 for an example of one-pole accretion geometry), or from both poles in which case the orbital modulation of the X-ray light curve corresponds to half of the orbital period (as seen by the double-humped orbital modulation of V496 UMa in Fig. **3-6**).

The spectrum of a source represents the number of photons, or more commonly the flux, over an energy range. X-ray instruments cannot measure astrophysical fluxes directly, but rather deliver a count rate after detection in a certain energy band. Only with the assumption of a spectral model can the flux be obtained from the count rate using what is known as energy conversion factors (ECFs in units of $\text{erg cm}^{-2} \text{s}^{-1} / \text{cts s}^{-1}$), meaning that the X-ray flux reported by an instrument represent a measured count rate multiplied by an ECF that depends on the spectral model and the instrumental response. For systems with an established distance (d), the X-ray luminosity (L_x) can be obtained from the X-ray flux (F_x) as

$$L_x = 4\pi d^2 F_x. \quad (3-1)$$

The X-ray luminosity can be in turn used to obtain an instantaneous mass accretion rate (\dot{M}_{inst}) for systems with an established primary mass (M_{primary}) and radius (R_{primary}) as

$$\eta \left(\frac{GM_{\text{primary}} \dot{M}_{\text{inst}}}{R_{\text{primary}}} \right) = L_x \quad (3-2)$$

$$\dot{M}_{\text{inst}} = \frac{1}{\eta} \left(\frac{L_x R_{\text{primary}}}{GM_{\text{primary}}} \right), \quad (3-3)$$

which assumes that the gravitational potential energy associated with accretion is being radiated away as X-rays. Assuming the standard case by Shakura and Sunyaev (1973), in non-magnetic cataclysmic variables half of the energy is radiated away by the boundary layer while the other half is stored by the accretion disk ($\eta=1/2$). On the other hand, magnetic cataclysmic variables lack an accretion disk meaning that all the energy is radiated away ($\eta=1$).

In the case of cataclysmic variables, the instantaneous mass accretion rate represents the accretion onto the white dwarf required to produce the observed X-ray luminosity, and therefore represents the immediate mass accretion taking place in the system. On the other hand, the term secular mean accretion rate is commonly used to describe the evolution of cataclysmic variables (see Knigge et al. 2011, Goliach and Nelson 2015, Pala et al. 2022) and refers to the accretion rate derived from the long-term thermal evolution of the white dwarf (10^3 - 10^5 yr). According to Pala et al. (2022), the secular mean accretion rate (\dot{M}_{sec}) can be derived using the effective temperature (T_{eff}), mass (M_{WD}) and radius (R_{WD}) of the white dwarf as

$$L_{\text{WD}} = 4\pi R_{\text{WD}}^2 \sigma T_{\text{eff}}^4 \quad (3-4)$$

$$6 \times 10^{-3} L_{\odot} \left(\frac{\dot{M}_{\text{sec}}}{10^{-10} M_{\odot} \text{yr}^{-1}} \right) \left(\frac{M_{\text{WD}}}{0.9 M_{\odot}} \right)^{0.4} = 4\pi R_{\text{WD}}^2 \sigma T_{\text{eff}}^4 \quad (3-5)$$

with the Stefan-Boltzmann constant σ . The luminosity of the white dwarf used for this calculation refers to the average quiescent surface luminosity during the classical nova cycle (Townesley and Gänsicke 2009). In this thesis the discussion is limited to the instantaneous mass accretion rate derived from X-ray data.

Cataclysmic variables present thermal spectra, with both magnetic and non-magnetic systems exhibiting multi-temperature plasma emission (Mukai 2003). Because of this, for the spectral analysis of cataclysmic variables, a model based on the X-ray emission of optically thin astrophysical plasma in collisional equilibrium, known as APEC¹, is commonly used to produce a spectral fit. The APEC model considers four parameters: the plasma temperature (kT), the global abundance (Z), the emission measure (EM), and the redshift. The EM refers to the number density of free electrons and hydrogen integrated over the volume of the emitting plasma ($EM = \int n_e n_H dV$) which can be obtained from the normalization factor (N) of the spectral fit as

$$EM \sim 4\pi d^2 N. \quad (3-6)$$

In the course of this thesis, spectral fitting of nearby cataclysmic variables will be performed, meaning that the redshift for these systems is negligible and will not be discussed further.

3.4. Population Outlook

Historically the X-ray detection of period-bouncers has proven difficult due to their intrinsic faintness which has been just at the limit of detection for many of the X-ray instruments and missions. This is clearly evident from the X-ray detections of confirmed period-bouncers that I compiled as a starting point and presented here to set the context for the results of this thesis (see Table 3-1). The systems with X-ray detections in different instruments and missions are marked, with not all of them being reported in the literature (see references column). The last row reports the percentage of confirmed period-bouncers detected by the given instrument. Before the advent of eROSITA, 10 out of the 18 confirmed period-bouncers did not have any X-ray data available, with this still being the case for 4 confirmed period-bouncers that are located in the sky area with Russian data rights.

ROSAT, a satellite covering the entire sky, has the smallest on-axis effective area of the X-ray instruments mentioned in this thesis (see Fig. 3-5), and is only able to detect the brightest confirmed period-bouncers. The resulting detection fraction for the confirmed period-bouncers obtained for ROSAT is lower than the one obtained for *XMM-Newton*, even though ROSAT had performed an all-sky survey.

¹<https://heasarc.gsfc.nasa.gov/docs/xanadu/xspec/manual/node134.html>

Table 3-1.: X-ray detections of confirmed period-bouncers (from Table 2-1).

Period-bouncer	<i>XMM-Newton</i>	ROSAT	eROSITA	References
V379 Vir	x		x	1, 2
SDSS J15141+0744	x			2
PM J12507+1549			x	2
SDSS J10575+2759			x	3
SDSS J14331+1011				
WZ Sge	x	x		4, 5
SDSS J10353+0551	x		x	6, 3
SMSS J16063-1000				
QZ Lib			x	3
GD 552	x	x		
MT Com				
V455 And	x			
V406 Vir			x	3
BW Scl		x	x	7, 3
EZ Lyn				
CRTS J12222-3115			x	3
V1108 Her		x		
SRGe J04113+6853			†	8
Detection fraction	33 %	22 %	50 %	

References. (1) Stelzer et al. (2017), (2) Muñoz-Giraldo et al. (2023), (3) Muñoz-Giraldo et al. (2024), (4) Nucita et al. (2014), (5) Patterson et al. (1998), (6) Schwope et al. (2021), (7) Abbott et al. (1997), (8) Galiullin et al. (2024)

† eROSITA detection in the Russian sky.

The two X-ray missions that perform the best when detecting confirmed period-bouncers are *XMM-Newton* and eROSITA, as it is expected from the two X-ray instruments with the largest on-axis effective areas (see Fig. 3-5). The detection fraction with eROSITA could only be calculated from the available data corresponding to the “German sky” (with the exception of SRGe J04113+6853 whose Russian eROSITA detection is known from the literature; Galiullin et al. 2024). All confirmed period-bouncers in the “German sky” are detected by eROSITA, making it very likely that the majority, if not all, of the confirmed period-bouncers in the Russian sky will also be detected, meaning that the percentage presented here has the potential of doubling. Because of this, the eROSITA detection fraction (last row of Table 3-1) should be taken as a lower limit.

XMM-Newton, as a pointed telescope, would require a great investment of time to study a

large population specially of faint objects, therefore it is better utilized to perform detailed analysis of specific period-bouncers. On the other hand, eROSITA is designed to conduct population studies over the entire sky and, because it has proven to be capable of detecting faint objects, it is conducive for population studies of period-bouncers. This illustrates the high potential of using eROSITA for the search for period-bouncers, which was a main goal pursued in this thesis

4. Results and discussion

In this chapter I summarize and expand on the results presented in the published articles found in Appendix A, as well as recent unpublished results. The prevalent theme through my work was the characterization of period-bouncers and candidates, specially in X-rays, in order to identify new members of this seemingly underrepresented sub-class of cataclysmic variables.

To achieve this goal a three step approach was taken. First, a detailed study of a pilot-sample of magnetic period-bounce candidates using X-rays was performed in order to confirm them as actual period-bouncers (Muñoz-Giraldo et al. 2023). Second, a literature catalog of cataclysmic variables around the period-bounce was compiled, including known period-bouncers (see Table 2-1), and a “scorecard” was produced which was used to assign to each system a probability of being a period-bouncer. Additionally, a systematic analysis of X-ray data from the recent all-sky surveys carried out with eROSITA was used to confirm systems from this catalog as new period-bouncers (Muñoz-Giraldo et al. 2024). And third, a preliminary catalog of new period-bounce candidates detected by eROSITA was constructed that, after confirmation from follow-up surveys, could lead to the identification of the missing population of period-bouncers.

4.1. Study of a Pilot Sample of Period-Bounce Cataclysmic Variables in X-rays

A pilot sample of three magnetic period-bounce candidates was selected by Breedt et al. (2012) to produce a detailed study of the X-ray characteristics of this elusive sub-class of cataclysmic variables. The X-ray study of this pilot sample started in Stelzer et al. (2017) with the determination of important parameters like X-ray flux, X-ray luminosity, and instant mass accretion rates for the only member at that time with an X-ray detection. In Muñoz-Giraldo et al. (2023) typical values for these X-ray parameters were extended for the entire pilot sample, as well as determining the appropriate treatment of period-bouncer data from *XMM-Newton* and eROSITA catalogs.

4.1.1. Characterization of the Pilot Sample

The pilot sample of period-bounce candidates that was selected to search for X-ray emission is drawn from Breedt et al. (2012): V379 Vir (also known as SDSS J121209.31+013627.7), detected as an X-ray source by Burleigh et al. (2006), and the two siblings of V379 Vir, SDSS J125044.42+154957.4 and SDSS J151415.65+074446.4 (henceforth SDSS 1250 and SDSS 1514), that had no X-ray emission reported in the literature.

These systems are composed of a magnetic white dwarf and a presumably very low-mass donor, where the white dwarf in these three systems had been previously identified as magnetic from SDSS spectra, specifically from the Zeeman splitting of the Balmer absorption lines (see Fig 4-1; Schmidt et al. 2005, Vanlandingham et al. 2005, Külebi et al. 2009). The pilot sample was chosen to be composed entirely by magnetic systems, more specifically polars (see Sect. 1.3.2), because cataclysmic variables with a magnetic white dwarf typically show a higher ratio between X-ray flux and optical flux and, thus, higher X-ray luminosity as they do not present a disk through which gravitational energy released via accretion is dissipated (Agüeros et al. 2009). Considering how faint period-bouncers are expected to be, looking for polars, which are supposed to have a higher X-ray luminosity than non-magnetic period-bouncers, increases the chances that the system will be detected using X-rays.

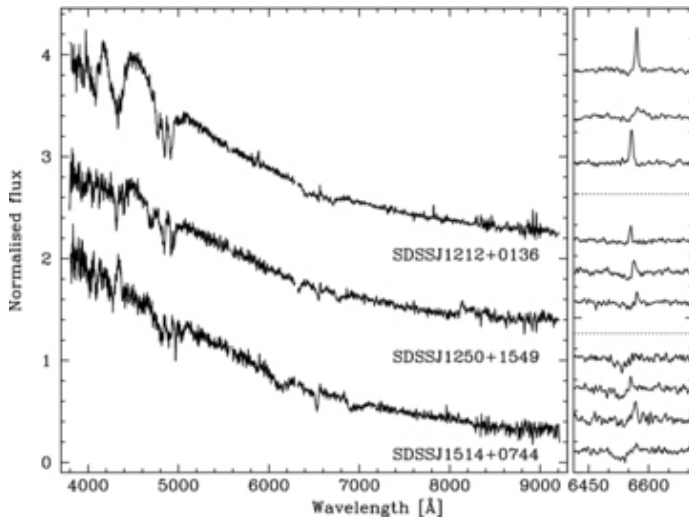


Figure 4-1.: **Left panel:** SDSS spectra of the three members of the pilot sample. **Right panel:** Corresponding SDSS subspectra centred on $H\alpha$ and are offset for clarity (Breedt et al. 2012).

This pilot sample of period-bounce candidates present in their SDSS spectra variable $H\alpha$ emission and no observable features from the companion star. Variable $H\alpha$ emission from time-resolved spectra, as seen in Fig. 4-1, allows a calculation of the orbital period of the system which is a key parameter in the identification of period-bouncers (see Sect. 2.1). An optical orbital period of 88.4 min, 86.3 min and 88.7 min was established for V379 Vir, SDSS 1250 and SDSS 1514, respectively (Burleigh et al. 2006, Breedt et al. 2012). As stated in Sect. 2.1, in optical spectra M dwarfs are mainly dominated by diatomic metal oxides, like titanium oxide (TiO) and vanadium oxide (VO), with the strength of TiO bands specifically decreasing from early to late M dwarfs (Rajpurohit et al. 2018). The absence of these features

indicates the presence of a donor with a later spectral type (L or T) in the system which is expected from period-bouncers.

These systems also share an established 10000-11000 K effective temperature for the white dwarf (Burleigh et al. 2006, Breedt et al. 2012), and their light curves compiled for this thesis using data from the Catalina Real-time Transient Survey (CRTS) and the Zwicky Transient Facility (ZTF) show no large-scale variability, eclipses or high states (Fig. 4-2). Three short-period cataclysmic variables that do exhibit these behaviours are also presented in Fig. 4-2 as a reference, in order to show how invariable the three members of the pilot sample are in comparison.

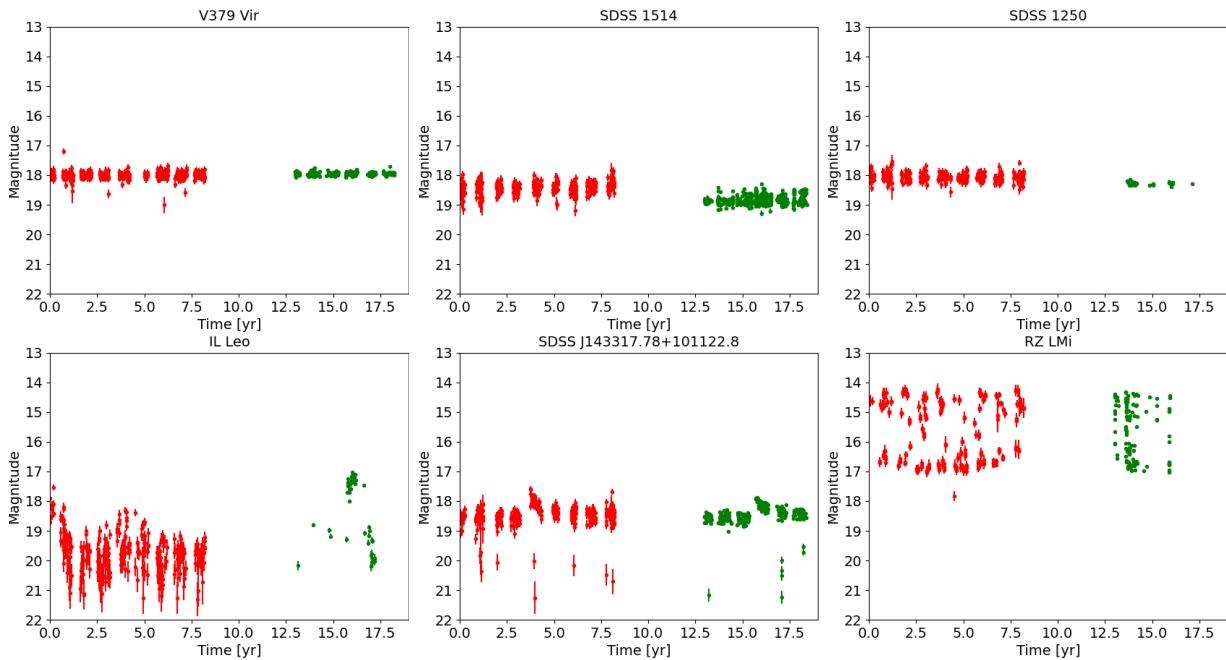


Figure 4-2.: CRTS (in red) and ZTF (in green) light curves. **Top panels:** all three members of the pilot sample. **Bottom left panel:** IL Leo, a short-period cataclysmic variable presenting large scale variability. **Bottom middle panel:** SDSS J143317.78+101122.8, a confirmed eclipsing period-bouncer. **Bottom right panel:** RZ LMi, a short-period cataclysmic variable presenting recurrent high states.

V379 Vir is the only member of the pilot sample with a near-infrared spectrum where the donor’s photospheric features of spectral type L8 were identified together with the contribution of cyclotron emission from the magnetic accreting white dwarf (Farihi et al. 2008). In absence of spectroscopic evidence, infrared photometry with a clear excess over a white dwarf template (see Fig. 4-3) can be used to estimate the donor’s spectral type for the remaining systems: L3 or later for SDSS 1514 estimated by Breedt et al. (2012) from the near-infrared excess in the spectral energy distribution (SED), and M8 for SDSS 1250 estimated by Steele

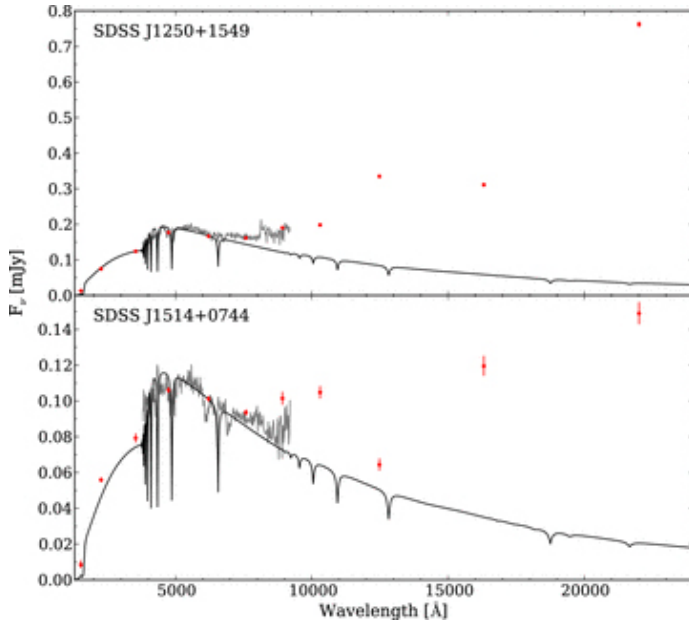


Figure 4-3.: SED of members of the pilot sample. Plotted are: the measured photometry from GALEX, SDSS and UKIDSS as red dots with their corresponding error bars, the SDSS spectrum as a grey line and a 10000 K non-magnetic hydrogen-rich white dwarf model as a solid black line (Breedt et al. 2012).

Table 4-1.: Relevant properties of our pilot sample of magnetic period-bouncers.

Name	d [pc]	P_{orb} [min]	SpT _{donor}	B_{WD} [MG]	References
V379 Vir	153^{+2}_{-3}	88.4	L5-L8	7	Farihi et al. (2008)
SDSS 1514	182^{+8}_{-6}	88.7	L3-	36	Breedt et al. (2012), Külebi et al. (2009)
SDSS 1250	131^{+2}_{-2}	86.3	M8-	20	Breedt et al. (2012), Külebi et al. (2009)

et al. (2011) from comparing the absolute JH band magnitude of the system to the observed absolute JH band magnitudes of M, L and T dwarfs. At this spectral type the secondary of SDSS 1250 would be slightly above the substellar limit on the donor sequence of Knigge (2006). However, the photometry used to estimate the donor spectral type was considered uncertain by Steele et al. (2011) because the J -band data was flagged as noise in the UKIDSS archive, making a spectroscopic confirmation mandatory for this system.

Some relevant system properties are summarized in Table 4-1. The systems are identified by their shortened SDSS name or variable star designation, with information on their distance obtained from Bailer-Jones et al. (2021), the orbital period derived by different authors using the $H\alpha$ emission line, the estimated spectral type of the donor as described above, the estimated white dwarf magnetic field strength, and their corresponding references.

In order to gain more information about the white dwarf in these systems, an estimate for the individual white dwarf radii and masses was performed (Muñoz-Giraldo et al. (2023)). For this purpose, hydrogen-rich (DA) white dwarf atmosphere models by Koester (2010) were

fitted to the SDSS spectra¹ of the period-bounce candidates in the pilot sample considering values for T_{eff} and $\log(g)$ previously reported in the literature (Fig. 4-4). Because these systems contain magnetic white dwarfs and the models do not consider magnetic fields, the Balmer lines cannot be used, such that the fits rely solely on the continuum.

The fit has a single parameter, the ratio between the observed flux from the SDSS spectrum and the model surface flux, because the other model parameters (T_{eff} and $\log(g)$) were drawn from the literature. This flux ratio represents the dilution factor, $(d/R_{\text{WD}})^2$ where d is the distance and R_{WD} the white dwarf radius. Therefore, given the distance, the white dwarf radius can be found. From the radius and an appropriate mass-radius relation the white dwarf mass can be obtained.

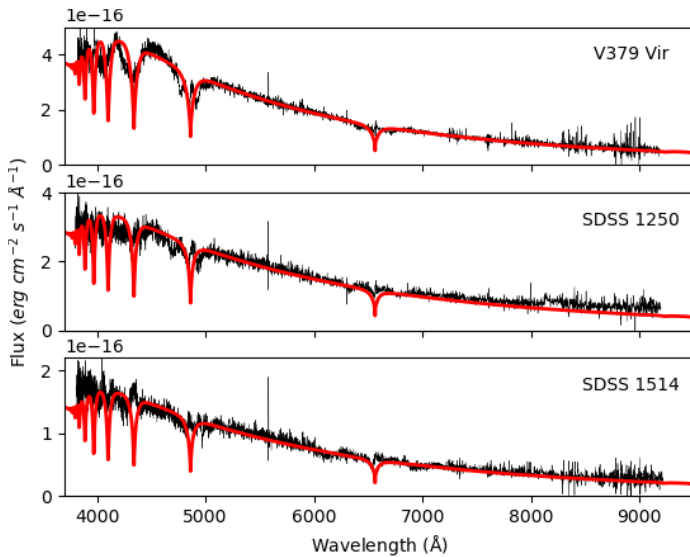


Figure 4-4.: SDSS spectra of the three members of the pilot sample (in black) with the corresponding Koester (2010) model discussed in this thesis (in red).

For SDSS 1514 and SDSS 1250 a $T_{\text{eff}} = 10000$ K DA white dwarf with $\log(g) = 8.0$ was assumed (see bottom two panels of Fig. 4-4), corresponding to the parameters derived by Breedt et al. (2012) using the same SDSS spectra. With the Bailer-Jones et al. (2021) distances from Table 4-1 a white dwarf radius of 7.0×10^8 cm for SDSS 1514 and of 7.2×10^8 cm for SDSS 1250 was obtained, which, using the mass-radius relation by Nauenberg (1972), results in white dwarf masses of $0.80M_{\odot}$ and $0.77M_{\odot}$, respectively.

For V379 Vir a $T_{\text{eff}} = 11000$ K DA white dwarf with $\log(g)=8.0$ was assumed (see top panel of Fig. 4-4) following the white dwarf temperature obtained by Burleigh et al. (2006) for the same SDSS spectrum and assuming the $\log(g)$ of the other systems in our pilot sample. With the Bailer-Jones et al. (2021) distance from Table 4-1 a white dwarf radius of 8.3×10^8 cm was obtained, and from this value a white dwarf mass of $0.64M_{\odot}$ was derived using the mass-radius relation by Nauenberg (1972).

¹<https://dr9.sdss.org/>

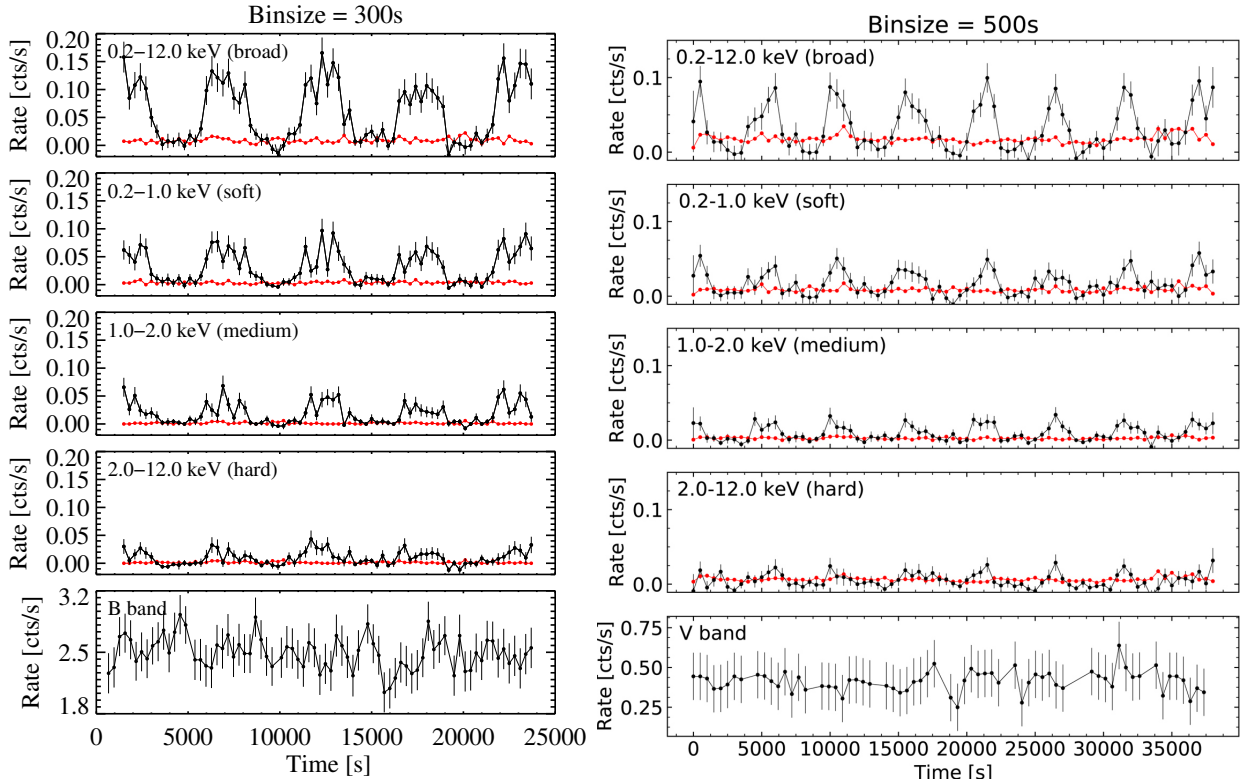


Figure 4-5.: EPIC/pn X-ray light curve in four energy bands and OM light curve. The X-ray light curves represent the background-subtracted source signal (black), and the background signal (red) is included for comparison. **Left panel:** Light curves for V379 Vir (Stelzer et al. 2017). **Right panel:** Light curves for SDSS 1514 (Muñoz-Giraldo et al. 2023).

4.1.2. XMM-Newton detections

XMM-Newton with its EPIC/pn detector was used to study the pilot sample of period-bounce candidates as it offers the largest collecting area of the existing X-ray instruments. Only two members of the pilot sample, V379 Vir (Obs-ID 0760440101; PI Stelzer) and SDSS 1514 (Obs-ID 0840380201; PI Stelzer), have *XMM-Newton* data available. The remaining member, SDSS 1250 (Prop-ID 092123; PI Muñoz-Giraldo), is part of an accepted *XMM-Newton* proposal with its observation still pending.

As seen in Fig. 4-5, Stelzer et al. (2017) detected X-ray orbital modulation (see Sect. 3.3) on V379 Vir from the *XMM-Newton* observation, proving that the system is accreting, and thus confirming it as a period-bounce polar. Through modelling of the X-ray spectrum (Fig. 4-6), Stelzer et al. (2017) derived an X-ray luminosity of $\sim 3 \times 10^{29}$ erg/s that, using a white dwarf mass of $0.64M_{\odot}$ and a radius of 8.3×10^8 cm (see Sect. 4.1.1), yielded when using Eq. 3-2 an updated instantaneous mass accretion rate in the system of $9.1 \times 10^{-14} M_{\odot}/\text{yr}$. The estimated value for the wind driven mass accretion rate in this system ($\sim 10^{-17} M_{\odot}/\text{yr}$; Wood et al. 2015,

Stelzer et al. 2017) is orders of magnitude too weak to explain the observed instantaneous mass accretion rate. Additionally, donor stars in cataclysmic variables are typically oversized as they are driven out of thermal equilibrium due to mass transfer (see Sect. 1.1), making Roche-lobe overflow the most likely accretion mechanism.

This result is specially important as V379 Vir had been suggested as a possible detached system (Schmidt et al. 2005, Debes et al. 2006). However, thanks to X-ray detections using *Swift* (Burleigh et al. 2006) and *XMM-Newton* (Stelzer et al. 2017), as well as the system parameters derived from them, V379 Vir was proven to be an interacting binary, and one of the first confirmed magnetic period-bouncers.

Similar to V379 Vir, as seen in Fig. 4-5, this thesis presents the detection of X-ray orbital modulation on SDSS 1514, proving that there is accretion happening in this system as well (Muñoz-Giraldo et al. 2023). The EPIC/pn spectrum of SDSS 1514 was fitted using a single temperature component APEC model (see Sect. 3.3). The best-fit model corresponded to a plasma temperature $kT = 3.7_{2.5}^{5.9}$ keV, global elemental abundances $Z = 0.04_{0.00}^{0.71} Z_{\odot}$, and an emission measure $EM = 2.2_{1.7}^{2.5} \times 10^{51} \text{ cm}^{-3}$. Through the best-fit to the X-ray spectrum (Fig. 4-6), an X-ray luminosity of $\sim 3 \times 10^{29} \text{ erg/s}$ was derived using Eq. 3-1 (Muñoz-Giraldo et al. 2023) that, using a white dwarf mass of $0.8 M_{\odot}$ and a radius of $7 \times 10^8 \text{ cm}$ (see Sect. 4.1.1), yields when using Eq. 3-2 an instantaneous mass accretion rate in the system of $3.3 \times 10^{-14} M_{\odot}/\text{yr}$. Despite the lack of a spectroscopically detected donor in this system, the considerable similarities shared by SDSS 1514 and V379 Vir, including their X-ray properties, suggests that SDSS 1514 is a magnetic period-bouncer as well.

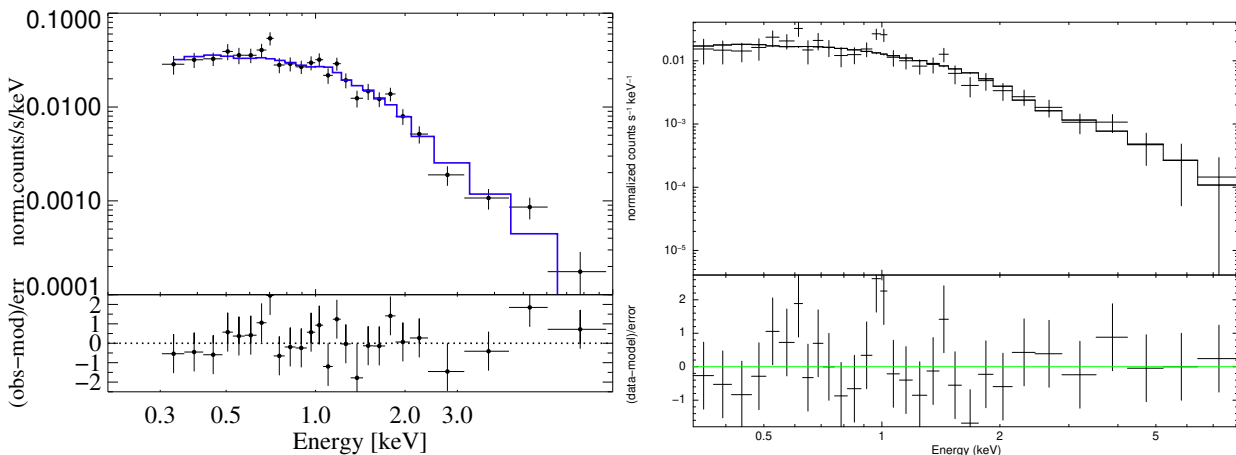


Figure 4-6.: Time-averaged EPIC/pn X-ray spectrum with the best-fit APEC model and residuals. **Left panel:** Spectrum of V379 Vir (Stelzer et al. 2017). **Right panel:** Spectrum of SDSS 1514 (Muñoz-Giraldo et al. 2023).

4.1.3. SRG-eROSITA detections

As explained in Sect. 3.2.2 the X-ray detection of period-bouncers as a population has not been very successful mainly due to the lack of coverage and sensitivity of current and past instruments. As an all-sky survey with sufficient sensitivity, eROSITA provides an unprecedented opportunity to not only study individual period-bouncers but to search for the missing population of these systems. In the framework of this thesis, in Muñoz-Giraldo et al. (2023) the first ever detections of period-bouncers with eROSITA were presented.

To obtain the highest sensitivity for detecting the presumably faint period-bouncers, the merged catalog eRASS:3 was used, which is the result of summing data from the first three all-sky surveys of eROSITA. The version of the eRASS:3 catalog used was the one made available in December 2022 to the German eROSITA consortium, and it was produced with the data processing version 020². Source detection was performed for this catalog in a single eROSITA energy band, 0.2 – 2.3 keV.

In order to search for the pilot sample of period-bounce candidates in eRASS data, an initial match between the three targets and the *Gaia*-DR3 catalog was performed. Using the corresponding *Gaia*-DR3 proper motions, the coordinates of the objects were corrected to the mean observing date of eRASS:3. Then, the corrected coordinates were matched with the eRASS:3 catalog, allowing for a maximum separation of 30". After establishing the closest matches for the pilot sample, a visual inspection was carried out in a 30" radius region around the X-ray source to confirm that indeed there were no other potential optical *Gaia* counterparts. Two of the members of the pilot sample have eROSITA detections, V379 Vir and SDSS 1250, while for SDSS 1514, which is located in the sky area with exclusive Russian eROSITA data rights, no data is available to me.

For the eROSITA catalogs, the reported flux was calculated from the count rate using a power law model with an index $\Gamma = 2.0$ and a galactic absorption of $N_H = 3 \times 10^{20} \text{cm}^{-2}$ (Brunner et al. 2022). As was covered in Sect.3.3, eROSITA cannot measure astrophysical fluxes directly, but rather uses a ECF dependent on the spectral model and instrument to convert the measured count rate into a flux. Most of the X-ray sources studied with eROSITA are active galactic nuclei, the X-ray spectrum of which typically follows a power-law distribution (Liu et al. 2022a). On the other hand, cataclysmic variables have thermal spectra, not power-law spectra (see Sect.3.3 for more details). Since the power-law spectral model assumed in the eROSITA catalogs is not appropriate for cataclysmic variables, fluxes for an APEC model were computed with help of a simulation that provided the eROSITA conversion factor, $CF_{\text{eROSITA,APEC}}$, from count rate to thermal flux.

To this end, a “fake” spectrum was generated using the eROSITA response files (RMF and ARF; see Sect. 3.3) for two different types of models: a power law and an APEC spectral model (specific parameters for each of them are described in Muñoz-Giraldo et al. (2023)). From both synthetic spectra, the flux and the count rate in the 0.2 – 2.3 keV eROSITA band

²The source catalog used in our work is all_s3_SourceCat1B_221007_poscorr_mpe_clean.fits (for eRASS:3).

were retrieved, using these values to calculate a $CF_{\text{fake,APEC}}$ and a $CF_{\text{fake,powerlaw}}$. The ratio between these two conversion factors from the simulation ($CF_{\text{fake,powerlaw}}/CF_{\text{fake,APEC}} = 0.97$) can be used with the eRASS:3 catalog $CF_{\text{eRASS:3,powerlaw}}$, calculated from the count rate and flux reported in the catalog, to derive $CF_{\text{eRASS:3,APEC}}$. The final APEC fluxes from eROSITA, of the two members of the pilot sample located in the ‘‘German sky’’, are reported as the first two systems in Table 4-2. The reported X-ray luminosity and instantaneous mass accretion rate were calculated using the Bailer-Jones et al. (2021) distances from Table 4-1 and the white dwarf mass from Sect. 4.1.2.

Table 4-2.: X-ray parameters from the eROSITA merged catalog, eRASS:3, for V379 Vir and SDSS 1250 given for the eROSITA band (0.2-2.3 keV). X-ray parameters for SDSS 1514 are converted from the *XMM-Newton* band (0.2-12keV) to the eROSITA band (0.2-2.3 keV).

Name	Flux (APEC) [erg cm ⁻² s ⁻¹]	X-ray luminosity* [erg s ⁻¹]	Mass accretion rate* [M _⊙ yr ⁻¹]
V379 Vir	7.47×10^{-14}	log(L _x)= 29.5	2.1×10^{-14}
SDSS 1250	4.58×10^{-14}	log(L _x)= 29.2	1.0×10^{-14}
SDSS 1514	4.21×10^{-14}	log(L _x)= 29.3	1.7×10^{-14}

* Values do not consider potential contributions from cyclotron emission to the X-ray luminosity.

Similar to SDSS 1514, SDSS 1250 also lacks a spectroscopically detected donor. However, its overall characteristics as well as its X-ray emission are very similar to those of V379 Vir, suggesting that SDSS 1250 is a period-bouncer as well.

From Table 4 in Muñoz-Giraldo et al. (2023) it can be seen that the detected period-bouncers are faint, with only tens of counts in the merged data from the first three eROSITA surveys. However, with a detection likelihood of 44.5 for V379 Vir and 19.9 for SDSS 1250, they are significantly above the detection likelihood limit of five set for the eRASS:3 merged catalog which corresponds to the probability of the source being spurious and consistent with background fluctuations (Liu et al. 2022b). This confirms eROSITA as a suitable instrument for the study of period-bouncers and for the potential identification of the missing population of this faint sub-class of cataclysmic variables.

We can use these results as a reference in future X-ray studies of period-bouncers. In order to have homogeneous data on all the members of the pilot sample, V379 Vir, the only period-bouncer with data from both *XMM-Newton* and eROSITA, can be used to convert the flux of SDSS 1514 from a *XMM-Newton* band (0.2-12 keV) to the eROSITA band (0.2-2.3keV). For this transformation we use the ratio of 0.57 between the reported fluxes of V379 Vir in the *XMM-Newton* band (1.30×10^{-13} erg cm⁻² s⁻¹; Stelzer et al. 2017) and the eROSITA band

($7.47 \times 10^{-14} \text{erg cm}^{-2} \text{s}^{-1}$; Table 4-2). This ratio is then applied to the *XMM-Newton* flux of SDSS 1514 ($7.33 \times 10^{-14} \text{erg cm}^{-2} \text{s}^{-1}$; Muñoz-Giraldo et al. 2023) to obtain an estimated eROSITA flux. The X-ray luminosity and mass accretion rate of SDSS 1514 calculated using this estimated flux are reported in Table 4-2.

The detailed study of this pilot sample of magnetic period-bouncers in the eROSITA band (0.2-2.3 keV) resulted in a mean X-ray flux of $5.42_{-1.21}^{+2.05} \times 10^{-14} \text{erg cm}^{-2} \text{s}^{-1}$ (with SDSS 1514 as the system with the lowest X-ray flux), a mean bolometric X-ray luminosity of $\log(L_x)[\text{erg/s}] = 29.3_{-0.1}^{+0.2}$ (with SDSS 1250 as the faintest system) and a mean instantaneous mass accretion rate of $1.6_{-0.6}^{+0.5} \times 10^{-14} M_{\odot}/\text{yr}$ (with SDSS 1250 as the system with the lowest value). According to the standard evolution track of cataclysmic variables by Knigge et al. (2011), in the post-bounce area cataclysmic variables exhibit X-ray luminosities of $\log(L_x)[\text{erg/s}] = 29.3_{-0.6}^{+0.5}$, which fits very well with both results (*XMM-Newton* and eROSITA) for the pilot sample of magnetic period-bouncers, and secular mean mass accretion rates of $1.6_{-0.8}^{+0.7} \times 10^{-11} M_{\odot}/\text{yr}$ which is considerably larger than the instantaneous mass accretion rates obtained from X-ray data.

4.2. Catalogue of Known Cataclysmic Variables Around the Period-bounce

With the goal of characterizing a wider sample of period-bouncers, as well as identifying new members of this population in the framework of this thesis, a catalog of literature published cataclysmic variables around the period-bounce was compiled. In Muñoz-Giraldo et al. (2024) previous theoretical studies of period-bouncers are used to construct a “scorecard” that reliably predicts the likelihood that a system has of being a period-bouncer. Using the results of the “scorecard” together with the results of typical X-ray parameters from the analysis of eROSITA data for the confirmed period-bouncers has yielded the identification of 12 systems as new period-bouncers, a $\sim 70\%$ increase in the overall population.

4.2.1. Constructing the Catalog

When constructing the catalog of cataclysmic variables around the period bounce (Fig. 4-7) two main selection parameters were used: the system should have a short orbital period ($P_{\text{orb}} \leq 90\text{min}$) and a low donor mass ($M_{\text{donor}} \leq 0.07M_{\odot}$). However, considering how uncertain the defining characteristics of period-bouncers are, due to the lack of a large representative population, I decided not to strictly enforce these parameters. This is relevant specially for 32 systems that were suspected in the literature of being period-bouncers, but do not have information on either orbital period/donor mass or both.

Some of the reasons given in the literature to suggest a system as a period-bouncer without information on their orbital period or donor mass are: presence of a very cool white dwarf in

the system (V1258 Cen; Pala et al. 2022), as well as similarities to confirmed period bouncers in their optical spectra (CXOXB J143435.3+334048 and Gaia DR3 1705302990918074880 amongst other systems; Inight et al. 2023a) and photometric light curve of their superoutburst (ASASSN -16hg and CRTS J173516.9+154708 amongst other systems; Kimura et al. 2018).

The catalog includes two systems, V1258 Cen and EF Eri, that are notoriously known for having been proposed as potential period-bouncers, but were subsequently rejected after a detailed study. V1258 Cen was initially suggested as a potential period-bouncer by Pala et al. (2022) solely due its very cool white dwarf. However, this argument was invalid as Savoury et al. (2012), through a detailed study, had already established the orbital period (128min) and donor mass of the system (between $0.12 M_{\odot}$ and $0.20 M_{\odot}$), which firmly places it just below the period gap. The nature of EF Eri is more ambiguous, as it has an orbital period that locates it near the period minimum for cataclysmic variables (81min, Schwöpe and Christensen 2010) and the presence of a degenerate donor in the system that is still debated. Schwöpe and Christensen (2010) favored a degenerate donor based on its estimated J -band brightness and the semi-empirical donor sequence of Knigge (2006). However, with *Gaia*-DR3 the distance to EF Eri was revised to a much larger value, increasing the estimated absolute magnitude of the donor above the substellar limit and, thus, weakening the arguments for a degenerate donor in the system. The motivation for including these systems in the catalog was to be able to compare their multi-wavelength characteristics to those of confirmed period-bouncers, which will further help in the differentiation between high likelihood and low likelihood period-bounce candidates.

In Muñoz-Giraldo et al. (2024) a catalog of cataclysmic variables around the period-bounce made of 192 systems was presented. Since its publication an additional 21 systems have been added (see Table A-1) for an updated total of 213 systems in the catalog. One of these new systems, GALEX J041130.0+685350, is a recently eROSITA-discovered period-bouncer with a spectroscopically detected donor of SpT T3 (Galiullin et al. 2024).

4.2.2. Scorecard for Likelihood of Being a Period-Bouncer

As mentioned in Sect. 1.3.1, a significant number of short-period cataclysmic variables, usually classified as WZ Sge, have been detected primarily through photometric studies of optical superoutbursts in their light curves. These systems are, therefore, not easily observed in quiescence due to their faintness, such that the lack of information available, specially of the orbital period and donor mass, makes a straightforward classification as a period-bouncer challenging. I attempted to remedy this by defining a “scorecard” which does not completely rely on the knowledge of the orbital period and donor mass in order to accurately judge if a system is a period-bouncer.

This “scorecard” is composed of ten parameters that were constructed following literature expectations for period-bouncers. A numerical score was assigned to each individual para-

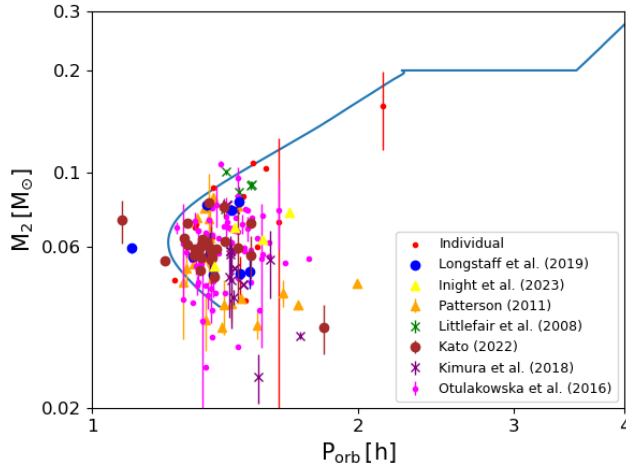


Figure 4-7.: Donor mass as a function of orbital period for 175 systems in Muñoz-Giraldo et al. (2024) catalog of cataclysmic variables around the period-bounce, and the additional 6 systems introduced in this thesis that had reported values. Their respective literature sources are listed in the legend. The standard evolution track is shown in blue as reference (Knigge et al. 2011).

meter that was then combined into a final numerical score for each system in the catalog. The maximum number of achievable score points is 36, corresponding to an object that has the highest score in all ten parameters, and therefore, a final score of 100 %. However, a considerable number of candidates did not have enough data to be scored in all of the ten parameters making a direct comparison between systems difficult. To solve this problem, for each individual object, the final score of 100 % was re-defined as the maximum number of points that it would have received if it had the highest likelihood of being a period-bouncer in every parameter for which it has available data. The percentage final score is then calculated as the ratio between the actual points the system has and its maximum achievable points. Here a brief overview of the parameters is presented, but a complete description can be found in Muñoz-Giraldo et al. (2024):

1. Spectral type of donor (SpT in Table 4-3): Parameter with the most weight in the “scorecard” considering that a spectroscopic detection of a late-type donor in a cataclysmic variable is the ultimate proof needed to securely confirm the system as a period-bouncer. Partial points are awarded to systems that have a photometric detection of the donor, as it is not as conclusive as an spectroscopic detection, as well as to systems with an uncertain spectral type for the donor just at the point of the period-bounce, usually reported in the literature as M5-or-later.
2. Donor mass (M_{Donor} in Table 4-3): According to the evolution tracks for cataclysmic variables by Knigge et al. (2011), the period-bounce area is defined for cataclysmic variables with a donor mass lower than $0.058M_{\odot}$. Partial points are awarded to systems with a donor mass up to $0.07M_{\odot}$, placing them just at the point of period-bounce.

3. Orbital period (P_{orb} in Table **4-3**): This parameter judges the proximity of the cataclysmic variable to the observed period minimum (81.8 min; Gänsicke et al. 2009) depending on their donor mass. This is because different cataclysmic variables with the same orbital period could be located in the pre-bounce or post-bounce area solely due to the donor mass.
4. White dwarf temperature (T_{WD} in Table **4-3**): Cataclysmic variables are known to contain white dwarfs that cool during the evolution of the system. This means that period-bouncers, the last stage in the evolution of cataclysmic variables, should have very low-temperature white dwarfs (≤ 12500 K; Pala et al. 2022).
5. *Gaia* variability (G_{var} in Table **4-3**): Due to the very low mass accretion rates exhibited by period-bouncers, they are expected to undergo outbursts or superoutbursts only once every decade (Patterson 2011), such that observations of these systems most likely happen when they are in a quiescent non-variable state.
6. *Gaia* colors (*Gaia* in Table **4-3**): Period-bouncers composed by a cool white dwarf and a very late-type donor are expected to appear in optical bands as single white dwarfs, usually located in the *Gaia* color-magnitude diagram in the area corresponding to the white dwarf locus or just above it (Santisteban et al. 2018).
7. SDSS colors (SDSS in Table **4-3**): Similar to the *Gaia* colors parameter, period-bouncers are expected to be located in the area corresponding to the white dwarf locus or just above it in the SDSS color-color diagram (Inight et al. 2023a).
8. Ultraviolet colors (UV in Table **4-3**): In ultraviolet bands the emission from period-bouncers is dominated by the white dwarf, where GALEX colors are a sensitive probe of the white dwarf’s effective temperature (Patterson 2011).
9. Infrared colors (IR in Table **4-3**): The position of a system in the infrared color-color diagram can give information about the spectral type of the donor. Littlefair et al. (2003) established areas for cataclysmic variables with early-type donors, as well as areas populated by L or T donors which are the expected companions of period-bouncers.
10. Infrared excess (Excess in Table **4-3**): Due to the evolved nature of the donor in period-bouncers, it is expected to appear as a very slight or no excess in the infrared. Specifically when analysing the spectral energy distribution of confirmed period-bouncers, this infrared excess should be evident only at longer wavelengths associated to the *K*-band or the WISE bands, if they present an excess at all.

The values obtained from all individual parameters considered in the scorecard and the final score are reported in Table **4-3** for the 21 new systems, as an addition to the final scores

Table 4-3.: Scorecard for the 21 new systems in the catalog of cataclysmic variables around the period-bounce. See Sect. 4.2.2 and Muñoz-Giraldo et al. (2024) for explanations on the different parameters and scores.

System	SpT	M _{Donor}	P _{orb}	T _{WD}	G _{var}	Gaia	SDSS	UV	IR	Excess	%
ASASSN -14dx			1	3		2	3	0	3	3	71
OT J21380+2619		1	2	0	3	2	1	0	0	1	37
SDSS J09290+0053	5						0				-
SDSS J00581-0107		1	0				0				-
EQ Lyn			1	0	3	2	0			3	50
SDSS J07550+1435			1	0	3	3	3	0		3	62
FV Lyn				3	3	3	3	0		3	83
LV Cnc			1	3	3	3	3	0	3	3	79
1RXS J10142+0638			1	3	3	3	3	3	3	3	92
SDSS J14575+5148		1	3	1	2	3	1		3		67
V386 Ser			1	3	3	3	3			3	89
QZ Aqr		0	0				3				-
SDSS J21414+0507			1	3	3	3	3	0		3	76
OT J23111+0130		3	3				0				-
VY Aqr	5	1	0	0	1	2	1	0	0	3	36
ZTF19acfixfe			1		3		0				-
GALEX J04113+6853	9	1.5	0	1	3	3		0			65
eFEDS J09261+0105			1		3	2	1	0		3	56
2QZ J14283+0031				3	3	3		0	1	3	72
GALEX J18113+7956				3	3	2		0		3	73
ATO J026.6+49.2	7			3	3	3			0	3	79

reported by Muñoz-Giraldo et al. (2024) (see their Table 3) for the original 192 systems included in the catalog of cataclysmic variables around the period-bounce. Overall, 5 of the 21 new systems had information for only three or fewer parameters, meaning that a final score was not assigned to them and they have been excluded from the following analysis.

Even after the addition of GALEX J041130.0+685350, the new eROSITA-confirmed period-bouncer, V406 Vir remains the lowest scoring confirmed period-bouncer at 64%, meaning that the definition for the category of high likelihood of being a period-bouncer established by Muñoz-Giraldo et al. (2024) stays the same. Now, 76 systems (12 newly reported in this thesis and 64 presented by Muñoz-Giraldo et al. 2024) have a final score greater than 60%, meaning that they are strong period-bounce candidates that have not yet been categorized as such.

A good indicator of the performance of the scorecard is that the category of low likelihood of

being a period-bouncer includes systems that are well known for not being period-bouncers (V1258 Cen; Savoury et al. 2012), as well as the ambiguous system EF Eri.

In Table 4-4 the completeness and accuracy of each of the ten scorecard parameters is shown for two populations: case 1 made of 18 confirmed period-bouncers (see Sect. 2), and case 2 made of 30 confirmed and new period-bouncers (see Sect. 4.2.3). Completeness refers to the percentage of confirmed period-bouncers that were successfully classified as period-bouncers using the highest score for the parameter. Accuracy refers to the percentage of systems with the highest score for the parameter which are actually period-bouncers, and is a measure for the “contamination” of the sample.

Table 4-4.: Significance of scorecard parameter. All numbers indicate percentages.

		SpT	M _{Donor}	P _{orb}	T _{WD}	G _{var}	<i>Gaia</i>	SDSS	UV	IR	Excess
(1)	Completeness	50	61	72	61	95	88	78	50	58	88
	Accuracy	90	18	19	18	17	26	12	35	37	15
(2)	Completeness	47	60	61	67	97	83	81	43	53	93
	Accuracy	90	25	25	33	29	42	21	53	53	25

(1) For previously known confirmed period-bouncers (see Sect. 2).

(2) For previously known confirmed and new period-bouncers identified through this thesis work (see Sect. 4.2.3).

These ten parameters were constructed following expectations for period-bouncers established in the literature, which describe an ideal of what is regarded as a period-bouncer. From the completeness of both populations, it can be observed that the expectations of an ideal period-bouncer describe around half or more of the actual population of confirmed period-bouncers (case 1 in Table 4-4). From the accuracy of the confirmed period-bouncers, case 1 in Table 4-4, it can be observed that the expectations of an ideal period-bouncer (with the exception of the spectral type of the donor) also describe a considerable number of systems that have not been confirmed as period-bouncers. The accuracy is considerably increased with the addition of the newly eROSITA confirmed period-bouncers (see Sect. 4.2.3) which suggests that there are systems amongst the “contaminants” which are waiting to be confirmed as period-bouncers.

As expected, the parameter with the highest accuracy is the “spectral type of the donor”, considering that a spectroscopic detection of a late-type donor in a cataclysmic variable is the ultimate confirmation that the system is a period-bouncer. However, the completeness of this parameter is at most 50% mainly due to the lack of spectroscopic confirmation of the late-type donor in several confirmed period-bouncers (see Sect. 2). “Ultraviolet colors” and “infrared colors” are the parameters with the second highest accuracy, with the majority of short-period cataclysmic variables that fulfill these selection cuts being actual period-bouncers.

The parameter that performs the best overall is “*Gaia* colors”, as it manages to retrieve 83% of confirmed and new period-bouncers while also including amongst the least amounts of “contaminants”. According to this, it is likely that a cataclysmic variable with *Gaia* colors locating it within the white dwarf locus, as defined by the bounds presented in the scorecard, is indeed a period-bouncer.

Considering that they are able to recover the majority of already confirmed period-bouncers (completeness in Table 4-4), while at the same time accurately identifying candidates that are actual period-bouncers (accuracy in Table 4-4), the most useful and relevant parameters when deciding if a cataclysmic variable is a period-bouncer are: spectral type of the donor, *Gaia* colors, ultraviolet colors and infrared colors.

4.2.3. SRG-eROSITA detections

In Sect. 4.1.3 the first ever X-ray results from period-bouncers using eROSITA were reported. Based on this work, I expanded the study on the catalog of known cataclysmic variables around the period-bounce introduced earlier in this chapter.

The sky distribution of all 213 systems in the catalog of cataclysmic variables around the period-bounce is shown in Fig. 4-8, including 192 systems previously presented in Muñoz-Giraldo et al. (2024) and 21 new systems introduced in Sect. 4.2.1. The summary of the different compositions of the catalog is presented in Table 4-5.

As discussed in Sect. 3.2.2, data access for the German consortium is only provided for the western half of the sky in terms of Galactic coordinates (Galactic longitude $l \geq 180^\circ$ shown in Fig. 4-8). The eRASS:3 catalog introduced in Sect. 4.1.3 was used, considering that not only does it provides the highest sensitivity for the detection of faint period-bouncers, but it also allows for a comparison with a compiled catalog of cataclysmic variable candidates (Schwope et al. prep). Similar to the procedure presented in Sect. 4.1.3 the coordinates of the 213 systems in the catalog of cataclysmic variables around the period-bounce were corrected to the mean observing date of eRASS:3 using their *Gaia*-DR3 proper motions. A match with the eRASS:3 catalog was performed, allowing for a maximum separation of $30''$ and enforcing for the separation between optical and X-ray coordinates the condition $\text{sep}_{\text{ox}} < 3 \times \text{RADEC_ERR}$, where RADEC_ERR is the positional error of the X-ray coordinates in units of arcseconds. I found that 55 of the 86 systems from the catalog which are in the German eROSITA sky are detected in the eRASS:3 catalog, 5 are new systems introduced in this thesis and 50 were already presented by Muñoz-Giraldo et al. (2024). The remaining 31 undetected systems (grey dots in Fig. 4-8) were, for the most part, identified and studied as they were experiencing superoutbursts (e.g. V498 Hya by Kato et al. (2009), CRTS J075418.7+381225 by Nakata et al. (2014), ASASSN -15hn and CRTS J075418.7+381225 by Kato et al. (2016)). Because they are all located at large distances ($\sim 900\text{pc}$) it is expected that eROSITA would not detect them in a quiescent state.

The cross-match process was performed allowing for all possible matches within $30''$. Ho-

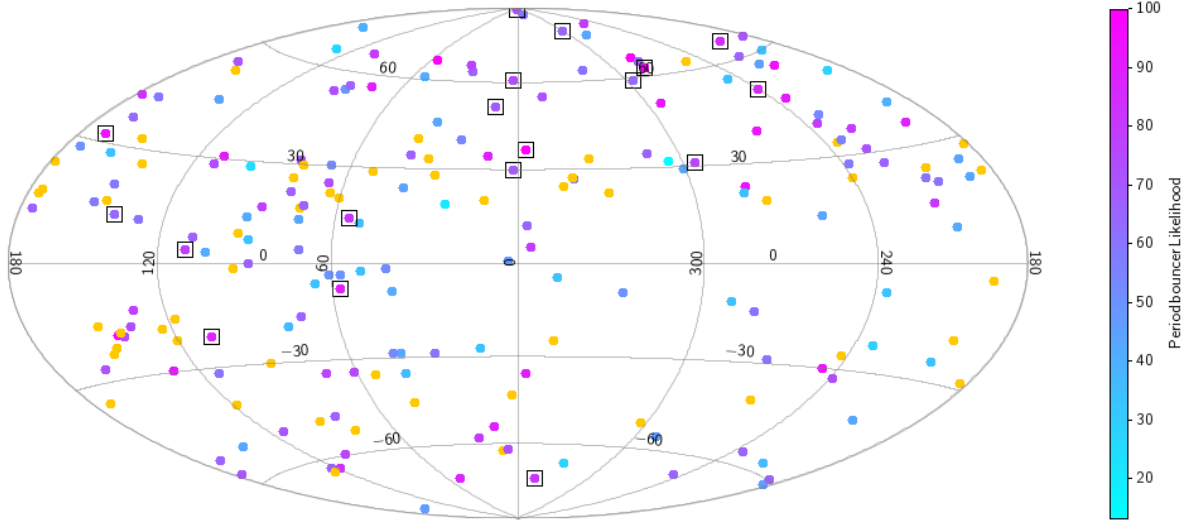
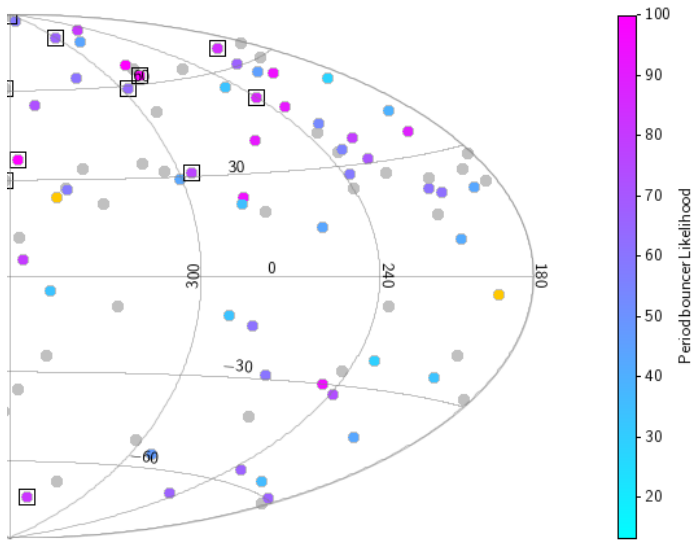


Figure 4-8.: Aitoff projection in Galactic coordinates. **Top panel:** Distribution of the 213 systems in the catalog of cataclysmic variables around the period-bounce.

The final score achieved by the systems is presented as a color scale, and candidates without enough information to have received a final score are presented in yellow. Previously known confirmed period-bouncers (Table 2-1) are highlighted with black boxes. **Left panel:** Distribution of the 86 systems located in the German eROSITA sky. The “eROSITA subsample” is shown in color scales, while systems without an eROSITA detection are shown in grey.



wever, each of the 55 detected systems had only one eRASS:3 match within that radius. A visual inspection was carried out using ESAsky³ in a 30'' radius region around the X-ray source to assure that there were no other potential optical counterparts that were located closer. Out of the 55 systems detected in the eRASS:3 catalog, 50 have no other optical source closer to the eRASS X-ray position than the target system in our catalog and can therefore be confidently categorized as a correct match. Of the remaining five systems with other possible optical counterparts, two systems were confirmed as having the correct match thanks to previous X-ray detections (*XMM-Newton* and *Chandra*) clearly associated with the target systems. For the last three systems the other possible optical counterpart is closer to the eRASS source than the target system, such that the X-ray source could not be securely associated with the period-bounce candidate, and therefore, was not reported by Muñoz-Giraldo et al. (2024). However, in their compilation of a catalog of known cataclysmic variables detected by eROSITA, Schwöpe et al. (2024) establishes that two of these X-ray sources are indeed associated with their corresponding target systems, meaning that only one out of these three systems remains un-associated to an X-ray source. The 54 systems in the catalog of cataclysmic variables around the period-bounce with a reliably associated X-ray source make up the “eROSITA subsample”, where the X-ray parameters of 47 systems in this “eROSITA subsample” were already presented by Muñoz-Giraldo et al. (2024). In Table 4-6 the X-ray parameters of the 7 sources from the “eROSITA subsample” with a newly established eROSITA detection are presented, all 5 new systems introduced in this thesis and 2 systems originally presented in Muñoz-Giraldo et al. (2024) but for which an eROSITA association could not be reliably determined at the time.

All 8 confirmed period-bouncers located in the sky area with German eROSITA data rights are amongst the “eROSITA subsample”, which were already presented by Muñoz-Giraldo et al. (2024). Additionally, there are 20 systems, four new systems introduced in this thesis, two with a recently established reliable counterpart, and 14 already presented by Muñoz-Giraldo et al. (2024) that even though they belong to the category of high likelihood of being a period-bouncer (see Sect. 4.2.2), they have not yet been classified as such. Considering that there are no new eROSITA-detected confirmed period-bouncers with available data, the X-ray selection cuts established by Muñoz-Giraldo et al. (2024) are maintained (see their Figures 7 and 8). These selection cuts were chosen to represent the areas typically occupied by eROSITA-detected confirmed period-bouncers and are defined as: a “X-ray luminosity cut” given by the bolometric X-ray luminosity (upper limit at $\log(L_x)[\text{erg/s}] \leq 30.4$ corresponding to the brightest eROSITA-detected confirmed period-bouncer CRTS J122221.6-311525) and *Gaia* colors (upper limit at $G_{BP}-G_{RP} \leq 0.35$ corresponding to the eROSITA-detected confirmed period-bouncer PM J12507+1549), and a “X-ray flux cut” given by the X-ray-to-optical flux ratio (upper limit at $\log(F_x/F_{opt}) \leq 0$ corresponding to the eROSITA-detected confirmed period-bouncer CRTS J122221.6-311525 and lower limit at $\log(F_x/F_{opt}) \geq -1.21$ corresponding to the eROSITA-detected confirmed period-bouncer

³<https://sky.esa.int/>

Table 4-5.: Catalog of known cataclysmic variables around the period-bounce.

	Systems presented by Muñoz-Giraldo et al. (2024)	New systems	Overall catalog
Total	192	21	213
eROSITA German sky	80	6	86
eROSITA-detected	50	5	55
“eROSITA subsample”	47	5+2*	54
In “eROSITA subsample”			
Confirmed period-bouncers	8	0	8
High likelihood of being a period-bouncer	14	4+2*	20
In high likelihood of being a period-bouncer			
Newly confirmed period-bouncers	7	3+2*	12

* These 2 systems were initially introduced by Muñoz-Giraldo et al. (2024), but no reliable cross-match could be determined at the time.

SDSS J103533.02+055158.4).

Table 4-6 shows if the new members of the “eROSITA subsample” fulfill these X-ray selection cuts. For systems that have a high score due to their multi-wavelength characteristics rated in the “scorecard”, which categorizes them as having a high likelihood of being period-bouncers, the fulfillment of the X-ray selection cuts leads to a classification of the system as a new period-bouncer. Out of the 7 new systems of the “eROSITA subsample”, 5 are confirmed as new period-bouncers bringing the total of eROSITA-confirmed new period-bouncers to 12 systems. All 5 newly confirmed period-bouncers were categorized as WZ Sge in the literature, with only two of them having previously been suggested as period-bounce candidates: WISE J111217.37-353829.1 (Patterson 2011) and PNV J17144255-2943481 (Kimura et al. 2018, Thorstensen 2020). Of the 20 systems in the “eROSITA subsample” that are part of the category of high likelihood of being a period-bouncer according to the “scorecard”, 12 could be successfully confirmed using eROSITA. This conclusively demonstrates not only the accuracy of the “scorecard” when selecting high likelihood period-bounce candidates, but also the usefulness of eROSITA-selected X-ray parameters in confirming these period-bounce candidates.

After the X-ray confirmation of 12 new period bouncers, the population of eROSITA-detected period-bouncers is now made up of 20 systems, representing an increase of $\sim 150\%$ in this population. When compared with the pilot sample of Sect. 4.1 the X-ray characteristics of this broader sample of period-bouncers seem to be relatively similar, with a mean bolometric X-ray luminosity of $\log(L_x)[\text{erg/s}] = 29.8^{+0.6}_{-0.7}$ (with SDSS J103533.02+055158.4 as the faintest system) and a mean instantaneous mass accretion rate of $5.6^{+9.6}_{-4.8} \times 10^{-14} M_\odot/\text{yr}$ (with SDSS

J103533.02+055158.4 as the system with the lowest value).

A comparison with the overall eROSITA-detected population of confirmed cataclysmic variables from Schwöpe et al. (prep) is presented in Fig. 4-9. The eRASS:3 sensitivity limit, marked by the red line in Fig. 4-9, is calculated for the limiting X-ray flux of 2×10^{-14} erg $\text{cm}^{-2} \text{s}^{-1}$ (Muñoz-Giraldo et al. 2023). Schwöpe et al. (prep) report the eROSITA detection of 585 confirmed cataclysmic variables, of which 171 are located within 500pc (blue line in Fig. 4-9), making confirmed period-bouncers $\sim 4\%$ and $\sim 11\%$ of these populations, respectively. These results are consistent with previous campaigns reporting an observed fraction of period-bouncers of 2.5% to 14% (Pala et al. 2020, Pala et al. 2022, Inight et al. 2023a). Even after the considerable increase in the population of period-bouncers that came as a result of this eROSITA study, period-bouncers are still far from being the major component of the cataclysmic variable population that is predicted in theoretical models.

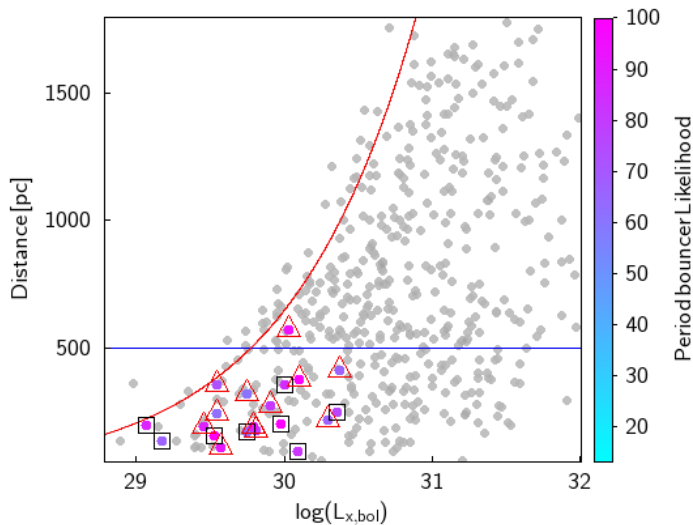


Figure 4-9.: Bolometric X-ray luminosity versus distance from Bailer-Jones et al. (2021) showing the position of previously confirmed (in black boxes) and new (in red triangles) period-bouncers detected by eROSITA with respect to the average eRASS:3 sensitivity limit marked by the red line. The final score achieved by the system is presented as a color scale. The population of eROSITA-detected confirmed cataclysmic variables from Schwöpe et al. (prep) is shown as a reference.

Table 4-6.: X-ray parameters for the 7 new systems in the “eROSITA subsample”. A checkmark is used to show which systems fulfill the X-ray selection cuts presented in Sect. 4.2.3 and Muñoz-Giraldo et al. (2024).

Parameter	WISE 1112*	PNV 1714*	SDSS 0755*	LV Cnc	RXS 1014*	eFEDS 0926	2QZ 1428*
Detection likelihood	6.7	56.7	8.2	5.5	53.1	123.0	6.0
sep _{ox} ["]	7.1	2.0	16.1	5.5	4.3	4.3	2.0
Counts [cts]	7.4±3.4	41.2±7.4	8.4±3.6	4.3±2.3	22.7±5.1	43.2±7.0	7.4±3.4
Count rate [cts/s]	0.02±0.01	0.12±0.02	0.04±0.02	0.02±0.01	0.10±0.02	0.19±0.03	0.02±0.01
Flux (APEC) ×10 ⁻¹⁴ [erg cm ⁻² s ⁻¹]	1.71±0.78	10.91±1.96	3.15±1.34	1.77±0.96	8.86±1.98	17.12±2.76	1.48±0.67
Distance [†] [pc]	571	176	240	196	191	385	352
X-ray luminosity log(L _x)[erg s ⁻¹]	30.0	29.8	29.5	29.1	29.8	30.7	29.5
Mass accretion rate ×10 ⁻¹⁴ [M _⊙ yr ⁻¹]	6.9	4.2	2.2	0.8	4.0	31.3	2.3
X-ray luminosity cut	✓	✓	✓	✓	✓	x	✓
X-ray flux cut	✓	✓	✓	x	✓	x	✓
Final score [%]	94	80	62	79	92	56	72

Object’s full name: WISE J111217.37-353829.1, PNV J17144255-2943481, SDSS J075507.70+143547.6, 1RXS J101421.4+063855, eFEDS J092614.1+010558 and 2QZ J142833.5+003100.

[†] From Bailor-Jones et al. (2021).

* System has been confirmed as a new period-bouncer using eROSITA selection cuts. See Sect. 4.2.3 for a discussion of these 5 systems.

4.3. Search for New Period-Bounce Cataclysmic Variables with eROSITA

With the detection of two faint confirmed period-bouncers reported by Muñoz-Giraldo et al. (2023) the sensitivity of eROSITA was proven sufficient for the study of period-bouncers (see Sect 4.1). This was exploited by Muñoz-Giraldo et al. (2024) in order to confirm new period-bouncers, significantly raising the number of systems in this population (see Sect. 4.2). However, as mentioned before, this increase is not enough to salvage the divide between the expected and observed population of period-bouncers. The success of these two projects has motivated the search for new period-bouncers using eROSITA.

As a starting point for the search of new period-bouncers, the *Gaia* Data Release 3 catalog of white dwarfs by Gentile Fusillo et al. (2021) is used, considering that, as detailed in Sect. 2.1, period-bouncers are very likely to appear like single white dwarfs in optical bands. Each object in the Gentile Fusillo et al. (2021) catalog has a corresponding probability of being a white dwarf (P_{WD}) calculated using as reference a sample of spectroscopically confirmed white dwarfs from SDSS. Gentile Fusillo et al. (2021) showed that selecting objects with $P_{\text{WD}} > 0.75$ recovers 96% of the spectroscopically confirmed white dwarfs from SDSS, as well as being able to recover 95% of the confirmed period-bouncers, making these “high-fidelity” white dwarfs an ideal starting sample for a search of new period-bouncers.

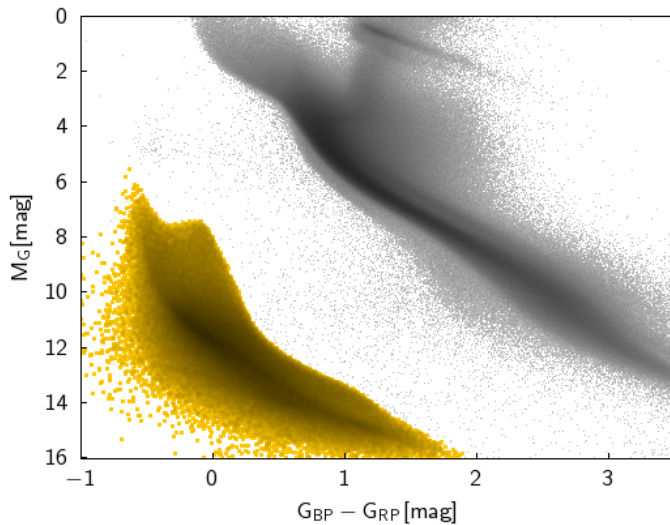


Figure 4-10.: *Gaia* color-magnitude diagram showing the position of “high-fidelity” white dwarfs from Gentile Fusillo et al. (2021). The *Gaia*-DR3 sources with Bailer-Jones et al. (2021) distances and a parallax error of less than 1% of the parallax value are shown in gray as a reference.

The sample of “high-fidelity” white dwarfs is made up of 359073 objects (yellow dots in Figs. 4-10) of which 187079 objects, roughly 52%, are located in the German eROSITA sky (yellow dots in Fig. 4-11). The same eRASS:3 catalog described in Sect. 4.1.3 and the same cross-match procedure from Muñoz-Giraldo et al. (2024) described in Sect. 4.2.3 are used to determine which of the “high-fidelity” white dwarfs in the German eROSITA sky have a reliable X-ray detection. This corresponds to 5514 objects (blue dots in Fig. 4-11), 1.5% of the original “high-fidelity” white dwarfs and 3% of those located in the German

eROSITA sky. The low detection fraction is not surprising considering that an eROSITA-detection of the faint X-ray emission coming from typical single white dwarfs making up the majority of this catalog is not expected. The sample of “high-fidelity” white dwarfs detected by eROSITA must therefore contain a range of different objects including, but not limited to, very hot white dwarfs or white dwarfs in complex configurations like AM CVn binaries and triple systems.

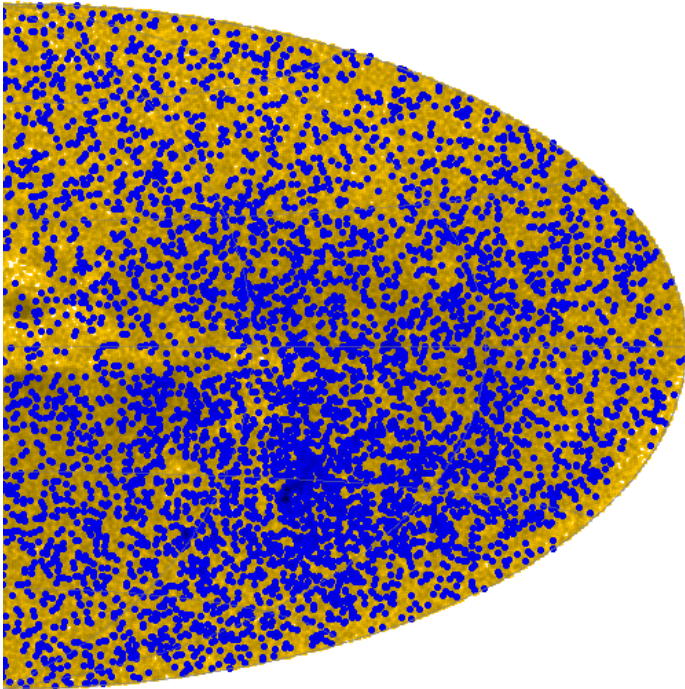


Figure 4-11.: Aitoff projection in Galactic coordinates of the distribution of “high-fidelity” white dwarfs located in the German eROSITA sky. “High-fidelity” white dwarfs with a detection in the eRASS:3 catalog are shown in blue.

A distance limit of 500pc was established in the search for new period-bouncers. This is initially motivated by the fact that all confirmed period-bouncers and almost all newly eROSITA-confirmed period-bouncers are located within 500pc (WISE J111217.37-353829.1 is the only exception with a distance of 571pc as seen in Fig. 4-9). Other considerations were: the limitation on the accuracy of distance measurements that can be achieved with *Gaia* for faint objects, as well as the eRASS sensitivity limit for the faintest confirmed period-bouncer (Muñoz-Giraldo et al. 2024). In Fig. 4-12 the 3833 “high-fidelity” white dwarfs located within 500pc in the German eROSITA sky are shown in pink. Around 70% of the “high-fidelity” white dwarfs detected by eROSITA are located close by and are probably related with faint X-ray emitting systems like period-bouncers.

As a last step, the X-ray selection cuts from Muñoz-Giraldo et al. (2024) are applied, which were derived using eROSITA-detected confirmed period-bouncers and already used to confirm new period-bouncers (see Sect. 4.2.3 for more information). The 1662 “high-fidelity” white dwarfs located within 500pc in the German eROSITA sky that fulfill both X-ray selection cuts are highlighted in Fig. 4-13, and are used to define a catalog of period-bounce candidates. The catalog of X-ray selected period-bounce candidates is made up of objects

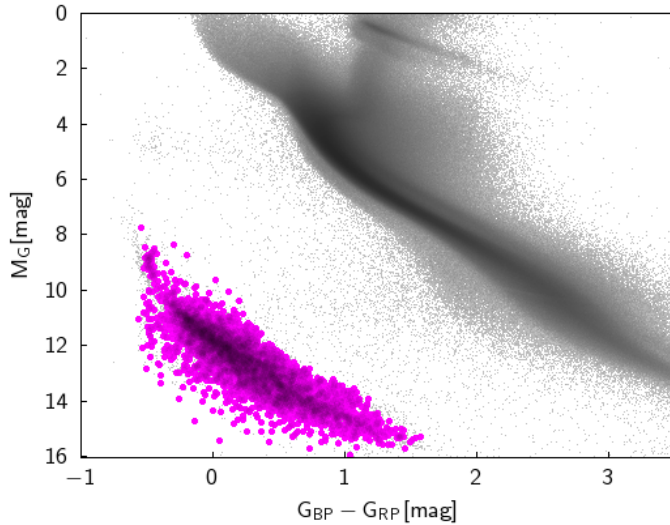


Figure 4-12.: *Gaia* color-magnitude diagram showing the position of “high-fidelity” white dwarfs from Gentile Fusillo et al. (2021) within 500pc and detected in eRASS:3. The *Gaia*-DR3 sources with Bailer-Jones et al. (2021) distances and a parallax error of less than 1% of the parallax value are shown in gray as a reference.

which have similar X-ray properties to that of confirmed period-bouncers and also resemble in the optical band spectroscopically confirmed white dwarfs.

As of now, the study of the 1662 members in the catalog of X-ray selected period-bounce candidates was started by compiling the final score for their likelihood of being a period-bouncer (see Sect. 4.2.2 and Muñoz-Giraldo et al. 2024). This ensures that not only they have X-ray properties similar to confirmed period-bouncers, but that their overall multi-wavelength characteristics resemble what we expect from period-bouncers.

Considering that the vast majority of these systems are not found in the literature, I do not have access to information about their orbital periods and the spectral type or mass of the donor, as these parameters typically come as a result of a detailed study. Therefore, a “reduced” version of the scorecard presented by Muñoz-Giraldo et al. (2024) is used including the following parameters: white dwarf temperature, *Gaia* variability, *Gaia* colors, SDSS colors, ultraviolet colors, and infrared colors. The final score was then calculated only taking these parameters into consideration (presented as a color scale in Fig. 4-13). I am confident that the results from the “reduced” scorecard are reliable as it includes *Gaia*, ultraviolet and infrared colors which, besides from the spectral type of the donor, are the most relevant parameters when identifying period-bouncers (see Table 4-4).

The final scores of the 1662 members in the catalog of X-ray selected period-bounce candidates seem to follow a trend, with the highest scoring systems also having the highest values for $G_{BP}-G_{RP}$ *Gaia* color. This happens for the most part because of the relation between the temperature of the white dwarf and the $G_{BP}-G_{RP}$ *Gaia* color, considering that as the white dwarfs cools it becomes redder.

If the same “reduced” scorecard is used on the confirmed period-bouncers (Table 2-1), the lowest scoring system is once again V406 Vir with 72%, meaning that a category of high

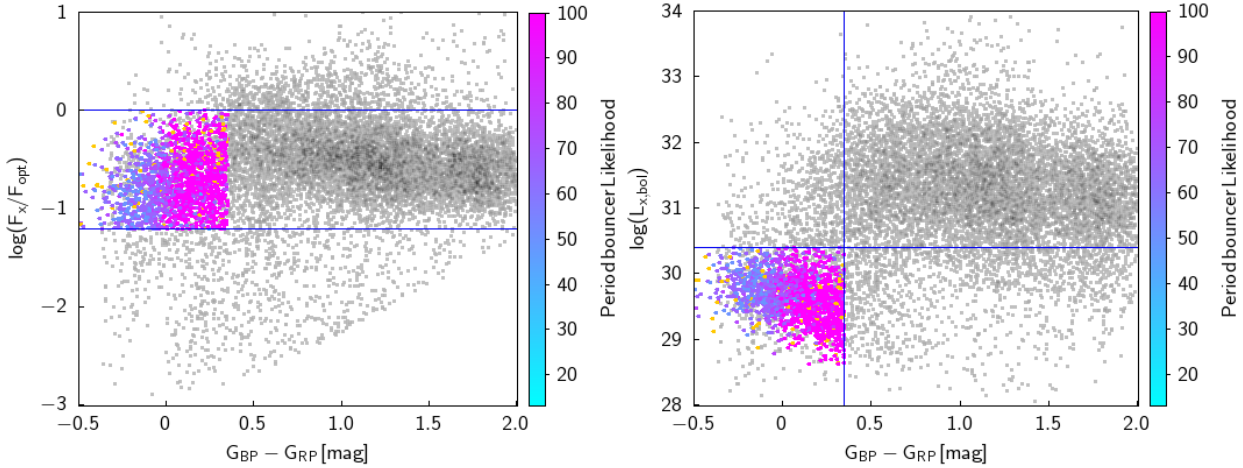


Figure 4-13.: X-ray selection cuts from Muñoz-Giraldo et al. (2024) applied to the population of eRASS:3 detected “high-fidelity” white dwarfs within 500pc. The final score of the X-ray selected period-bounce candidates is presented as a color scale. Candidates without enough information to have received a final score are presented in yellow. A population of cataclysmic variable candidates found in eRASS:3 is shown in grey as a reference (Schwope et al. in prep). **Left panel:** X-ray-to-optical flux ratio as a function of *Gaia* colors. **Right panel:** Bolometric X-ray luminosity as a function of *Gaia* colors.

likelihood of being a period-bouncer can be defined by systems that have final scores higher than 70 %. This category would include 1100 of the candidates in the catalog. However, it is relevant to mention that a significant number of these candidates, 764 systems, have a final score of 100 % likelihood of being a period-bouncer according to the “reduced” scorecard. These 764 period-bounce candidates are cool temperature, non-variable objects that look in optical bands like spectroscopically confirmed white dwarfs and in their X-ray, ultraviolet and infrared emissions like confirmed period-bouncers. Confirmation of these candidates as actual period-bouncers is very important as they might represent the missing population of period-bounce cataclysmic variables.

4.4. Outlook

At the moment, the work conducted has led to a confirmed population of period-bouncers that, in a 500pc volume-limited sample, corresponds to $\sim 11\%$ of the cataclysmic variable population, which is still quite far from the expected 40 % to 70 %. This can mean two things: the models describing the overall evolution of cataclysmic variables are incorrect and should be adjusted to reflect the small number of period-bouncers observed (see e.g. Schreiber et al. 2023), or a significant number of period-bouncers is waiting to be discovered as part of a large missing population.

The focus of this work has been towards the second approach and, considering the large number of surveys already conducted in optical, ultraviolet and infrared bands in the search of period-bouncers (Santisteban et al. 2018, Pala et al. 2022, Inight et al. 2023b), such X-ray studies might represent the last effort to find the large population of missing period-bouncers. The initial work on the catalog of X-ray selected period-bounce candidates is very promising, with 764 out of the 1662 members having a 100 % likelihood of being a period-bouncer according to the “reduced” scorecard (Fig. 4-14). In the ideal case where all these candidates are confirmed as actual period-bouncers, there would be a confirmation rate for X-ray selected period-bounce candidates of $\sim 50\%$. If the same ideal confirmation rate is applied to the population of X-ray selected cataclysmic variable candidates by Schwöpe et al. (prep), there would be the potential confirmation of ~ 1400 new cataclysmic variables within 500pc.

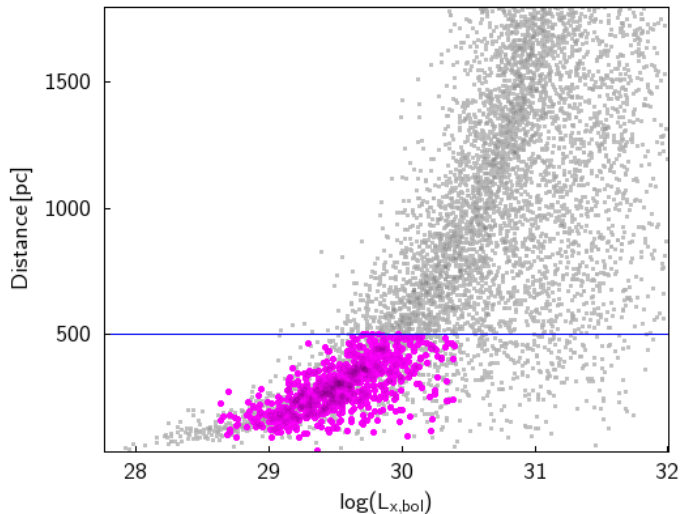


Figure 4-14.: Period-bounce candidates with 100 % likelihood of being period-bouncers. A population of eROSITA detected confirmed cataclysmic variables are shown as a reference (Schwöpe et al. prep).

Within this ideal population of cataclysmic variables, period-bouncers would make-up $\sim 55\%$ of the overall population, a result that is in agreement with the lower end of the predicted fraction of period-bouncers (Goliaš and Nelson 2015).

However, this is still an ideal population, and considerable work needs to be done in order to securely confirm that the population of missing period-bouncers has been found. Firstly, a spectroscopic confirmation of these objects as cataclysmic variables has to be carried out. This can be achieved using optical spectra, looking for Balmer emission lines from the accretion disc or column (Inight et al. 2023a), which is not present in single white dwarfs. The next step would be to establish these systems as short-period cataclysmic variables with late-type donors through gaining information on the orbital period of the system, which can come from a variety of different methods like light curve analysis from optical and X-ray surveys (Muñoz-Giraldo et al. 2024). Moreover, the donor should be characterized as this requires most likely a dedicated infrared campaign. Shedding light onto the system’s parameters would lead to a more detailed characterization of the system, and could represent the final confirmation that the X-ray selected candidates with 100 % likelihood of being period-

bouncers can be actually classified as period-bouncers, solving the long lasting discrepancy between the expected and observed population of period-bouncers.

Bibliography

- Abbott, T., Fleming, T., and Pasquini, L. (1997). The rosat cataclysmic variable rx j2353.0-3852. *Astronomy and Astrophysics*, v. 318, p. 134-139, 318:134–139.
- Agüeros, M. A., Anderson, S. F., Covey, K. R., Hawley, S. L., Margon, B., Newsom, E. R., Posselt, B., Silvestri, N. M., Szkody, P., and Voges, W. (2009). X-ray-emitting stars identified from the rosat all-sky survey and the sloan digital sky survey. *The Astrophysical Journal Supplement Series*, 181(2):444.
- Aizu, K. (1973). X-ray emission region of a white dwarf with accretion. *Progress of Theoretical Physics*, 49(4):1184–1194.
- Amantayeva, A., Zharikov, S., Page, K., Pavlenko, E., Sosnovskij, A., Khokhlov, S., and Ibraimov, M. (2021). Period bouncer cataclysmic variable ez lyn in quiescence. *The Astrophysical Journal*, 918(2):58.
- Andronov, N., Pinsonneault, M., and Sills, A. (2003). Cataclysmic variables: An empirical angular momentum loss prescription from open cluster data. *The Astrophysical Journal*, 582(1):358.
- Araujo-Betancor, S., Gänsicke, B., Hagen, H.-J., Marsh, T., Harlaftis, E., Thorstensen, J., Fried, R., Schmeer, P., and Engels, D. (2005). Hs 2331+ 3905: The cataclysmic variable that has it all. *Astronomy & Astrophysics*, 430(2):629–642.
- Audard, M., Osten, R., Brown, A., Briggs, K., Güdel, M., Hodges-Kluck, E., and Gizis, J. (2007). A chandra x-ray detection of the l dwarf binary kelu-1-simultaneous chandra and very large array observations. *Astronomy & Astrophysics*, 471(3):L63–L66.
- Bailer-Jones, C. A. L., Rybizki, J., Fouesneau, M., Demleitner, M., and Andrae, R. (2021). Estimating Distances from Parallaxes. V. Geometric and Photogeometric Distances to 1.47 Billion Stars in Gaia Early Data Release 3. *The Astronomical Journal*, 161(3):147.
- Balman, Ş., Khamitov, I., Kolbin, A., Çalışkan, E. A., Bikmaev, I., Özdönmez, A., Burenin, R., Kılıç, Y., Esenoğlu, H., Yelkenci, K., et al. (2024). Optical identification and follow-up observations of srga j213151. 5+ 491400-a new magnetic cataclysmic variable discovered with the srg observatory. *Astronomy & Astrophysics*, 684:A190.

- Bannikova, E. and Capaccioli, M. (2022). The three-body problem. In *Foundations of Celestial Mechanics*, pages 81–127. Springer.
- Barnes, S. A. and Kim, Y.-C. (2010). Angular momentum loss from cool stars: an empirical expression and connection to stellar activity. *The Astrophysical Journal*, 721(1):675.
- Belenkaya, E. S., Khodachenko, M. L., and Alexeev, I. I. (2015). Alfvén radius: a key parameter for astrophysical magnetospheres. *Characterizing stellar and exoplanetary environments*, pages 239–249.
- Belloni, D., Schreiber, M. R., Pala, A. F., Gänsicke, B. T., Zorotovic, M., and Rodrigues, C. V. (2020). Evidence for reduced magnetic braking in polars from binary population models. *Monthly Notices of the Royal Astronomical Society*, 491(4):5717–5731.
- Breedt, E., Gänsicke, B. T., Girven, J., Drake, A., Copperwheat, C., Parsons, S., and Marsh, T. (2012). The evolutionary state of short-period magnetic white dwarf binaries. *Monthly Notices of the Royal Astronomical Society*, 423(2):1437–1449.
- Brunner, H., Liu, T., Lamer, G., Georgakakis, A., Merloni, A., Brusa, M., Bulbul, E., Dennerl, K., Friedrich, S., Liu, A., et al. (2022). The erosita final equatorial depth survey (efeds)-x-ray catalogue. *Astronomy & Astrophysics*, 661:A1.
- Burleigh, M. R., Marsh, T., Gänsicke, B., Goad, M. R., Dhillon, V., Littlefair, S., Wells, M., Bannister, N., Hurkett, C., Martindale, A., et al. (2006). The nature of the close magnetic white dwarf+ probable brown dwarf binary sdss j121209. 31+ 013627.7. *Monthly Notices of the Royal Astronomical Society*, 373(4):1416–1422.
- Cannizzo, J. K., Smale, A. P., Wood, M. A., Still, M. D., and Howell, S. B. (2012). The kepler light curves of v1504 cygni and v344 lyrae: A study of the outburst properties. *The Astrophysical Journal*, 747(2):117.
- Cordova, F., Jensen, K., and Nugent, J. (1981a). The heao-1 soft x-ray survey of cataclysmic variable stars. *Monthly Notices of the Royal Astronomical Society*, 196(1):1–12.
- Cordova, F., Mason, K., and Nelson, J. (1981b). X-ray observations of selected cataclysmic variable stars using the einstein observatory. *Astrophysical Journal, Part 1, vol. 245, Apr. 15, 1981, p. 609-617. Research supported by the Miller Institute for Basic Research*., 245:609–617.
- Cropper, M. (1990). The polars. *Space Science Reviews*, 54(3):195–295.
- De Luca, A., Stelzer, B., Burgasser, A. J., Pizzocaro, D., Ranalli, P., Raetz, S., Marelli, M., Novara, G., Vignali, C., Belfiore, A., et al. (2020). Extras discovery of an x-ray superflare from an l dwarf. *Astronomy & Astrophysics*, 634:L13.

- Debes, J. H., López-Morales, M., Bonanos, A., and Weinberger, A. (2006). Detection of a variable infrared excess around sdss j121209. 31+ 013627.7. *The Astrophysical Journal*, 647(2):L147.
- Den Herder, J., Brinkman, A., Kahn, S., Branduardi-Raymont, G., Thomsen, K., Aarts, H., Audard, M., Bixler, J., den Boggende, A., Cottam, J., et al. (2001). The reflection grating spectrometer on board xmm-newton. *Astronomy & Astrophysics*, 365(1):L7–L17.
- Eggleton, P. P. (1983). Approximations to the radii of roche lobes. *Astrophysical Journal, Part 1 (ISSN 0004-637X)*, vol. 268, May 1, 1983, p. 368, 369., 268:368.
- Farihi, J., Burleigh, M., and Hoard, D. (2008). A near-infrared spectroscopic study of the accreting magnetic white dwarf sdss j121209. 31+ 013627.7 and its substellar companion. *The Astrophysical Journal*, 674(1):421.
- Galiullin, I., Rodriguez, A. C., Kulkarni, S. R., Sunyaev, R., Gilfanov, M., Bikmaev, I., Yungelson, L., van Roestel, J., Gänsicke, B. T., Khamitov, I., et al. (2024). A joint srg/erosita+ ztf search: Discovery of a 97-min period eclipsing cataclysmic variable with evidence of a brown dwarf secondary. *Monthly Notices of the Royal Astronomical Society*, 528(1):676–692.
- Gänsicke, B., Dillon, M., Southworth, J., Thorstensen, J., Rodríguez-Gil, P., Aungwerojwit, A., Marsh, T., Szkody, P., Barros, S., Casares, J., et al. (2009). Sdss unveils a population of intrinsically faint cataclysmic variables at the minimum orbital period. *Monthly Notices of the Royal Astronomical Society*, 397(4):2170–2188.
- Gentile Fusillo, N., Tremblay, P., Cukanovaite, E., Vorontseva, A., Lallement, R., Hollands, M., Gänsicke, B., Burdge, K., McCleery, J., and Jordan, S. (2021). A catalogue of white dwarfs in gaia edr3. *Monthly Notices of the Royal Astronomical Society*, 508(3):3877–3896.
- Giovannelli, F. (2008). Cataclysmic variables: A review. *Chinese Journal of Astronomy & Astrophysics Supplement*, Vol. 8, p. 237-258, 8:237–258.
- Goliash, J. and Nelson, L. (2015). Population synthesis of cataclysmic variables. i. inclusion of detailed nuclear evolution. *The Astrophysical Journal*, 809(1):80.
- Hakala, P., Parsons, S. G., Marsh, T. R., Gänsicke, B. T., Ramsay, G., Schwope, A., and Hermes, J. (2022). Circular polarimetry of suspect wind-accreting magnetic pre-polars. *Monthly Notices of the Royal Astronomical Society*, 513(3):3858–3870.
- Harrison, T. E. (2015). Direct detection of the l-dwarf donor in wz sagittae. *The Astrophysical Journal*, 816(1):4.

- Harrison, T. E., Bornak, J., Howell, S. B., Mason, E., Szkody, P., and McGurk, R. (2009). Infrared photometry and spectroscopy of vy aqr and ei psc: Two short-period cataclysmic variables with curious secondary stars. *The Astronomical Journal*, 137(4):4061.
- Hessman, F., Gänsicke, B., and Mattei, J. (2000). The history and source of mass-transfer variations in am herculis. *Astronomy & Astrophysics*, v. 361, p. 952-958 (2000), 361:952–958.
- Howell, S. B., Nelson, L. A., and Rappaport, S. (2001). An exploration of the paradigm for the 2-3 hour period gap in cataclysmic variables. *The Astrophysical Journal*, 550(2):897.
- Inight, K., Gänsicke, B. T., Breedt, E., Israel, H. T., Littlefair, S. P., Manser, C. J., Marsh, T. R., Mulvany, T., Pala, A. F., and Thorstensen, J. R. (2023a). A catalogue of cataclysmic variables from 20 yr of the Sloan Digital Sky Survey with new classifications, periods, trends, and oddities. *Monthly Notices of the Royal Astronomical Society*, 524(4):4867–4898.
- Inight, K., Gänsicke, B. T., Schwöpe, A., Anderson, S. F., Badenes, C., Breedt, E., Chandra, V., Davies, B. D. R., Gentile Fusillo, N. P., Green, M. J., Hermes, J. J., Huamani, I. A., Hwang, H., Knauff, K., Kurpas, J., Long, K. S., Malanushenko, V., Morrison, S., Quiroz C., I. J., Ramos, G. N. A., Roman-Lopes, A., Schreiber, M. R., Standke, A., Stutz, L., Thorstensen, J. R., Toloza, O., Tovmassian, G., and Zakamska, N. L. (2023b). Cataclysmic Variables from Sloan Digital Sky Survey - V. The search for period bouncers continues. *Monthly Notices of the Royal Astronomical Society*, 525(3):3597–3625.
- Irwin, J., Hodgkin, S., Aigrain, S., Hebb, L., Bouvier, J., Clarke, C., Moraux, E., and Brämich, D. (2007). The monitor project: rotation of low-mass stars in the open cluster ngc 2516. *Monthly Notices of the Royal Astronomical Society*, 377(2):741–758.
- Ishioka, R., Sekiguchi, K., and Maehara, H. (2007). Infrared spectroscopy of short-period cataclysmic variables. *Publications of the Astronomical Society of Japan*, 59(5):929–938.
- Isogai, K., Kato, T., Imada, A., Ohshima, T., Kojiguchi, N., Ohnishi, R., Hamsch, F.-J., Monard, B., Kiyota, S., Nishimura, H., et al. (2019). Third-nearest wz sge-type dwarf nova candidate asasn-14dx classified on the basis of gaia data release 2. *Publications of the Astronomical Society of Japan*, 71(1):22.
- Ivanova, N. and Taam, R. E. (2003). Magnetic braking revisited. *The Astrophysical Journal*, 599(1):516.
- Kafka, S. and Honeycutt, R. (2005). High/low states in magnetic cataclysmic variables. *The Astronomical Journal*, 130(2):742.

- Kato, T. (2015). Wz sge-type dwarf novae. *Publications of the Astronomical Society of Japan*, 67(6):108.
- Kato, T. (2022). Evolution of short-period cataclysmic variables: implications from eclipse modeling and stage a superhump method (with new year's gift). *arXiv preprint arXiv:2201.02945*.
- Kato, T., Hamsch, F.-J., Monard, B., Vanmunster, T., Maeda, Y., Miller, I., Itoh, H., Kiyota, S., Isogai, K., Kimura, M., et al. (2016). Survey of period variations of superhumps in su uma-type dwarf novae. viii. the eighth year (2015–2016). *Publications of the Astronomical Society of Japan*, 68(4):65.
- Kato, T., Imada, A., Uemura, M., Nogami, D., Maehara, H., Ishioka, R., Baba, H., Matsu-moto, K., Iwamatsu, H., Kubota, K., et al. (2009). Survey of period variations of superhumps in su uma-type dwarf novae. *Publications of the Astronomical Society of Japan*, 61(sp2):S395–S616.
- Kato, T. and Osaki, Y. (2013). New method of estimating binary's mass ratios by using superhumps. *Publications of the Astronomical Society of Japan*, 65(6):115–115.
- Kawaler, S. D. (1988). Angular momentum loss in low-mass stars. *Astrophysical Journal, Part 1 (ISSN 0004-637X)*, vol. 333, Oct. 1, 1988, p. 236-247., 333:236–247.
- Kawka, A., Vennes, S., Ferrario, L., Bessell, M., Keller, S., Paunzen, E., Buckley, D., Groenewald, D., Janík, J., and Zejda, M. (2021). The magnetic system smss j1606- 1000 as a period bouncer. *Monthly Notices of the Royal Astronomical Society: Letters*, 507(1):L30–L35.
- Kimura, M., Isogai, K., Kato, T., Taguchi, K., Wakamatsu, Y., Hamsch, F.-J., Monard, B., Myers, G., Dvorak, S., Starr, P., et al. (2018). Asassn-16dt and asassn-16hg: Promising candidate period bouncers. *Publications of the Astronomical Society of Japan*, 70(3):47.
- King, A. (1988). The evolution of compact binaries. *Quarterly Journal of the Royal Astronomical Society*, 29:1–25.
- Knigge, C. (2006). The donor stars of cataclysmic variables. *Monthly Notices of the Royal Astronomical Society*, 373(2):484–502.
- Knigge, C., Baraffe, I., and Patterson, J. (2011). The evolution of cataclysmic variables as revealed by their donor stars. *The Astrophysical Journal Supplement Series*, 194(2):28.
- Kochukhov, O. (2021). Magnetic fields of m dwarfs. *The Astronomy and Astrophysics Review*, 29(1):1.

- Koester, D. (2010). White dwarf spectra and atmosphere models. *Memorie della Societa Astronomica Italiana*, 81:921–931.
- Kolb, U. (1993). A model for the intrinsic population of cataclysmic variables. *Astronomy & Astrophysics*, Vol. 271, p. 149 (1993), 271:149.
- Kolb, U. and Baraffe, I. (1999). Brown dwarfs and the cataclysmic variable period minimum. *Monthly Notices of the Royal Astronomical Society*, 309(4):1034–1042.
- Külebi, B., Jordan, S., Euchner, F., Gänsicke, B., and Hirsch, H. (2009). Analysis of hydrogen-rich magnetic white dwarfs detected in the sloan digital sky survey. *Astronomy & Astrophysics*, 506(3):1341–1350.
- Lamb, D. and Masters, A. (1979). X and uv radiation from accreting magnetic degenerate dwarfs. *Astrophysical Journal, Part 2-Letters to the Editor*, vol. 234, Dec. 1, 1979, p. L117-L122., 234:L117–L122.
- Littlefair, S., Dhillon, V., Marsh, T., Gänsicke, B., Southworth, J., Baraffe, I., Watson, C., and Copperwheat, C. (2008). On the evolutionary status of short-period cataclysmic variables. *Monthly Notices of the Royal Astronomical Society*, 388(4):1582–1594.
- Littlefair, S., Dhillon, V., and Martin, E. (2003). On the evidence for brown dwarf secondary stars in cataclysmic variables. *Monthly Notices of the Royal Astronomical Society*, 340(1):264–268.
- Littlefield, C., Hoard, D., Garnavich, P., Szkody, P., Mason, P. A., Scaringi, S., Ilkiewicz, K., Kennedy, M. R., Rappaport, S. A., and Jayaraman, R. (2023). Kepler k2 and tess observations of two magnetic cataclysmic variables: The new asynchronous polar sdss j084617. 11+ 245344.1 and paloma. *The Astronomical Journal*, 165(2):43.
- Liu, T., Buchner, J., Nandra, K., Merloni, A., Dwelly, T., Sanders, J. S., Salvato, M., Arcodia, R., Brusa, M., Wolf, J., et al. (2022a). The erosita final equatorial-depth survey (efeds)-the agn catalog and its x-ray spectral properties. *Astronomy & Astrophysics*, 661:A5.
- Liu, T., Merloni, A., Comparat, J., Nandra, K., Sanders, J., Lamer, G., Buchner, J., Dwelly, T., Freyberg, M., Malyali, A., et al. (2022b). Establishing the x-ray source detection strategy for erosita with simulations. *Astronomy & Astrophysics*, 661:A27.
- Livio, M. and Pringle, J. (1994). Star spots and the period gap in cataclysmic variables. *Astrophysical Journal, Part 1 (ISSN 0004-637X)*, vol. 427, no. 2, p. 956-960, 427:956–960.
- Marsh, T. and Horne, K. (1988). Images of accretion discs—ii. doppler tomography. *Monthly Notices of the Royal Astronomical Society*, 235(1):269–286.

- Mason, K., Breeveld, A., Much, R., Carter, M., Cordova, F., Cropper, M., Fordham, J., Huckle, H., Ho, C., Kawakami, H., et al. (2001). The xmm-newton optical/uv monitor telescope. *Astronomy & Astrophysics*, 365(1):L36–L44.
- McAllister, M., Littlefair, S., Dhillon, V., Marsh, T., Gänsicke, B., Bochinski, J., Bours, M., Breedt, E., Hardy, L., Hermes, J., et al. (2017). Sdss j105754. 25+ 275947.5: a period-bounce eclipsing cataclysmic variable with the lowest-mass donor yet measured. *Monthly Notices of the Royal Astronomical Society*, 467(1):1024–1032.
- Merloni, A., Lamer, G., Liu, T., Ramos-Ceja, M., Brunner, H., Bulbul, E., Dennerl, K., Doroshenko, V., Freyberg, M., Friedrich, S., et al. (2024). The srg/erosita all-sky survey-first x-ray catalogues and data release of the western galactic hemisphere. *Astronomy & Astrophysics*, 682:A34.
- Mestel, L. (1968). Magnetic braking by a stellar wind-i. *Monthly Notices of the Royal Astronomical Society*, Vol. 138, p. 359, 138:359.
- Mestel, L. and Spruit, H. (1987). On magnetic braking of late-type stars. *Monthly Notices of the Royal Astronomical Society*, 226(1):57–66.
- Meyer, F. and Meyer-Hofmeister, E. (1984). Outbursts in dwarf novae accretion disks. *Astronomy & Astrophysics*, 132:143–150.
- Morin, J., Donati, J.-F., Petit, P., Delfosse, X., Forveille, T., Albert, L., Aurière, M., Cabanac, R., Dintrans, B., Fares, R., et al. (2008). Large-scale magnetic topologies of mid m dwarfs. *Monthly Notices of the Royal Astronomical Society*, 390(2):567–581.
- Morin, J., Donati, J.-F., Petit, P., Delfosse, X., Forveille, T., and Jardine, M. M. (2010). Large-scale magnetic topologies of late m dwarfs. *Monthly Notices of the Royal Astronomical Society*, 407(4):2269–2286.
- Muñoz-Giraldo, D., Stelzer, B., de Martino, D., and Schwope, A. (2023). New X-ray detections of magnetic period-bounce cataclysmic variables from XMM-Newton and SRG/eROSITA. *Astronomy & Astrophysics*, 676:A7.
- Muñoz-Giraldo, D., Stelzer, B., and Schwope, A. (2024). Cataclysmic variables around the period-bounce: An eROSITA-enhanced multiwavelength catalog. *Astronomy & Astrophysics*, 687:A305.
- Mukadam, A. S., Townsley, D., Szkody, P., Gänsicke, B., Southworth, J., Brockett, T., Parsons, S., Hermes, J., Montgomery, M., Winget, D., et al. (2013). Enigmatic recurrent pulsational variability of the accreting white dwarf eq lyn (sdss j074531. 92+ 453829.6). *The Astronomical Journal*, 146(3):54.

- Mukai, K. (2003). X-ray spectroscopy of cataclysmic variables. *Advances in Space Research*, 32(10):2067–2076.
- Mukai, K. (2017). X-ray emissions from accreting white dwarfs: a review. *Publications of the Astronomical Society of the Pacific*, 129(976):062001.
- Muno, M. P., Bauer, F. E., Bandyopadhyay, R., and Wang, Q. (2006). A chandra catalog of x-ray sources in the central 150 pc of the galaxy. *The Astrophysical Journal Supplement Series*, 165(1):173.
- Myers, G., Patterson, J., de Miguel, E., Hamsch, F.-J., Monard, B., Bolt, G., McCormick, J., Rea, R., and Allen, W. (2017). Resynchronization of the asynchronous polar cd ind. *Publications of the Astronomical Society of the Pacific*, 129(974):044204.
- Nagae, T., Oka, K., Matsuda, T., Fujiwara, H., Hachisu, I., and Boffin, H. M. (2004). Wind accretion in binary stars-i. mass accretion ratio. *Astronomy & Astrophysics*, 419(1):335–343.
- Nakata, C., Kato, T., Nogami, D., Pavlenko, E. P., Ohshima, T., De Miguel, E., Stein, W., Siokawa, K., Morelle, E., Itoh, H., et al. (2014). Ot j075418. 7+ 381225 and ot j230425. 8+ 062546: Promising candidates for the period bouncer. *Publications of the Astronomical Society of Japan*, 66(6):116.
- Nauenberg, M. (1972). Analytic approximations to the mass-radius relation and energy of zero-temperature stars. *The Astrophysical Journal*, 175:417.
- Neustroev, V., Marsh, T. R., Zharikov, S., Knigge, C., Kuulkers, E., Osborne, J. P., Page, K., Steeghs, D., Suleimanov, V. F., Tovmassian, G., et al. (2017). The remarkable outburst of the highly evolved post-period-minimum dwarf nova sss j122221. 7- 311525. *Monthly Notices of the Royal Astronomical Society*, 467(1):597–618.
- Neustroev, V. V. and Mäntynen, I. (2023). A brown dwarf donor and an optically thin accretion disc with a complex stream impact region in the period-bouncer candidate BW Sculptoris. *Monthly Notices of the Royal Astronomical Society*, 523(4):6114–6137.
- Norton, A. (1993). Simulation of the x-ray light curves of intermediate polars. *Monthly Notices of the Royal Astronomical Society*, 265(2):316–328.
- Nucita, A., Kuulkers, E., De Paolis, F., Mukai, K., Ingrassio, G., and Maiolo, B. (2014). Xmm-newton and swift observations of wz sagittae: spectral and timing analysis. *Astronomy & Astrophysics*, 566:A121.
- Ok, S. and Schwobe, A. (2022). Xmm-newton and tess observations of the highly variable polar v496 uma. *Astronomy & Astrophysics*, 662:A116.

- Osaki, Y. (1989). A model for the superoutburst phenomenon of *su ursae majoris* stars. *Astronomical Society of Japan, Publications (ISSN 0004-6264)*, vol. 41, no. 5, 1989, p. 1005-1033., 41:1005–1033.
- Osborne, J. (1987). X-ray observations of cataclysmic variables. In *International Astronomical Union Colloquium*, volume 93, pages 207–223. Cambridge University Press.
- Otulakowska-Hypka, M., Olech, A., and Patterson, J. (2016). Statistical analysis of properties of dwarf novae outbursts. *Monthly Notices of the Royal Astronomical Society*, 460(3):2526–2541.
- Paczynski, B. (1976). Common envelope binaries. In *Symposium-International Astronomical Union*, volume 73, pages 75–80. Cambridge University Press.
- Paczynski, B. and Sienkiewicz, R. (1983). The minimum period and the gap in periods of cataclysmic binaries. *Astrophysical Journal, Part 1 (ISSN 0004-637X)*, vol. 268, May 15, 1983, p. 825-831., 268:825–831.
- Pala, A., Gänsicke, B., Belloni, D., Parsons, S., Marsh, T., Schreiber, M., Breedt, E., Knigge, C., Sion, E., Szkody, P., et al. (2022). Constraining the evolution of cataclysmic variables via the masses and accretion rates of their underlying white dwarfs. *Monthly Notices of the Royal Astronomical Society*, 510(4):6110–6132.
- Pala, A., Gänsicke, B., Breedt, E., Knigge, C., Hermes, J., Gentile Fusillo, N., Hollands, M., Naylor, T., Pelisoli, I., Schreiber, M., et al. (2020). A volume-limited sample of cataclysmic variables from *gaia dr2*: space density and population properties. *Monthly Notices of the Royal Astronomical Society*, 494(3):3799–3827.
- Pala, A. F., Gänsicke, B. T., Marsh, T., Breedt, E., Hermes, J. J., Landstreet, J., Schreiber, M., Townsley, D., Wang, L., Aungwerojwit, A., et al. (2019). Evidence for mass accretion driven by spiral shocks onto the white dwarf in *sds j123813.73–033933.0*. *Monthly Notices of the Royal Astronomical Society*, 483(1):1080–1103.
- Pala, A. F., Schmidtbreick, L., Tappert, C., Gänsicke, B. T., and Mehner, A. (2018). The cataclysmic variable *qz lib*: a period bouncer. *Monthly Notices of the Royal Astronomical Society*, 481(2):2523–2535.
- Patterson, J. (1998). Late evolution of cataclysmic variables. *Publications of the Astronomical Society of the Pacific*, 110(752):1132.
- Patterson, J. (2011). Distances and absolute magnitudes of dwarf novae: murmurs of period bounce. *Monthly Notices of the Royal Astronomical Society*, 411(4):2695–2716.

- Patterson, J., Kemp, J., Harvey, D. A., Fried, R. E., Rea, R., Monard, B., Cook, L. M., Skillman, D. R., Vanmunster, T., Bolt, G., et al. (2005a). Superhumps in cataclysmic binaries. xv. q crit, $i_{\frac{1}{2}}i_{\frac{1}{2}}(q)$, and mass-radius. *Publications of the Astronomical Society of the Pacific*, 117(837):1204.
- Patterson, J., Masi, G., Richmond, M. W., Martin, B., Beshore, E., Skillman, D. R., Kemp, J., Vanmunster, T., Rea, R., Allen, W., et al. (2002). The 2001 superoutburst of wz sagittae. *Publications of the Astronomical Society of the Pacific*, 114(797):721.
- Patterson, J. and Raymond, J. (1985). X-ray emission from cataclysmic variables with accretion disks. i-hard x-rays. ii-euv/soft x-ray radiation. *Astrophysical Journal, Part 1 (ISSN 0004-637X)*, vol. 292, May 15, 1985, p. 535-558., 292:535–558.
- Patterson, J., Richman, H., Kemp, J., and Mukai, K. (1998). Rapid oscillations in cataclysmic variables. xiii. wz sagittae revisited. *Publications of the Astronomical Society of the Pacific*, 110(746):403.
- Patterson, J., Thorstensen, J. R., and Kemp, J. (2005b). Pulsations, boundary layers, and period bounce in the cataclysmic variable re j1255+ 266. *Publications of the Astronomical Society of the Pacific*, 117(831):427.
- Politano, M. and Weiler, K. P. (2006). The distribution of secondary masses in post-common-envelope binaries: A potential test of disrupted magnetic braking. *The Astrophysical Journal*, 641(2):L137.
- Potter, S. B. (1998). *A multiwavelength study of the accretion region in magnetic cataclysmic variables*. University of London, University College London (United Kingdom).
- Predehl, P., Andritschke, R., Arefiev, V., Babyshkin, V., Batanov, O., Becker, W., Böhringer, H., Bogomolov, A., Boller, T., Borm, K., et al. (2021). The erosita x-ray telescope on srg. *Astronomy & Astrophysics*, 647:A1.
- Pretorius, M. L., Knigge, C., and Schwobe, A. D. (2013). The space density of magnetic cataclysmic variables. *Monthly Notices of the Royal Astronomical Society*, 432(1):570–583.
- Rajpurohit, A., Allard, F., Rajpurohit, S., Sharma, R., Teixeira, G., Mousis, O., and Kamlesh, R. (2018). Exploring the stellar properties of m dwarfs with high-resolution spectroscopy from the optical to the near-infrared. *Astronomy & Astrophysics*, 620:A180.
- Rappaport, S., Cash, W., Doxsey, R., McClintock, J., and Moore, G. (1974). Possible detection of very soft x-rays from ss cygni. *Astrophysical Journal*, vol. 187, p. L5, 187:L5.
- Rappaport, S., Joss, P., and Webbink, R. (1982). The evolution of highly compact binary stellar systems. *Astrophysical Journal, Part 1*, vol. 254, Mar. 15, 1982, p. 616-640., 254:616–640.

- Rappaport, S., Verbunt, F., and Joss, P. C. (1983). A new technique for calculations of binary stellar evolution, with application to magnetic braking. *Astrophysical Journal, Part 1 (ISSN 0004-637X)*, vol. 275, Dec. 15, 1983, p. 713-731. Sponsorship: Nederlandse organisatie voor Zuiver-Wetenschappelijk, Onderzoek., 275:713–731.
- Ritter, H. (1991). Recent progress in understanding the secular evolution of cataclysmic binaries. In *High Energy Astrophysics: Compact Stars and Active Galaxies (Proc. 3rd Chinese Academy of Sciences and Max-Planck-Society Workshop, Huangshan, China, 1990)*, Ed. QB Li. World Scientific, Singapore, pages 107–116. World Scientific.
- Ritter, H. and Kolb, U. (2003). Catalogue of cataclysmic binaries, low-mass x-ray binaries and related objects. *Astronomy & Astrophysics*, 404(1):301–303.
- Rodriguez, A. C., Kulkarni, S. R., Prince, T. A., Szkody, P., Burdge, K. B., Caiazzo, I., van Roestel, J., Vanderbosch, Z. P., El-Badry, K., Bellm, E. C., et al. (2023). Discovery of two polars from a crossmatch of ztf and the srg/efeds x-ray catalog. *The Astrophysical Journal*, 945(2):141.
- Rothschild, R., Gruber, D., Knight, F., Matteson, J., Nolan, P., Swank, J., Holt, S., Serlemitsos, P., Mason, K., and Tuohy, I. (1981). The x-ray spectrum of am herculis from 0.1 to 150 keV. *Astrophysical Journal, Part 1*, vol. 250, Nov. 15, 1981, p. 723-732., 250:723–732.
- Santisteban, J. H., Knigge, C., Pretorius, M., Sullivan, M., and Warner, B. (2018). The space density of post-period minimum cataclysmic variables. *Monthly Notices of the Royal Astronomical Society*, 473(3):3241–3250.
- Santisteban, J. V. H., Knigge, C., Littlefair, S. P., Breton, R. P., Dhillon, V. S., Gänsicke, B. T., Marsh, T. R., Pretorius, M. L., Southworth, J., and Hauschildt, P. H. (2016). An irradiated brown-dwarf companion to an accreting white dwarf. *Nature*, 533(7603):366–368.
- Sarkar, A., Rodriguez, A. C., Ginzburg, S., Yungelson, L., and Tout, C. A. (2024). Weakening of magnetic braking in cataclysmic variables explains the dearth of period bouncers. *arXiv preprint arXiv:2401.14389*.
- Savourey, C., Littlefair, S. P., Marsh, T. R., Dhillon, V. S., Parsons, S., Copperwheat, C., and Steeghs, D. (2012). A radial velocity study of ctcv j1300- 3052. *Monthly Notices of the Royal Astronomical Society*, 422(1):469–477.
- Schmidt, G. D., Szkody, P., Silvestri, N. M., Cushing, M. C., Liebert, J., and Smith, P. S. (2005). Discovery of a magnetic white dwarf/probable brown dwarf short-period binary. *The Astrophysical Journal*, 630(2):L173.

- Schreiber, M., Zorotovic, M., and Wijnen, T. (2016). Three in one go: consequential angular momentum loss can solve major problems of cv evolution. *Monthly Notices of the Royal Astronomical Society*, 455(1):L16–L20.
- Schreiber, M. R., Belloni, D., and van Roestel, J. (2023). Period bouncers as detached magnetic cataclysmic variables. *Astronomy & Astrophysics*, 679:L8.
- Schwope, A. and Christensen, L. (2010). X-shooting of eridani: further evidence for a massive white dwarf and a sub-stellar secondary. *Astronomy & Astrophysics*, 514:A89.
- Schwope, A., Knauff, K., Kurpas, J., Stelzer, B., Stutz, L., and Tubín-Arenas (prep). A first systematic characterization of cataclysmic variables in srg/erosita surveys.
- Schwope, A., Kurpas, J., Baecke, P., Knauff, K., Stütz, L., Tubín-Arenas, D., Standke, A., Anderson, S., Bauer, F., Brandt, W., et al. (2024). Compact white dwarf binaries in the combined srg/erosita/sdss efeds survey. *Astronomy & Astrophysics*, 686:A110.
- Schwope, A., Worpel, H., and Traulsen, I. (2021). X-ray and ultraviolet observations of the eclipsing cataclysmic variables ov bootis and sdss j103533. 02+ 055158.3 with degenerate donors. *Astronomy & Astrophysics*, 646:A181.
- Schwope, A. D., Burnner, H., Hambaryan, V., and Schwarz, R. (2002). *Astronomical Society of the Pacific Conference Series, Vol. 261, The Physics of Cataclysmic Variables and Related Objects*, ed. Gänsicke, B. T. and Beuermann, K. and Reinsch, K., 102.
- Shakura, N., Postnov, K., Kochetkova, A. Y., and Hjalmarsdotter, L. (2014). Theory of wind accretion. In *EPJ Web of Conferences*, volume 64, page 02001. EDP Sciences.
- Shakura, N. I. and Sunyaev, R. A. (1973). Black holes in binary systems. observational appearance. *Astronomy and Astrophysics, Vol. 24, p. 337-355*, 24:337–355.
- Shugarov, S. Y. and Malashevich, S. (2021). New cataclysmic variable in pisces: A wz sge-subtype star with rebrightenings. *Peremennye Zvezdy*, 41(6):27–38.
- Southworth, J., Gänsicke, B., Marsh, T., De Martino, D., Hakala, P., Littlefair, S., Rodríguez-Gil, P., and Szkody, P. (2006). Vlt/fors spectroscopy of faint cataclysmic variables discovered by the sloan digital sky survey. *Monthly Notices of the Royal Astronomical Society*, 373(2):687–699.
- Steele, P., Burleigh, M., Dobbie, P., Jameson, R., Barstow, M., and Satterthwaite, R. (2011). White dwarfs in the ukirt infrared deep sky survey large area survey: the substellar companion fraction. *Monthly Notices of the Royal Astronomical Society*, 416(4):2768–2791.

- Stelzer, B., de Martino, D., Casewell, S., Wynn, G., and Roy, M. (2017). X-ray orbital modulation of a white dwarf accreting from an l dwarf-the system sdss j121209. 31+013627.7. *Astronomy & Astrophysics*, 598:L6.
- Strüder, L., Briel, U., Dennerl, K., Hartmann, R., Kendziorra, E., Meidinger, N., Pfeffermann, E., Reppin, C., Aschenbach, B., Bornemann, W., et al. (2001). The european photon imaging camera on xmm-newton: the pn-ccd camera. *Astronomy & Astrophysics*, 365(1):L18–L26.
- Sunyaev, R., Arefiev, V., Babyshkin, V., Bogomolov, A., Borisov, K., Buntov, M., Brunner, H., Burenin, R., Churazov, E., Coutinho, D., et al. (2021). Srg x-ray orbital observatory-its telescopes and first scientific results. *Astronomy & Astrophysics*, 656:A132.
- Szkody, P., Godon, P., Gänsicke, B. T., Kafka, S., Castillo, O. F., Bell, K. J., Cho, P., Sion, E. M., Kumar, P., Townsley, D. M., et al. (2021). The heating and pulsations of v386 serpentis after its 2019 dwarf nova outburst. *The Astrophysical Journal*, 914(1):40.
- Temmink, K., Pols, O., Justham, S., Istrate, A., and Toonen, S. (2023). Coping with loss-stability of mass transfer from post-main-sequence donor stars. *Astronomy & Astrophysics*, 669:A45.
- Thorstensen, J. R. (2020). Spectroscopic studies of 30 short-period cataclysmic variable stars and remarks on the evolution and population of similar objects. *The Astronomical Journal*, 160(1):6.
- Thorstensen, J. R., Taylor, C. J., Peters, C. S., Skinner, J. N., Southworth, J., and Gänsicke, B. T. (2015). Spectroscopic orbital periods for 29 cataclysmic variables from the sloan digital sky survey. *The Astronomical Journal*, 149(4):128.
- Townsley, D. M. and Gänsicke, B. T. (2009). Cataclysmic variable primary effective temperatures: constraints on binary angular momentum loss. *The Astrophysical Journal*, 693(1):1007.
- Turner, D., Giles, P., Romer, A., Wilkinson, R., Upsdell, E., Klein, M., Viana, P., Hilton, M., Bhargava, S., Collins, C., et al. (2022). The xmm cluster survey: an independent demonstration of the fidelity of the efeds galaxy cluster data products and implications for future studies. *Monthly Notices of the Royal Astronomical Society*, 517(1):657–674.
- Turner, M. J., Abbey, A., Arnaud, M., Balasini, M., Barbera, M., Belsole, E., Bennie, P., Bernard, J., Bignami, G., Boer, M., et al. (2001). The european photon imaging camera on xmm-newton: the mos cameras. *Astronomy & Astrophysics*, 365(1):L27–L35.
- Ulla, A., Giovannelli, F., and Martinez-Pais, I. (1999). Multifrequency observations of non-magnetic cataclysmic variables. *Memorie della Societa Astronomica Italiana, Vol. 70, N. 3-4, p. 971-986*, 70:971–986.

- Unda-Sanzana, E., Marsh, T., Gänsicke, B. T., Maxted, P., Morales-Rueda, L., Dhillon, V., Thoroughgood, T., Tremou, E., Watson, C., and Hinojosa-Goni, R. (2008). Gd 552: a cataclysmic variable with a brown dwarf companion? *Monthly Notices of the Royal Astronomical Society*, 388(2):889–897.
- Uthas, H., Patterson, J., Kemp, J., Knigge, C., Monard, B., Rea, R., Bolt, G., McCormick, J., Christie, G., Retter, A., et al. (2012). Two new accreting, pulsating white dwarfs: Sdss j1457+ 51 and bw sculptoris. *Monthly Notices of the Royal Astronomical Society*, 420(1):379–387.
- Vanlandingham, K. M., Schmidt, G. D., Eisenstein, D. J., Harris, H. C., Anderson, S. F., Hall, P. B., Liebert, J., Schneider, D. P., Silvestri, N. M., Stinson, G. S., et al. (2005). Magnetic white dwarfs from the sdss. ii. the second and third data releases. *The Astronomical Journal*, 130(2):734.
- Verbunt, F., Bunk, W., Ritter, H., and Pfeffermann, E. (1997). Cataclysmic variables in the rosat pspc all sky survey. *Astronomy & Astrophysics*, v. 327, p. 602-613, 327:602–613.
- Verbunt, F. and Zwaan, C. (1981). Magnetic braking in low-mass x-ray binaries. *Astronomy & Astrophysics*, 100:L7–L9.
- Warner, B. (1995). *Cataclysmic variable stars*, volume 28. Cambridge University Press.
- Whitehurst, R. (1988). Numerical simulations of accretion discs–i. superhumps: a tidal phenomenon of accretion discs. *Monthly Notices of the Royal Astronomical Society*, 232(1):35–51.
- Wickramasinghe, D. and Ferrario, L. (2000). Magnetism in isolated and binary white dwarfs. *Publications of the Astronomical Society of the Pacific*, 112(773):873.
- Wood, B. E., Linsky, J. L., and Güdel, M. (2015). Stellar winds in time. *Characterizing Stellar and Exoplanetary Environments*, pages 19–35.
- Woudt, P. A. and Warner, B. (2004). Sdss j161033. 64–010223.3: a second cataclysmic variable with a non-radially pulsating primary. *Monthly Notices of the Royal Astronomical Society*, 348(2):599–602.
- Zharikov, S., Tovmassian, G., Aviles, A., Michel, R., Gonzalez-Buitrago, D., and García-Díaz, M. T. (2013). The accretion disk in the post period-minimum cataclysmic variable sdss j080434. 20+ 510349.2. *Astronomy & Astrophysics*, 549:A77.

**A. New Systems in the Catalog of
Known Cataclysmic Variables
Around the Period-Bounce**

Table **A-1** presents the system parameters for the 21 new systems that have been added since its publication to the catalog of known cataclysmic variables around the period-bounce presented by Muñoz-Giraldo et al. (2024).

Table A-1.: System parameters for the period-bounce candidates not included in Muñoz-Giraldo et al. (2024) with distances from Bailer-Jones et al. (2021).

System	P_{orb} [h]	M_{donor} [M_{\odot}]	SpT	Distance [pc]	WD T_{eff} [K]	M_{WD} [M_{\odot}]	WD type	References
ASASSN -14dx	1.38	-	-	81	9113	-	nMag	1, 2
OT J2138+2619	1.31	0.068	-	99	15317	0.57	-	3, 4
SDSS J0929+0053	1.85	-	M5	-	-	-	-	5
SDSS J0058-0107	1.56	0.063	-	-	-	-	-	6
EQ Lyn	1.33	-	-	314	15447	0.75	nMag	7, 4
SDSS J0755+1435	1.41	-	-	240	16193	0.91	nMag	4
FV Lyn	1.67	-	-	335	9788	-	-	8, 2
LV Cnc	1.35	-	-	196	9730	-	nMag	9, 2
1RXS J1014+0638	1.42	-	-	192	10027	-	-	8, 2
SDSS J1457+5148	1.30	-	-	587	9672	-	nMag	10, 2
V386 Ser	1.34	-	-	244	9846	0.68	nMag	11, 12, 2
QZ Aqr	1.67	0.076	-	-	-	-	-	8, 13
SDSS J2141+0507	1.31	-	-	274	11679	-	nMag	8, 2
OT J2311+0130	1.24	0.048	-	-	-	-	-	14
VY Aqr	1.51	0.070	M6	141	14453	1.06	nMag	15, 4
ZTF19acfixfe	1.43	-	-	-	-	-	Mag	16
GALEX J0411+6853	1.62	0.017	T3	324	13790	0.84	Mag	17
eFEDS J0926+0105	1.47	-	-	385	-	-	Mag	18
2QZ J1428+0031	-	-	-	352	10662	-	-	2
GALEX J1811+7956	-	-	-	364	8262	-	-	2
ATO J026.6+49.2	2.06	-	T2	57	8550	-	Mag	19

White dwarf type: Magnetic (Mag) or non-magnetic (nMag).

References. (1) Isogai et al. (2019), (2) Gentile Fusillo et al. (2021), (3) Kato (2015), (4) Pala et al. (2022), (5) Schwöpe et al. (2024), (6) Kato (2022), (7) Mukadam et al. (2013), (8) Inight et al. (2023b), (9) Thorstensen et al. (2015), (10) Uthas et al. (2012), (11) Woudt and Warner (2004), (12) Szkody et al. (2021), (13) Otulakowska-Hypka et al. (2016), (14) Shugarov and Malashevich (2021), (15) Harrison et al. (2009), (16) Balman et al. (2024), (17) Galiullin et al. (2024), (18) Rodriguez et al. (2023), (19) Hakala et al. (2022).

B. Published Papers

New X-ray detections of magnetic period-bounce cataclysmic variables from *XMM-Newton* and SRG/eROSITA

Daniela Muñoz-Giraldo¹, Beate Stelzer^{1,2}, Domitilla de Martino³, and Axel Schwope⁴

¹ Institut für Astronomie und Astrophysik, Eberhard-Karls Universität Tübingen, Sand 1, 72076 Tübingen, Germany
e-mail: munoz-giraldo@astro.uni-tuebingen.de

² INAF – Osservatorio Astronomico di Palermo, Piazza del Parlamento 1, 90134 Palermo, Italy

³ INAF – Osservatorio Astronomico di Capodimonte, Via Moiariello 16, 80131 Naples, Italy

⁴ Leibniz-Institut für Astrophysik Potsdam (AIP), An der Sternwarte 16, 14482 Potsdam, Germany

Received 13 March 2023 / Accepted 7 June 2023

ABSTRACT

Context. A great portion of the cataclysmic variable population, between 40% and 70%, is predicted to be made up of period-bouncers, systems with degenerate donors that have evolved past the period minimum. However, due to their intrinsic faintness, only a few of these systems have been observed and confidently identified so far.

Aims. We have searched for X-ray emission as proof of accretion in order to confirm period-bounce cataclysmic variables.

Methods. In this study, we used data from *XMM-Newton* and eROSITA on a pilot sample of three period-bounce candidates with a magnetic white dwarf, which are expected to exhibit stronger X-ray emission than non-magnetic systems due to more efficient conversion of matter accretion onto the white dwarf.

Results. In a dedicated *XMM-Newton* observation of the period-bounce candidate SDSS J151415.65+074446.5 we discovered X-ray modulation at the binary orbital period confirming it as an accreting system. The X-ray light curve and the X-ray spectrum display characteristics of magnetic Polar-type systems, allowing us for the first time to determine the X-ray luminosity and mass accretion rate for this system. Catalog data from eROSITA on the Spektrum-Roentgen-Gamma satellite for V379 Vir and SDSS J125044.42+154957.4 enabled a first look into the X-ray behavior of period-bounce candidates with this new all-sky instrument. From the eROSITA measurements, the X-ray luminosity and mass accretion rate were determined for the first time for SDSS J125044.42+154957.4, and the earlier result for V379 Vir from *XMM-Newton* was confirmed.

Conclusions. The three cataclysmic variables with a magnetic white dwarf and very low-mass donor studied in this work present evidence for X-ray emission at a similar level of $L_X [\text{erg s}^{-1}] \approx 10^{29}$, which, together with the detection of X-ray orbital modulation in two of them (i.e., V379 Vir and SDSS J151415.65+074446.5), unambiguously proves the presence of accretion in these systems. The detection of these period-bouncers at faint X-ray luminosity levels with the all-sky X-ray survey eROSITA offers new prospects for the identification of additional period-bouncers, providing impetus for theoretical studies of binary evolution.

Key words. X-rays: binaries – stars: individual: SDSS J151415.65+074446.5 – stars: individual: SDSS J121209.31+013627.7 – stars: individual: SDSS J125044.42+154957.4

1. Introduction

Cataclysmic variables (CVs) are interacting compact binaries where a white dwarf (WD) accretes matter from a Roche-lobe filling late-type donor (Warner 1995). Two main types of CVs have been distinguished according to the accretion geometry of the system in question. Usually, accretion onto the WD occurs via a disk, but if the WD magnetic field is strong enough (≥ 10 MG), the formation of an accretion disk is prevented and accretion flow proceeds directly from the companion toward the magnetic polar regions. In these high-field systems, called Polars, the WD rotation is phase locked at the orbital period (Cropper 1990). Polars are known to switch between high and low mass-accretion rate states spending roughly half their time in low states, as seen in the case of the prototype AM Her (Hessman et al. 2000), making their identification and characterization challenging (Pretorius et al. 2013).

In terms of evolution, all CVs follow a track from longer orbital periods toward shorter ones driven by angular momentum loss, which causes the orbital separation of the system to decrease (Knigge et al. 2011). In the course of this evolution, the

system passes through a period gap as a detached binary between an orbital period (P_{orb}) of 2–3 h, and reemerges as an active CV when the donor is again filling its Roche lobe (Howell et al. 2001). Through angular momentum loss due to gravitational radiation, the evolution continues toward even shorter periods until the system reaches a period minimum located at an orbital period of $P_{\text{min}} \approx 80$ min (see e.g., Howell et al. 2001; Patterson 2011; Pretorius et al. 2013; Goliash & Nelson 2015; McAllister et al. 2019; Pala et al. 2020, 2022). At the period minimum, the donor is out of thermal equilibrium because its mass-loss timescale is much shorter than its thermal timescale, causing the donor to stop shrinking in response to mass loss (King 1988). This results in the increase of the system’s orbital separation and consequently the CV bouncing back to longer orbital periods. These systems are dubbed “period-bouncers” (Patterson 1998). The actual contribution from period-bouncers to the total CV population is highly disputed, with estimations ranging between 40% and 70% and depending heavily on the formation and evolution model used as well as the assumptions made about the system’s parameters (see e.g., Schreiber et al. 2015; Belloni et al. 2020; Pala et al. 2020). However, as a matter

of fact, only a small number of period-bouncers and candidates have been observed and identified, mainly from the Sloan Digital Sky Survey (SDSS; Gänsicke et al. 2009; Littlefair et al. 2008), and a few of them have been shown to harbor a magnetic WD that possibly accretes at low rates (see e.g., Schmidt et al. 2005; Breedt et al. 2012).

The very low-mass donors (late M and L dwarfs) of period-bouncers have either no coronal X-ray emission or emission that is extremely weak and hardly detectable with present-day instrumentation (Audard et al. 2007; De Luca et al. 2020). Therefore, the detection of X-ray emission is a key diagnostic of ongoing mass accretion in the system, and hence it is the most promising path for the identification of period-bouncers. Another method for detecting mass accretion relies on the presence of H α emission. However, contrary to X-rays, this is not a reliable diagnostic of mass accretion in binaries with M or L dwarfs, since only upper limits to the mass accretion rate (\dot{M}_{acc}) can be obtained due to the possible contribution of the donor's chromospheric activity or its irradiation by the WD.

Candidate period-bouncers can also be identified through an excess of emission in the infrared spectrum over the WD contribution. Such emission could be produced by a very late-type donor, one of the key characteristics of these systems. Since CVs with a magnetic WD typically show a higher ratio between X-ray flux and optical flux, and thus higher X-ray luminosity, as they do not present a disk through which accretion luminosity is dissipated, we narrowed our search for period-bounce candidates to binaries composed by a magnetic WD with evidence for a very late-type companion. Of the few binaries where the presence of a very late-type companion has been spectroscopically confirmed, so far four have a magnetic WD. This includes EF Eri and V379 Vir (also known as SDSS J121209.31+013627.7), which were each detected as an X-ray source by White (1981) and Burleigh et al. (2006), respectively, as well as the two siblings of V379 Vir, SDSS J125044.42+154957.4 and SDSS J151415.65+074446.4 (henceforth SDSS 1250 and SDSS 1514), which have no X-ray emission reported in the literature. The nature of EF Eri is, presently, still unclear. Its orbital period locates EF Eri near the P_{min} for CVs, but the presence of a degenerate donor in the system is still debated. Schwöpe & Christensen (2010) favored a degenerate donor based on its estimated J -band brightness and the semi-empirical donor sequence of Knigge (2006). However, with *Gaia* Data Release 3 (DR3), the distance to EF Eri was revised to a much larger value, increasing the estimated absolute magnitude of the donor to above the substellar limit and thus weakening the arguments for a degenerate donor in the system.

Stelzer et al. (2017) detected X-ray orbital modulation on V379 Vir from a deep *XMM-Newton* observation, proving that the system is accreting and thus confirming it as a period-bounce system of the Polar type. Through modeling of the X-ray light curve, Stelzer et al. (2017) derived an X-ray luminosity of $\sim 3 \times 10^{29}$ erg s $^{-1}$ that, assuming a mass of $0.8 M_{\odot}$ and a radius of 7×10^8 cm for the WD, yields a mass accretion rate in the system of $3.2 \times 10^{-14} M_{\odot} \text{ yr}^{-1}$. The estimated value for the wind-driven mass accretion rate in this system is orders of magnitude too weak to explain the observed accretion rate and therefore is most likely not the accretion mechanism in the system. Additionally, donor stars in CVs are typically oversized as they are driven out of thermal equilibrium due to mass transfer (Knigge et al. 2011), making Roche-lobe overflow the most likely accretion mechanism.

However, whether V379 Vir is a typical magnetic period-bouncer rather than a peculiar system still has to be demon-

strated. To this end, we study the X-ray emission of systems SDSS 1250 and SDSS 1514, as they are composed of similar stellar components, namely a cool ($\sim 10\,000$ K) DA magnetic WD with a very low-mass companion (late M or L estimated spectral type). Neither of the systems has been previously detected in X-ray surveys. We used *XMM-Newton* with its European Photon Imaging Camera (EPIC) pn detector, which offers the largest collecting area among existing X-ray instruments.

Most of the confirmed detections of period-bouncers (see e.g., Patterson et al. 2005; McAllister et al. 2017; Neustroev et al. 2017; Pala et al. 2018; Schwöpe et al. 2021; Amantayeva et al. 2021; Kawka et al. 2021; Neustroev & Mäntynen 2023) have occurred through detailed observations of specific sources using different instruments in the X-ray, optical, and/or infrared bands. As a result, the sample of period-bouncers with complete and reliable system parameters is quite small and may not be representative of the period-bouncers as a class. With the launch of the extended ROentgen Survey with an Imaging Telescope Array (eROSITA; Predehl et al. 2021) onboard the Spektrum-Roentgen-Gamma mission (SRG; Sunyaev et al. 2021), we are now able to conduct new studies of the X-ray activity of period-bouncers. Even though the high sensitivity of instruments like *XMM-Newton* is required to identify accreting period-bounce systems, the enormous statistical samples of faint X-ray sources being observed by eROSITA are expected to boost the number of new detections and new identifications among period-bounce candidates. In this article, we carry out an analysis of the first detections of X-ray emission from period-bouncers based on the eROSITA All-Sky surveys, the last of which so far was completed in winter 2021.

The pilot sample of period-bounce candidates is introduced in more detail in Sect. 2. For SDSS 1514, we present a dedicated *XMM-Newton* observation in Sect. 3. In Sect. 4, we discuss the detections of period-bounce candidates from this sample in the source catalogs of eROSITA. Finally, we give our conclusions in Sect. 5.

2. Sample of period-bounce candidates

The pilot sample of short-period systems that we selected for our search of X-ray emission is drawn from Breedt et al. (2012). These systems (i.e., V379 Vir, SDSS 1250, and SDSS 1514) are composed of a magnetic WD and a presumably very low-mass donor. The WD has been previously identified as being magnetic based on SDSS spectra, specifically from the Zeeman splitting of the Balmer absorption lines (Schmidt et al. 2005; Vanlandingham et al. 2005; Külebi et al. 2009). This sample of candidates also shares some other characteristics, including large radial velocity variations, variable H α emission, a $\sim 10\,000$ K WD, and light curves taken with the Catalina Real-time Transient Survey that show no large-scale variability, eclipses, or high states.

The system V379 Vir is the only candidate with a near-IR spectrum where the donor's photospheric features of spectral type L8 were identified together with the contribution of cyclotron emission from the magnetic accreting WD (Farihi et al. 2008). In the absence of spectroscopic evidence, IR photometry can be used to estimate the donor spectral type of all three candidates: L5 or later for V379 Vir, estimated by Schmidt et al. (2005) by comparing the absolute J -band magnitude of the system to observed absolute J -band magnitudes of L and T dwarfs; L3 or later for SDSS 1514, estimated by Breedt et al. (2012) from the near-IR excess in the spectral energy distribution (SED); and M8 for SDSS 1250, estimated by

Table 1. Relevant properties of our pilot sample of period-bounce candidates.

Name	$d^{(1)}$ [pc]	P_{orb} [min]	SpT _{comp}	B_{WD} [MG]
V379 Vir	155 ± 4	$88.4^{(2)}$	L5-L8	$7^{(2)}$
SDSS 1514	181 ± 8	$88.7^{(3)}$	L3	$36^{(4)}$
SDSS 1250	132 ± 3	$86.3^{(3)}$	M8	$20^{(4)}$

Notes. ⁽¹⁾Distances from *Gaia*-DR3 parallax. ⁽²⁾Farihi et al. (2008). ⁽³⁾Breidt et al. (2012). ⁽⁴⁾Külebi et al. (2009).

Steele et al. (2011) by comparing the absolute *JH* band magnitude of the system to the observed absolute *JH* band magnitudes of M, L, and T dwarfs. At this spectral type, the secondary of SDSS 1250 would be slightly above the substellar limit on the donor sequence of Knigge (2006). However, the photometry used to estimate the donor spectral type was considered uncertain by Steele et al. (2011), making a spectroscopic confirmation mandatory for this system.

Some relevant system properties are summarized in Table 1. We identify the candidates by their shortened SDSS name or variable star designation in the first column of the table. The second column of the table reports the distance obtained from the *Gaia*-DR3 parallax. The third column shows the orbital period derived by different authors using the $H\alpha$ emission line. The fourth column presents the estimated spectral type of the donor, as described above, and the fifth column shows the estimated WD magnetic field strength.

To estimate the individual WD radii and masses, we fitted WD atmosphere models by Koester (2010) to the SDSS spectra¹ of the period-bounce candidates in our pilot sample while considering values for T_{eff} and $\log(g)$ previously reported in the literature. Because these systems are magnetic WDs, the Balmer lines cannot be used, and our fits rely solely on the continuum. Since we selected the appropriate model (T_{eff} , $\log(g)$) beforehand, the fit has a single parameter: the ratio between the observed flux from the SDSS spectrum and the model surface flux. This ratio represents the dilution factor, $(d/R_*)^2$, where d is the distance and R_* is the stellar radius. From the *Gaia*-DR3 distance we could therefore derive the WD radius. From the radius and an appropriate mass–radius relation, we obtained the WD mass.

For SDSS 1514 and SDSS 1250, we used the 10 000 K DA WD spectrum with $\log(g) = 8.0$ corresponding to the parameters derived by Breidt et al. (2012) for the two stars from the same SDSS spectra. With the *Gaia*-DR3 distances in Table 1, we obtained a WD radius of 7.0×10^8 cm for SDSS 1514 and of 7.2×10^8 cm for SDSS 1250. From these values, we derive the WD masses using the mass–radius relation by Nauenberg (1972) of $0.80 M_{\odot}$ and $0.77 M_{\odot}$, respectively.

For V379 Vir, we used a 11 000 K DA WD spectrum with $\log(g)=8.0$ following the WD temperature obtained by Burleigh et al. (2006) for the same SDSS spectra and assumed a $\log(g)$ similar to the other candidates in our pilot sample. With the *Gaia*-DR3 distance in Table 1, we obtained a WD radius of 8.3×10^8 cm, and from this value, we derived a WD mass using the mass–radius relation by Nauenberg (1972) of $0.64 M_{\odot}$.

We report that Gentile Fusillo et al. (2021) derived a WD mass for all three systems in our sample using *Gaia* photometry and astrometry to fit stellar parameters. From

Table 2. X-ray count rate and PF from a sine fit for SDSS 1514 EPIC/pn data in different energy bands.

Energy [keV]	Band label	Net source rate [cts s ⁻¹]	PF _{sine}
0.2–12.0	B	0.0335 ± 0.0013	1.0
0.2–1.0	S	0.0181 ± 0.0009	1.0
1.0–2.0	M	0.0096 ± 0.0006	1.0
2.0–12.0	H	0.0058 ± 0.0006	0.96 ± 0.02

this fitting process, they obtained effective temperatures of $10\,668 \pm 444$ K, 8057 ± 1234 K, and 8211 ± 311 K and a $\log(g)$ of 8.0 ± 0.1 , 7.6 ± 0.5 , and 7.8 ± 0.1 for V379 Vir, SDSS 1514, and SDSS 1250, respectively. Using a pure-H atmosphere model Gentile Fusillo et al. (2021) obtained a WD mass of $0.62 \pm 0.07 M_{\odot}$, $0.41 \pm 0.20 M_{\odot}$, and $0.48 \pm 0.05 M_{\odot}$ for V379 Vir, SDSS 1514, and SDSS 1250 respectively. The values for V379 Vir are consistent with the ones applied to the SDSS spectra. For the other two candidates, the values are considerably lower than the ones we obtained from the SDSS spectra.

3. XMM-Newton observation of SDSS J1514

The observation of SDSS 1514 by *XMM-Newton* occurred on January 14, 2020. It had a duration of 41 ks (Obs-ID 0840380201; PI Stelzer) and was performed with all EPIC instruments (Strüder et al. 2001; Turner et al. 2001) using the THIN filter, and with the Optical Monitor (OM; Mason et al. 2001) in FAST MODE using the V-band filter.

3.1. X-ray data

The system SDSS 1514 was detected in all EPIC instruments, giving a net count rate of 0.0042 ± 0.0004 cts s⁻¹ in the MOS1 and of 0.0121 ± 0.0011 cts s⁻¹ in the MOS2 cameras. Considering how faint the source is in the MOS instrument, we limited the analysis to EPIC/pn, which provides the highest sensitivity of the EPIC detectors, as can be seen in the net source count rates presented in Table 2. The data analysis was carried out with *XMM-Newton*'s Standard Science Analysis System (SAS) version 19.1.0. The observation is slightly affected by a flaring particle background; therefore, we retained only the events for which the count rate measured over the full detector area fulfills $\text{RATE} \leq 0.6$ cts s⁻¹, leaving an exposure time of 37 ks for the analysis. We filtered the data for pixel patterns ($\text{PATTERN} \leq 4$), quality flag ($\text{FLAG} = 0$), and events channels ($200 \leq \text{PI} \leq 12\,000$). Source detection was performed in three energy bands, namely, 0.2–1.0 keV (S), 1.0–2.0 keV (M), and 2.0–12.0 keV (H), using a customized procedure based on the steps implemented in the SAS task EDETECT_CHAIN.

For the spectral and temporal analysis we defined a circular photon extraction region with radius of 30'' centered on the EPIC/pn source position. To ensure a homogeneous signal, the background was taken as the average of three adjacent circular regions on the same CCD chip, each with a radius of 30''. The background subtraction of the light curve was carried out with SAS task EPICLCCORR, which also corrects for instrumental effects, on an event list that was previously barycenter corrected using the SAS tool BARYCEN.

The X-ray light curve shows a clear periodic modulation in all energy bands and a larger amplitude for softer emission,

¹ <https://dr9.sdss.org/>

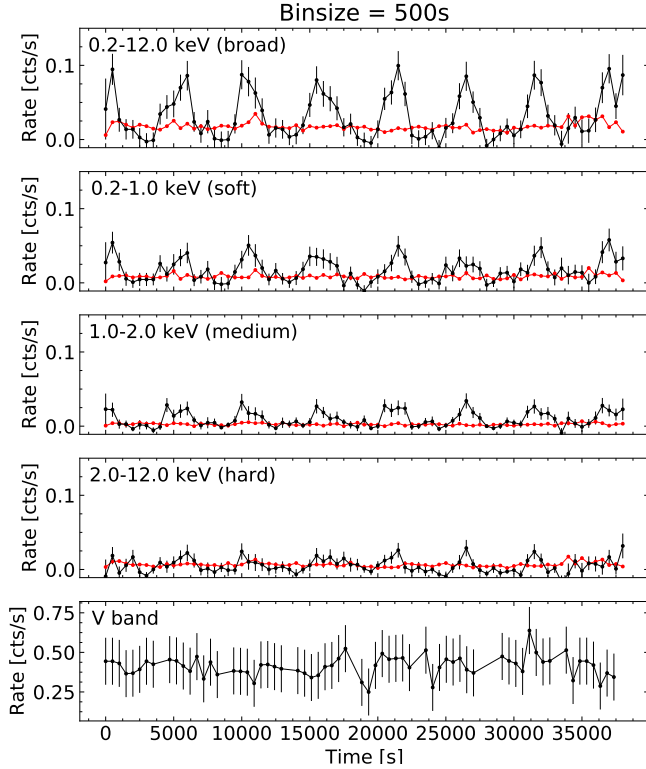


Fig. 1. EPIC/pn X-ray light curve of SDSS 1514 in four energy bands plus the OM *V*-band light curve. The energy band is indicated in the upper-left corner of each panel. The bin size is 500 s in all panels. The X-ray light curves represent the background-subtracted source signal (black), and background signal (red) is included for comparison.

as can be observed in Fig. 1. The modulation displays an on-off behavior that is typical for Polars (Cropper 1990). In the minimum, the count rate drops to approximately zero, suggesting that the area of accretion, presumably the magnetic pole cap of the WD, is completely occulted. A Lomb-Scargle periodogram analysis of the broad-band light curve yielded a period of $P_{\text{orb}} = 87.93 \pm 0.30$ min. This value and its 1σ error were derived with a bootstrap approach from 5000 simulated broad-band light curves that were generated by drawing the count rates of individual bins randomly from the range defined by the count rate errors. This period is in good agreement with the published period derived from the $H\alpha$ emission (88.7 min; Breedt et al. 2012).

To first approximation, we fitted a sinusoid to the X-ray light curve of each energy band. We determined the pulsed fraction (PF) taking into account the uncertainties on the y-offset and amplitude of the sine curve. The values obtained for the individual energy bands (see Table 2) are consistent with the 100% PF typically observed in Polars (Norton & Watson 1989). The phase-folded light curve shown in Fig. 2 was obtained using the High Energy Astrophysics Science Archive Research Center (HEASARC) tool EFOLD, which uses an input of 11 phase bins to calculate a new bin time of 479.61 s corresponding to the duration of a phase bin in the folded light curve. The folded light curve more clearly displays the already mentioned on-off behavior with a faint phase that is slightly longer than the bright phase.

We used Fig. 2 to constrain the geometry of the system. Radial accretion at the magnetic pole can be described by the

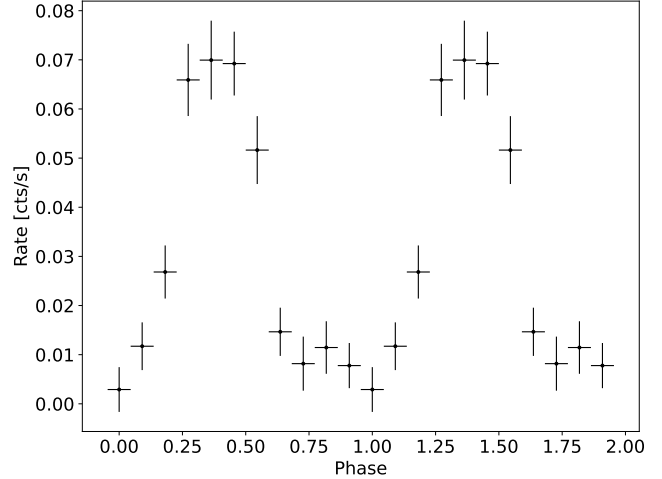


Fig. 2. X-ray light curve (EPIC/pn 0.2–12 keV) of SDSS 1514 folded using the period determined from the X-ray signal. The bin size is 479.61 s.

duration of the faint phase (γ) in fractions of the orbital period, where the WD is viewed at an angle i to the rotation axis (the inclination) such that the magnetic pole is located at a colatitude β (angle between the rotation and the magnetic axis) given by Cropper (1990) as

$$\beta = \arctan\left(\frac{\cot i}{\cos \pi\gamma}\right). \quad (1)$$

We did not see evidence of eclipses in the *V*-band lightcurve (Fig. 1), meaning that we could therefore set a rough upper limit to the inclination of $i < 75^\circ$. Considering that we observed occultation in the X-ray light curve, a lower limit was assumed at $i > 10^\circ$ so that the hot spot moved in and out of view due to the rotation of the WD. Together with the observed duration of the faint phase ($\gamma = 0.46$) determined from the folded light curve in Fig. 2, we found a range of $65^\circ < \beta < 89^\circ$ for the colatitude of the magnetic pole using Eq. (1). This result gave us information about the geometry of the system. For $\beta < 90^\circ$, the accreting pole is on the same side of the orbital plane as our line of sight. The high value for β suggests a large misalignment between the rotation axis of the WD and its magnetic field. In Fig. 2, the shape of the folded X-ray light curve indicates that the rise and decline to the maximum are approximately of the same duration. This suggests that the emission region is symmetrical; however, with the available data we could not discern if the extent is vertical or lateral.

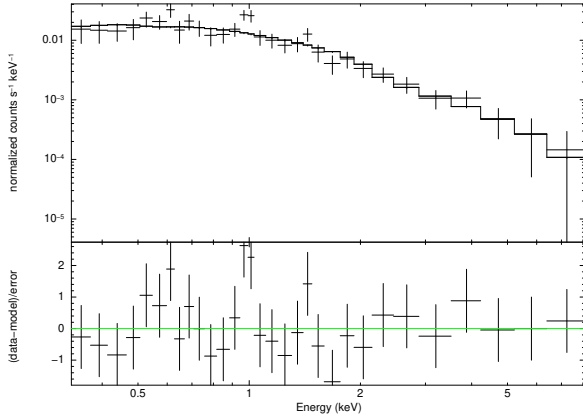
To constrain the properties of the X-ray emitting plasma, we fitted the EPIC/pn spectrum of SDSS 1514 using the X-Ray Spectral Fitting Package (XSPEC; Arnaud 1996). We performed two separate fits considering, in both cases, a simple absorber (TBABS), the first with a single-component thermal model (APEC) and the second with a thermal Bremsstrahlung model (BREMS). The APEC fit was carried out using the abundances from Asplund et al. (2009).

The BREMS and the APEC models provided consistent values for the X-ray temperature of the system (see Table 3). For the APEC model, we obtained a subsolar abundance that is however ill-constrained, and its uncertainty also allowed for zero metallicity. This might be explained by the lack of strong emission lines at the plasma temperature of about 4 keV as well as the low S/N ratio of the spectrum, thus justifying the use of a

Table 3. Best-fit parameters for the *XMM-Newton* EPIC/pn spectrum of SDSS 1514 and values corresponding to upper and lower 90% confidence ranges.

Model	χ^2_{red} (d.o.f.)	N_{H} [cm^{-2}]	kT [keV]	Z [Z_{\odot}]	Flux [$\text{erg cm}^{-2} \text{s}^{-1}$]	Emission measure [cm^{-3}]
TBABS*APEC	1.03 (27)	$1.9^{6.1}_{0.0} \times 10^{20}$	$3.75^{5.92}_{2.55}$	$0.04^{0.71}_{0.0}$	$7.20^{8.41}_{6.22} \times 10^{-14}$	$2.16^{2.46}_{1.72} \times 10^{51}$
TBABS*BREMSS	1.00 (28)	$1.6^{6.6}_{0.0} \times 10^{20}$	$3.84^{6.36}_{2.38}$	–	$7.21^{8.37}_{6.18} \times 10^{-14}$	$2.16^{2.66}_{1.87} \times 10^{51}$

Notes. The flux is given for the *XMM-Newton* broadband (0.2–12 keV).


Fig. 3. Time-averaged EPIC/pn X-ray spectrum of SDSS 1514 with the APEC model and residuals.

pure Bremsstrahlung model. The neutral hydrogen column density also appeared to be unconstrained and compatible with no absorption of the source. The range obtained from our spectral fits for the gas column density fell within the upper limit for the galactic absorption² in the direction of SDSS 1514, which is estimated at $2.2 \times 10^{20} \text{ cm}^{-2}$ (Bekhti et al. 2016). The BREMS and the APEC models yielded a similar χ^2_{red} , and we could not distinguish between these two models at the statistics of our observation. We show in Fig. 3 the observed EPIC/pn spectrum together with the APEC model and residuals.

We also performed several APEC fits with abundances fixed at different values and found that this has a negligible influence on the X-ray flux. Therefore, based on the average flux from all the different APEC fits we performed, we adopted an unabsorbed flux of $f_{\text{X}} = 7.3 \times 10^{-14} \text{ erg cm}^2 \text{ s}^{-1}$ in the 0.2–12 keV-band. For the 0.1–2.4 keV ROSAT band, the average X-ray flux is $4.5 \times 10^{-14} \text{ erg cm}^2 \text{ s}^{-1}$. This latter value is in accordance with the upper limit placed on the X-ray flux by the ROSAT non-detection at $\leq 6 \times 10^{-14} \text{ erg cm}^2 \text{ s}^{-1}$ for this energy band (Breedt et al. 2012). Using the best-fit APEC parameters and a dummy response that covers a broad energy range, we calculated the bolometric X-ray flux to obtain a bolometric correction factor of 1.10.

With its *Gaia*-DR3, distance we determine the bolometric X-ray luminosity to $\log(L_{\text{X}}) [\text{erg s}^{-1}] = 29.5$, and from this value, we derived a mass accretion rate of $\dot{M}_{\text{acc}} = 3.3 \times 10^{-14} M_{\odot} \text{ yr}^{-1}$, obtained by adopting the WD mass and radius derived in Sect. 2 for the SDSS spectra of SDSS 1514. A mass accretion rate of $\dot{M}_{\text{acc}} = 9.4 \times 10^{-14} M_{\odot} \text{ yr}^{-1}$ was obtained by adopting the WD mass and radius SDSS 1514 from

Gentile Fusillo et al. (2021). Similar to the conclusion reached by Stelzer et al. (2017), the estimated lower limit for the accretion rate in this system is orders of magnitude too high to be accounted for by a wind-driven mass accretion rate mechanism, making Roche-lobe overflow the most likely accretion mechanism for SDSS 1514.

Because we are working with magnetic targets, a contribution of cyclotron emission to the overall flux (and therefore luminosity) of the systems might be present. Cyclotron flux depends on several parameters, such as the electron temperature kT_e and density N_e , the magnetic field strength, and the angle between the line of sight and the magnetic field vector (see Schwope et al. 1990). Hence, even a rough estimate of cyclotron flux needs assumptions regarding several unknown parameters. In addition, at low accretion rates, the plasma is likely in a non-hydrodynamic regime. Thus, such quantification is beyond the scope of the present work. We instead preferred to report accretion rates for the sources obtained from X-ray data that should henceforth be taken as lower limits.

The EPIC/pn X-ray count rate in the minimum of the light curve ($0.64 \leq \phi \leq 1.09$) is $0.0083 \text{ cts s}^{-1}$ with a standard deviation of $0.0091 \text{ cts s}^{-1}$, that is, SDSS 1514 is undetected. We produced an EPIC/pn sensitivity map for the combined time intervals corresponding to the range of phases ϕ that define this minimum. We then multiplied the value of the count rate of this map at the source position with the rate-to-flux conversion factor derived from the time-averaged X-ray spectrum. This way, we obtained the upper limit to the X-ray emission at the orbital minimum of $\log L_{\text{X,min}} [\text{erg s}^{-1}] < 28.3$. The coronal emission of the only two L dwarfs detected in X-rays so far is $\log L_{\text{X,min}} [\text{erg s}^{-1}] < 27.0$ (Audard et al. 2007; De Luca et al. 2020). In other words, we did not obtain any constraints on the L dwarf’s X-ray emission from this observation.

3.2. Optical data

The *V*-band photometry acquired with the OM in FAST MODE was taken simultaneously with the X-ray observation and was extracted with the SAS task OMFCHAIN. In addition, the time series was barycenter corrected.

A Lomb-Scargle periodogram analysis of the *V*-band did not yield a significant periodicity, and when folded on the X-ray period, no phase-related variability was observed. The system SDSS 1514 is optically faint, and at the time of the observation, the system was at $V_{\text{OM}} = 18.92 \pm 0.32 \text{ mag}$, which is about one magnitude above the sensitivity limit of the OM. The variability for the *V*-band was obtained by converting the OM count rates into fluxes using the conversion factor given in the *XMM-Newton* SAS user guide³. We used the values for

² <https://heasarc.gsfc.nasa.gov/cgi-bin/Tools/w3nh/w3nh.pl>

³ <https://heasarc.gsfc.nasa.gov/docs/xmm/sas/USG/ommag.html>

Table 4. X-ray parameters from the eROSITA merged catalog eRASS:3 for V379 Vir and SDSS 1250 given for the eROSITA single band (0.2–2.3 keV).

Name	Detection likelihood	Separation ["]	Counts [cts]	Count rate [cts s ⁻¹]	Flux (APEC) [erg cm ⁻² s ⁻¹]	X-ray luminosity ^(*) [erg s ⁻¹]	Mass accretion rate ^(*) [M _⊙ yr ⁻¹]
V379 Vir	44.5	2.2	30.1 ± 6.3	0.08 ± 0.02	(0.75 ± 0.13) × 10 ⁻¹³	log(L _{bol}) = 29.5	5.3 × 10 ⁻¹⁴
SDSS 1250	19.9	2.9	16.5 ± 4.9	0.05 ± 0.01	(0.46 ± 0.12) × 10 ⁻¹³	log(L _{bol}) = 29.2	1.7 × 10 ⁻¹⁴

Notes. ^(*)Values do not consider potential contributions from cyclotron emission to the X-ray luminosity.

the average flux (flux_{avg}) and for the maximum flux (flux_{max}) in the light curve to estimate the magnitude change as $\Delta\text{mag} = -2.5 \log_{10}(\text{flux}_{\text{max}}/\text{flux}_{\text{avg}})$. This gave a variability amplitude of $\Delta\text{mag} = 0.47$ mag, or around 2.5%. This percentage is consistent with the variability estimate made by [Burleigh et al. \(2006\)](#) for the V-band light curve of V379 Vir of about 3%. However, as can be seen in Fig. 1, the variation in the OM light curve of SDSS 1514 is not significant, due to the low statistics of the OM data.

4. eROSITA detections

Four full-sky surveys have been carried out with eROSITA, namely, eRASS 1 to eRASS 4. Source catalogs from eRASS data are produced at the Max Planck Institut für extraterrestrische Physik (MPE) in Garching, Germany, with the eROSITA Science Analysis Software System (eSASS) described by [Brunner et al. \(2022\)](#). These catalogs are composed of all eRASS sources in the western half of the sky in terms of Galactic coordinates, that is, Galactic longitude $l \geq 180^\circ$, which is the sky area with German data rights.

To obtain the highest sensitivity for detecting the presumably faint period-bounce candidates, we used the merged catalog eRASS:3 that was generated from summing data from the first three all-sky surveys. The latest version of the eRASS:3 catalog, which was made available to us in December 2022, was produced with the data processing version 020⁴. Source detection was performed in this catalog for a single eROSITA energy band: 0.2–2.3 keV.

In order to search for the period-bouncers from our pilot sample in eRASS data, we performed an initial match between our targets and the *Gaia*-DR3 catalog. Using the corresponding *Gaia*-DR3 proper motions, we corrected the coordinates of the objects to the mean observing date of eRASS:3. Then we matched them with the eRASS:3 catalog, allowing for a maximum separation of 30". After establishing the closest matches for our pilot sample, we carried out a visual inspection in a 30" radius region around the X-ray source to assure that there where no other potential optical counterparts. In Table 4, we report the X-ray parameters obtained from the merged eRASS:3 catalog for the matches of the two period-bouncers with eROSITA detections, V379 Vir and SDSS 1250. The system SDSS 1514 is located in the sky area with exclusive Russian eROSITA data rights, and therefore, it is not included in the eRASS:3 catalog. As can be seen from Table 4, the sources are faint in the eRASS surveys, with only tens of counts in the merged data from the first three eROSITA surveys, yet they are significantly above the detection likelihood limit of five set for the eRASS:3 merged catalog.

⁴ The source catalog used in our work is [all_s3_SourceCat1B_221007_poscorr_mpe_clean.fits](#) (for eRASS:3).

Table 5. Rate-to-flux conversion factors in the eROSITA single band (0.2–2.3 keV).

$CF_{\text{fake,APEC}}$ [cts cm ² erg ⁻¹]	$CF_{\text{fake,powerlaw}}$ [cts cm ² erg ⁻¹]
4.23×10^{11}	4.09×10^{11}

Notes. On the left is a conversion factor for the simulated spectra obtained using an APEC model with $kT = 2.62$ keV, and on the right is a conversion factor obtained using a power law model with $\Gamma = 2.0$.

In the eROSITA eRASS:3 catalog, the single band flux was calculated for a power law model with an index $\Gamma = 2.0$ and a galactic absorption of $N_{\text{H}} = 3 \times 10^{20}$ cm⁻² ([Brunner et al. 2022](#)). Since this spectral model is not appropriate for CVs, we computed fluxes for an APEC model with the help of a simulation that provided us with the eROSITA conversion factor, $CF_{\text{eROSITA,APEC}}$, from count rate to thermal flux.

Next, we generated a “fake” spectrum using the FAKFIT command available in XSPEC together with the eROSITA response files. We chose an APEC model with $kT = 2.62$ keV, $N_{\text{H}} = 2.3 \times 10^{20}$ cm⁻² and an abundance of 0.11 Z_⊙, which are the values found from the *XMM-Newton* spectrum for one of our targets (see [Stelzer et al. 2017](#)). We then produced another simulated eROSITA spectrum for the power law model used in the eRASS catalogs. From both synthetic spectra, we then retrieved the flux and the count rate in the single band, using these values to calculate a $CF_{\text{fake,APEC}}$ and a $CF_{\text{fake,powerlaw}}$. The results are shown in Table 5, where it can be seen that these two CF s differ by only 3.36%. This result allowed us to derive the $CF_{\text{eROSITA,APEC}}$ from the $CF_{\text{eROSITA,powerlaw}}$ used in the eRASS catalogs. The final values for the APEC fluxes for the eROSITA single band (0.2–2.3 keV), given in Table 4, were calculated using the catalog count rate and the APEC eROSITA conversion factor as $\text{Flux}_{\text{APEC}} = \text{Count Rate}/CF_{\text{eROSITA,APEC}}$. Analogous to the analysis of the *XMM-Newton* data, the APEC parameters and a dummy response that covers a broad energy range were used to calculate the bolometric X-ray flux. We obtained a bolometric correction factor of 1.60. With the *Gaia*-DR3 distances, we obtained the bolometric X-ray luminosity and mass accretion rate of each of our targets (see Table 4) by using the WD mass and radius obtained for each object in Sect. 2. By using the values for the WD masses obtained by [Gentile Fusillo et al. \(2021\)](#) from *Gaia* photometry combined with a WD radius from the [Nauenberg \(1972\)](#) mass–radius relation, we obtained a mass accretion rate of $\dot{M}_{\text{acc}} = 5.5 \times 10^{-14}$ M_⊙ yr⁻¹ for V379 Vir and of $\dot{M}_{\text{acc}} = 3.7 \times 10^{-14}$ M_⊙ yr⁻¹ for SDSS 1250. In the latter case, the mass accretion rate is more than two time greater than the value we calculated based on the WD mass from the SDSS spectra.

5. Discussion and conclusions

We detected X-ray emission from all three magnetic period-bouncer candidates. These systems are emitting at a similar level of $L_x \approx 10^{29}$ [erg s⁻¹] and hence displaying similar mass accretion rates under the assumption that the WD mass is similar in all systems.

In Stelzer et al. (2017), an APEC flux value was reported for V379 Vir in the *XMM-Newton* broadband (0.2–12.0 keV) of 1.3×10^{-13} erg cm⁻² s⁻¹. Since the X-ray spectra of V379 Vir and SDSS 1514 are very similar we can use the *XMM-Newton* spectrum of SDSS 1514 analyzed in this paper to estimate the flux of V379 Vir in the eROSITA band at its *XMM-Newton* epoch. In XSPEC, we calculated a flux ratio of 1.76 for SDSS 1514 between the *XMM-Newton* broadband and the 0.2–2.3 keV-band used in the eRASS:3 catalog. From this, we inferred the flux of V379 Vir in the eRASS:3 energy band at the *XMM-Newton* epoch to be 7.1×10^{-14} erg cm⁻² s⁻¹. A comparison with the observed eROSITA flux presented in Table 4 for V379 Vir showed that there is only a 5.7% difference between the two values, and considering the error bars, the two brightness measurements are consistent with each other, that is, the system’s X-ray luminosity (averaged over the orbital cycle) did not change on timescales of a few years.

For two of the three systems, V379 Vir and SDSS 1514, we found X-ray orbital modulation through the long, sensitive *XMM-Newton* observations presented by Stelzer et al. (2017) and this paper respectively. The fluxes discussed in the previous paragraph therefore represent time averages over several orbital cycles. In the case of eROSITA, the flux is the average over three surveys separated from each other by six months. Within each survey, V379 Vir and SDSS 1250 were observed between 6 and 11 times for around 20 s–40 s with a gap of approximately 4 h between the individual exposures, as defined by the scanning law of eROSITA (see e.g., Predehl et al. 2021). Given the faintness of the sources, we refrained from performing a search of variability in the eRASS data.

The X-ray detection of our targets confidently proves that accretion is taking place. We have thus demonstrated that X-ray emission is an efficient way of identifying CVs with very low-mass donors. While the periodic X-ray variability testifying to the accretion geometry requires a high sensitivity that can only be achieved with dedicated X-ray pointings, we have shown that the flux limit of the merged data from the eROSITA surveys is sufficient to provide a weak detection for systems at distances out to ~200 pc. A rough projection of the prospects for a systematic search for period-bouncers in the eRASS:3 catalog can be done using the X-ray flux limit of the survey and an estimate of the space density of CVs in an exponential disk.

To this end, we used the fainter eRASS detection among our pilot sample, SDSS 1250, as a reference point to estimate the distance limit for period-bouncers of eRASS:3. Using a detection likelihood of DET_ML > 20, which corresponded to the value for SDSS 1250 (see Table 4), 95% of the sources in the eRASS:3 catalog have a flux higher than 2×10^{-14} erg cm⁻² s⁻¹. Combined with the “typical” X-ray luminosity of our pilot targets (10^{29} erg s⁻¹) this yielded an approximate distance limit of ~200 pc for eROSITA discoveries of accreting WDs with very low-mass donors in the merged eRASS 1 to eRASS 3 database. We caution that this estimate may apply only to magnetic systems that tend to be X-ray brighter than non-magnetic CVs (Cropper 1990). On the other hand, our detection likelihood threshold is very conservative. Values of DET_ML = 11 have been

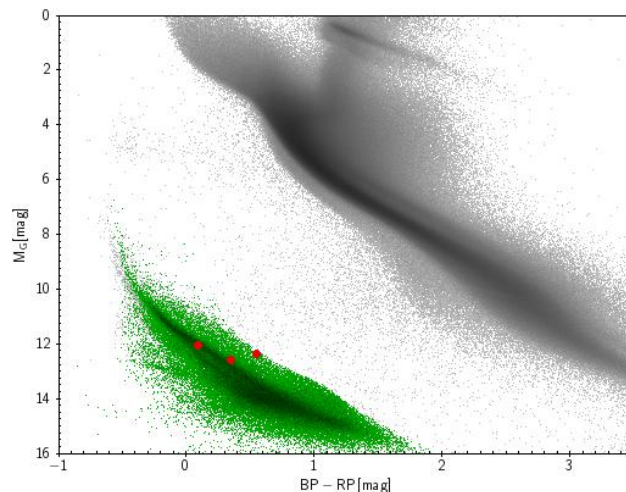


Fig. 4. *Gaia* color–magnitude diagram showing the position of the “high-fidelity” WDs from Gentile Fusillo et al. (2021) with a distance limit of 200 pc (green). The three period-bouncers from our pilot sample that are also in the Gentile Fusillo et al. (2021) catalog are shown in red. The *Gaia*-DR3 sources with Bailer-Jones et al. (2021) distances are shown in gray as a reference.

shown to define samples with only modest contamination by spurious sources (Wolf et al. 2021).

A possible starting point in the search of new period-bounce candidates is the *Gaia* catalog of WDs by Gentile Fusillo et al. (2021), which presents a list of approximately 360 000 genuine WDs and was constructed through a comprehensive selection based on *Gaia* magnitudes and colors with consideration for diverse quality flags. In Fig. 4, we display as a green sample the “high-fidelity” WDs with distances within the eRASS:3 limit estimated above.

The “high-fidelity” WDs are objects with a probability of being a WD, $P_{WD} \geq 0.75$, as derived by Gentile Fusillo et al. (2019) from the position of the objects in the *Gaia* color–magnitude diagram compared to the WD density map obtained from confirmed SDSS WDs. The sample shown in Fig. 4 in green comprises 91 089 objects. Overlaid are the three period-bouncers from our pilot X-ray survey (marked in red), all of which are present in the Gentile Fusillo et al. (2021) catalog. All three are located in the same area as the *Gaia* WD subsample, indicating that the *Gaia* WD catalog by Gentile Fusillo et al. (2021) might include further period-bouncers.

In Fig. 4, we present in gray a large sample of *Gaia*-DR3 sources to serve as reference. This sample was selected considering only the sources with a distance obtained by Bailer-Jones et al. (2021) and a parallax error less than 1% of the parallax value.

The expected estimated number of period-bouncers within the eRASS:3 distance limit is determined by the space density of CVs, which is highly uncertain and ranges from 2×10^{-4} pc⁻³ (de Kool 1992) to 4.8×10^{-6} pc⁻³ (Pala et al. 2020). Considering this, for the space density of period-bouncers in the Galactic midplane, we assumed $\rho_0 \sim 10^{-5}$ pc⁻³, which is twice the value estimated for “normal” CVs from their observed X-ray luminosity function (Pretorius & Knigge 2012). An exponential vertical density profile with a scale height of 260 pc for short-period systems (Pretorius & Knigge 2012) then yields approximately 340 period-bouncers within 200 pc. Since the eRASS:3 catalog comprises only half of the sky, the actual

expected number of period-bouncers hidden in this catalog is around 170. When considering a 450 pc scale height proposed by Pretorius & Knigge (2012) specifically for period-bouncers, we obtained approximately 400 period-bouncers within 200 pc with around 200 period-bouncers that should be found in the eRASS:3 catalog. The number would be lower if the majority of period-bouncers had a lower X-ray luminosity than the benchmark systems we studied in this work. However, the theoretically predicted mass accretion rates (on the order of $\dot{M}_{\text{acc}} \sim 10^{-11} M_{\odot} \text{yr}^{-1}$; Goliashch & Nelson 2015) are much higher than expected from the observed L_X values, and this suggests that the number of X-ray detections might be substantially higher than the estimate above.

Considering the all-sky nature of eROSITA's surveys, this instrument is ideal for population studies. As we have shown here, with the detections of V379 Vir and SDSS J250, the eRASS data is suitable for searching for new period-bounce candidates. Once accretion has been proven in a system through an X-ray detection, an infrared spectrum should be obtained to confirm the late spectral type of the donor and thus confidently verify the system as a period-bouncer. The discovery of more period-bouncers and the observational characterization of this object class is expected to provide new impetus for theoretical studies of binary evolution.


Acknowledgements. We thank an anonymous referee for reviewing the original manuscript and giving helpful comments and useful advice. Daniela Muñoz-Giraldo acknowledges financial support from Deutsche Forschungsgemeinschaft (DFG) under grant number STE 1068/6-1. Domitilla de Martino acknowledges financial support from ASI and INAF. This work is based on observations obtained with *XMM-Newton*, an ESA science mission with instruments and contributions directly funded by ESA Member States and NASA. This work is based on data from eROSITA, the primary instrument aboard SRG, a joint Russian-German science mission supported by the Russian Space Agency (Roskosmos), in the interests of the Russian Academy of Sciences represented by its Space Research Institute (IKI), and the Deutsches Zentrum für Luft- und Raumfahrt (DLR). The SRG spacecraft was built by Lavochkin Association (NPOL) and its subcontractors, and is operated by NPOL with support from the Max Planck Institute for Extraterrestrial Physics (MPE). The development and construction of the eROSITA X-ray instrument was led by MPE, with contributions from the Dr. Karl Remis Observatory Bamberg and ECAP (FAU Erlangen-Nürnberg), the University of Hamburg Observatory, the Leibniz Institute for Astrophysics Potsdam (AIP), and the Institute for Astronomy and Astrophysics of the University of Tübingen, with the support of DLR and the Max Planck Society. The Argelander Institute for Astronomy of the University of Bonn and the Ludwig Maximilians Universität München also participated in the science preparation for eero. The eROSITA data shown here were processed using the eSASS/NRTA software system developed by the German eROSITA consortium. This work has made use of data from the European Space Agency (ESA) mission *Gaia* (<https://www.cosmos.esa.int/gaia>), processed by the *Gaia* Data Processing and Analysis Consortium (DPAC, <https://www.cosmos.esa.int/web/gaia/dpac/consortium>). Funding for the DPAC has been provided by national institutions, in particular the institutions participating in the *Gaia* Multilateral Agreement.

References

Amantayeva, A., Zharikov, S., Page, K., et al. 2021, *ApJ*, 918, 58
 Arnaud, K. 1996, in *Astronomical Data Analysis Software and Systems V*, ASP Conf. Ser., 101, 17

Asplund, M., Grevesse, N., Sauval, A. J., & Scott, P. 2009, *ARA&A*, 47, 481
 Audard, M., Osten, R., Brown, A., et al. 2007, *A&A*, 471, L63
 Bailer-Jones, C. A. L., Rybizki, J., Fouesneau, M., Demleitner, M., & Andrae, R. 2021, *AJ*, 161, 147
 Bekhti, N. B., Flöer, L., Keller, R., et al. 2016, *A&A*, 594, A116
 Belloni, D., Schreiber, M. R., Pala, A. F., et al. 2020, *MNRAS*, 491, 5717
 Breedt, E., Gaensicke, B. T., Girven, J., et al. 2012, *MNRAS*, 423, 1437
 Brunner, H., Liu, T., Lamer, G., et al. 2022, *A&A*, 661, A1
 Burleigh, M. R., Marsh, T., Gänsicke, B., et al. 2006, *MNRAS*, 373, 1416
 Cropper, M. 1990, *Space Sci. Rev.*, 54, 195
 de Kool, M. 1992, *A&A*, 261, 188
 De Luca, A., Stelzer, B., Burgasser, A. J., et al. 2020, *A&A*, 634, L13
 Farihi, J., Burleigh, M., & Hoard, D. 2008, *ApJ*, 674, 421
 Gänsicke, B., Dillon, M., Southworth, J., et al. 2009, *MNRAS*, 397, 2170
 Gentile Fusillo, N. P., Tremblay, P.-E., Gänsicke, B. T., et al. 2019, *MNRAS*, 482, 4570
 Gentile Fusillo, N., Tremblay, P., Cukanovaite, E., et al. 2021, *MNRAS*, 508, 3877
 Goliashch, J., & Nelson, L. 2015, *ApJ*, 809, 80
 Hessman, F., Gänsicke, B., & Mattei, J. 2000, *A&A*, 361, 952
 Howell, S. B., Nelson, L. A., & Rappaport, S. 2001, *ApJ*, 550, 897
 Kawka, A., Vennes, S., Ferrario, L., et al. 2021, *MNRAS*, 507, L30
 King, A. 1988, *Quart. J. Royal Astron. Soc.*, 29, 1
 Knigge, C. 2006, *MNRAS*, 373, 484
 Knigge, C., Baraffe, I., & Patterson, J. 2011, *ApJS*, 194, 28
 Koester, D. 2010, *Mem. Soc. Astron. Ital.*, 81, 921
 Külebi, B., Jordan, S., Euchner, F., Gänsicke, B., & Hirsch, H. 2009, *A&A*, 506, 1341
 Littlefair, S., Dhillon, V., Marsh, T., et al. 2008, *MNRAS*, 388, 1582
 Mason, K., Breeveld, A., Much, R., et al. 2001, *A&A*, 365, L36
 McAllister, M., Littlefair, S., Dhillon, V., et al. 2017, *MNRAS*, 467, 1024
 McAllister, M., Littlefair, S., Parsons, S., et al. 2019, *MNRAS*, 486, 5535
 Nauenberg, M. 1972, *ApJ*, 175, 417
 Neustroev, V., & Mäntynen, I. 2023, *MNRAS*, 523, 6114
 Neustroev, V., Marsh, T. R., Zharikov, S., et al. 2017, *MNRAS*, 467, 597
 Norton, A., & Watson, M. 1989, *MNRAS*, 237, 853
 Pala, A. F., Schmidtobreick, L., Tappert, C., Gänsicke, B. T., & Mehner, A. 2018, *MNRAS*, 481, 2523
 Pala, A., Gänsicke, B., Breedt, E., et al. 2020, *MNRAS*, 494, 3799
 Pala, A., Gänsicke, B., Belloni, D., et al. 2022, *MNRAS*, 510, 6110
 Patterson, J. 1998, *PASP*, 110, 1132
 Patterson, J. 2011, *MNRAS*, 411, 2695
 Patterson, J., Thorstensen, J. R., & Kemp, J. 2005, *PASP*, 117, 427
 Predehl, P., Andritschke, R., Arefiev, V., et al. 2021, *A&A*, 647, A1
 Pretorius, M. L., & Knigge, C. 2012, *MNRAS*, 419, 1442
 Pretorius, M. L., Knigge, C., & Schwope, A. D. 2013, *MNRAS*, 432, 570
 Schmidt, G. D., Szkody, P., Silvestri, N. M., et al. 2005, *ApJ*, 630, L173
 Schreiber, M. R., Zorotovic, M., & Wijnen, T. P. 2015, *MNRAS*, 455, L16
 Schwope, A., & Christensen, L. 2010, *A&A*, 514, A89
 Schwope, A., Beuermann, K., & Thomas, H.-C. 1990, *A&A*, 230, 120
 Schwope, A., Worpel, H., & Traulsen, I. 2021, *A&A*, 646, A181
 Steele, P., Burleigh, M., Dobbie, P., et al. 2011, *MNRAS*, 416, 2768
 Stelzer, B., de Martino, D., Casewell, S., Wynn, G., & Roy, M. 2017, *A&A*, 598, L6
 Strüder, L., Briel, U., Dennerl, K., et al. 2001, *A&A*, 365, L18
 Sunyaev, R., Arefiev, V., Babyshkin, V., et al. 2021, *A&A*, 656, A132
 Turner, M. J., Abbey, A., Arnaud, M., et al. 2001, *A&A*, 365, L27
 Vanlandingham, K. M., Schmidt, G. D., Eisenstein, D. J., et al. 2005, *AJ*, 130, 734
 Warner, B. 1995, *Cataclysmic Variable Stars*, (Cambridge: Cambridge University Press), 28
 White, N. 1981, *ApJ*, 244, L85
 Wolf, J., Nandra, K., Salvato, M., et al. 2021, *A&A*, 647, A5

Cataclysmic variables around the period-bounce: An eROSITA-enhanced multiwavelength catalog[★]

Daniela Muñoz-Giraldo¹, Beate Stelzer¹ , and Axel Schwobe²

¹ Institut für Astronomie und Astrophysik, Eberhard-Karls Universität Tübingen, Sand 1, 72076 Tübingen, Germany
e-mail: munoz-giraldo@astro.uni-tuebingen.de

² Leibniz-Institut für Astrophysik Potsdam (AIP), An der Sternwarte 16, 14482 Potsdam, Germany

Received 26 January 2024 / Accepted 12 June 2024

ABSTRACT

Context. Cataclysmic variables (CVs) with degenerate donors that have evolved past the period minimum are predicted to make up a great portion of the CV population, namely, between 40% and 80%. However, either due to shortcomings in the models or the intrinsic faintness of these strongly evolved systems, only a few of these so-called “period-bouncers” have been confidently identified thus far.

Aims. We compiled a multiwavelength catalog of period-bouncers and CVs around the period minimum from the literature to provide an in-depth characterization of the elusive subclass of period-bounce CVs that will support the identification of new candidates.

Methods. We combined recently published or archival multiwavelength data with new X-ray observations from the all-sky surveys carried out with the extended ROentgen Survey with an Imaging Telescope Array (eROSITA) on board the Spektrum-Roentgen-Gamma spacecraft (SRG). Our catalog comprises 192 CVs around the period minimum, chosen as likely period-bounce candidates based on reported short orbital periods and low donor mass. This sample helped us establish specific selection parameters, which were used to compile a “scorecard” that rates the likelihood that a particular system is a period-bouncer.

Results. Our “scorecard” correctly assigns high scores to the already confirmed period-bouncers in our literature catalog. It has also identified 103 additional strong period-bounce candidates in the literature that had not previously been classified as such. We established two selection cuts based on the X-ray-to-optical flux ratio ($-1.21 \leq \log(F_x/F_{\text{opt}}) \leq 0$) and the typical X-ray luminosity ($\log(L_{x,\text{bol}}) \leq 30.4$ [erg s⁻¹]) observed from the eight period-bouncers that have already been confirmed with eROSITA data. These X-ray selection cuts led to the updated categorization of seven systems as new period-bouncers, increasing their known population to 24 systems in total.

Conclusions. Our multiwavelength catalog of CVs around the period minimum drawn from the literature, together with X-ray data from eROSITA, has resulted in a ~40% increase in the population of period-bouncers. Both the catalog and “scorecard” we constructed will aid in future searches for new period-bounce candidates. These tools will contribute to the goal of resolving the discrepancy between the predicted high number of period-bouncers and the low number of these systems successfully observed to date.

Key words. catalogs – novae, cataclysmic variables – X-rays: binaries

1. Introduction

Cataclysmic variables (CVs) are interacting compact binaries where a white dwarf (WD) accretes matter from a Roche-lobe filling, late-type donor (Warner 1995). According to Paczynski (1976), CVs are the result of a common envelope (CE) phase in the evolution of the binary, where the envelope of a Roche-lobe filling, more massive primary star expands enough to engulf the companion. The envelope is then ejected from the binary, leaving a post-common envelope binary composed by the evolved core of the primary (now a WD) and a low-mass companion still on the main-sequence. At the end of the CE phase the orbital separation of the binary system has been significantly reduced due to friction in the CE that extracts angular momentum and energy from the system. Once the binary separation is close enough to allow mass transfer onto the WD, the system morphs into a CV.

In terms of evolution, all CVs follow a track from longer orbital periods towards shorter ones driven by angular momentum loss which causes the orbital separation (and thus the orbital

period) of the system to decrease (Paczynski 1976, Kolb 1993, Warner 1995). For systems with long orbital periods ($P_{\text{orb}} > 3$ h) the dominant angular momentum loss mechanism according to the “standard model” is magnetic braking, arising from the stellar wind associated with the secondary’s magnetic activity (see e.g. Mestel 1968; Verbunt & Zwaan 1981). The evolution of the CV continues until an orbital period of around 3 h, when the secondary becomes fully convective and (according to the standard model) magnetic braking abruptly stops causing a reduced mass transfer rate in the system. This eventually leads to the secondary detaching from its Roche-lobe (King 1988; Ritter 1991), marking the beginning of the “period gap” ($3 \text{ h} \lesssim P_{\text{orb}} \lesssim 2 \text{ h}$), which contains detached CVs. In the standard model, these CVs lose angular momentum exclusively as a result of gravitational radiation (Spruit & Ritter 1983). At the lower boundary of the gap, the secondary is filling its Roche-lobe once again, thereby allowing for the re-start of mass transfer in the system (Kolb et al. 1998).

According to this paradigm, the system re-emerges from the period gap as a short-period CV with angular momentum loss driven exclusively by gravitational radiation (Paczynski 1976). However, the evolutionary track generated by considering gravitational radiation as the only mechanism of

[★] Full Tables 3 and B.2 are available at the CDS via anonymous ftp to cdsarc.cds.unistra.fr (130.79.128.5) or via <https://cdsarc.cds.unistra.fr/viz-bin/cat/J/A+A/687/A305>

angular momentum loss does not comply with observations. [Knigge et al. \(2011\)](#) showed that in order to reproduce the observed evolution of short-period CVs, the angular momentum loss mechanism has to be around 2.5 times stronger than pure gravitational radiation. The origin and nature of this enhanced mechanism for angular momentum loss in short-period CVs is a topic of active discussion, with a wide variety of “recipes” having been suggested ([Politano 1996](#); [Zorotovic et al. 2011](#); [Wijnen et al. 2015](#); [Belloni et al. 2020](#)). Amongst these proposals, we highlight the empirical model for consequential angular momentum loss ([Schreiber et al. 2016](#)), which appears to solve several major disagreements among theory and observations, even though the physical mechanism behind the additional angular momentum loss is unclear.

Both magnetic and non-magnetic systems can be found amongst short-period CVs. Magnetic systems, which make up around one-third of CVs ([Wickramasinghe & Ferrario 2000](#); [Pretorius et al. 2013](#); [Pala et al. 2020](#)), can be further categorized depending on the strength of their magnetic field into polars, with $B \geq 10$ MG, which suppresses the formation of an accretion disk forcing the accretion flow to follow the magnetic field lines ([Cropper 1990](#)), and intermediate polars, with $1 \leq B \leq 10$ MG and allowing for a vestigial disk to form ([Patterson 1994](#)). Meanwhile, accretion remains primarily through the magnetic field lines.

Short-period CVs, below the period gap, continue to evolve towards even tighter orbits until the system reaches a period minimum. At this point the degenerate donor is out of thermal equilibrium due to its mass-loss timescale becoming much shorter than its thermal timescale, causing the donor to stop shrinking in response to mass-loss ([King 1988](#)). The donor, not being able to sustain hydrogen burning, becomes a brown dwarf ([Howell et al. 2001](#)). This change in internal structure results in the increase of the system’s orbital separation and consequently the CV bouncing back to longer orbital periods. The systems that go through this process of “bounce-back” to longer periods are known as period-bouncers ([Patterson 1998](#)).

Even though the presence of a period minimum has always been a defining characteristic of theoretical models describing CV evolution ([Paczynski & Sienkiewicz 1983](#); [Howell et al. 2001](#); [Rappaport et al. 1982](#); [Kolb & Baraffe 1999](#)), evidence supporting its existence only came with a Sloan Digital Sky Survey (SDSS) study of CVs by [Gänsicke et al. \(2009\)](#). A period spike at $80 \text{ min} \leq P_{\text{orb}} \leq 86 \text{ min}$ was observed providing clear evidence of a “pile-up” of systems that are slowly evolving through the period minimum.

One of the key predictions of theoretical models describing CV evolution is that period-bouncers are expected to make-up the majority of the CV population. Fractions between 40% and 80% of all CVs should have evolved beyond the period minimum, depending heavily on the formation and evolution model used as well as the assumptions made about the systems parameters (see e.g., [Kolb 1993](#); [Goliash & Nelson 2015](#); [Belloni et al. 2020](#)). However, from a volume-limited sample study of CVs by [Pala et al. \(2020\)](#) within 150 pc, the observed fraction of period-bouncers is only between 7% and 14%; also, to date there have been fewer than 20 confirmed period-bouncers (see e.g., [Patterson et al. 2005b](#); [McAllister et al. 2017](#); [Neustroev et al. 2017](#); [Pala et al. 2018](#); [Schwope et al. 2021](#); [Amantayeva et al. 2021](#); [Kawka et al. 2021](#); [Muñoz-Giraldo et al. 2023](#)). This under-representation may be due to selection biases against period-bouncers, as their defining characteristics of being old and faint CVs with low luminosity and mass transfer make their detection challenging ([Patterson 2011](#)).

Several recent studies suggest dwarf novae as the most likely source for the missing population of period-bouncers (see e.g., [Uemura et al. 2010](#), [Kimura et al. 2018](#)). These non-magnetic CVs are characterized by the presence of an accretion disk around the WD which can be observationally identified due to the quasi-periodic changes in brightness known as “outbursts” ([Meyer & Meyer-Hofmeister 1984](#)). Dwarf novae can be further classified into several sub-classes depending on the behavior of the outbursts. Furthermore, SU UMa systems are characterized for not only exhibiting outbursts, but also superoutbursts which can last up to several weeks ([Vogt 1980](#)). An interesting, and useful, property of these superoutbursts is that they are accompanied with the presence of “superhumps” that originate from donor-induced tidal dissipation of an eccentric accretion disk in a 3:1 orbital resonance ([Whitehurst 1988](#); [Osaki 1989](#)). The period of these “superhumps”, which is expected to be a few percent longer than the orbital period ([Patterson et al. 2005a](#)), has been established to scale with the mass ratio of the system. This makes it an ideal tool for estimating the masses of the individual components in the CV ([Patterson et al. 2005a](#); [Kato & Osaki 2013](#)).

The vast majority of SU UMa are located below the period gap, with donors that are usually M-type or later, making it common to describe the overall short-period non-magnetic CV population as SU UMa-type objects ([Kato et al. 2009](#) and further papers in this series). When an SU UMa has been established through observations to have extremely long outburst recurrence times (in the order of years to decades), a very low mass transfer rate (on the order of $10^{-11} M_{\odot} \text{ yr}^{-1}$), or a low-mass donor, this CV can be further categorized as a WZ Sge system ([Patterson et al. 2002](#); [Kato 2015](#)). In brief, WZ Sge-type CVs have usually the shortest orbital periods of the overall non-magnetic CV population and very low mass donors which may be brown dwarfs ([Kato 2022](#)). In fact, the majority of systems found in the “period spike” are classified as WZ Sge-type CVs ([Gänsicke et al. 2009](#)), which further supports this theory. This has led to the population of already identified WZ Sge-type objects being established as a good source for finding new period-bounce candidates. However, it is important to consider that these objects are detected primarily through photometric studies of optical superoutburst light curves. This means that they are not easily observed in quiescence due to their faintness and, therefore, they have remained largely undetected in other wavelengths, making a straightforward classification as a period-bouncer challenging.

Spectroscopic studies using a variety of instruments including the *Hubble* Space Telescope (HST) and SDSS (see e.g., [Pala et al. 2022](#), [Inight et al. 2023b](#)) are also an important source for period-bounce candidates. Spectra in the ultra-violet (UV) and optical bands in the case of period-bouncers are strongly dominated by the WD, often with no contribution from the late-type donor at all. This introduces new possibilities and challenges in the search for period-bouncers as potential candidates could be found in single WD catalogs ([Inight et al. 2023b](#)) in great numbers, but it makes it necessary to distinguish between these systems. Period-bouncers could also be incorrectly categorized as detached binaries, specially considering the low mass transfer rates that they exhibit ([Inight et al. 2021](#); [Schreiber et al. 2023](#)). V379 Vir is a confirmed period-bouncer that was initially assumed to be a detached binary ([Schmidt et al. 2005](#)); however, it was later proven to be accreting through the detection of orbital modulation from a deep X-ray observations using *XMM-Newton* ([Stelzer et al. 2017](#)).

Considering that coronal X-ray emission is not expected from the very late-type donors of period-bouncers

(Audard et al. 2007; De Luca et al. 2020), the detection of X-ray emission is a key diagnostic of ongoing mass accretion in these systems, which unequivocally distinguishes period-bouncers from isolated WDs and detached binaries, and hence is the most promising path for the identification of new candidates. Even though the high sensitivity of X-ray instruments, such as *XMM-Newton*, is useful when identifying accreting period-bounce systems, the use of all-sky surveys might be more pertinent for the large-scale search of period-bouncers that is required in order to bring the number of detected systems up to the expected values.

With the launch of the extended ROentgen Survey with an Imaging Telescope Array (eROSITA; Predehl et al. 2021) on board the Spektrum-Roentgen-Gamma mission (SRG; Sunyaev et al. 2021) we gained access to large statistical samples of X-ray sources. The first eROSITA detections of confirmed period-bouncers (Muñoz-Giraldo et al. 2023) proved the capabilities of this instrument in the study and classification of such faint sources. This supports its application as a reliable tool for the identification of new period-bounce candidates. The X-ray study of period-bouncers with eROSITA will help us establish the class properties that will aid in the search for new candidates in the future, with the aim of resolving the discrepancy between observed and predicted fraction of period-bouncers.

The main focus of this study is to produce a catalog of CVs around the period minimum, namely, potential period-bouncers, which were already discussed in the literature, in order to characterize in detail the elusive subclass of period-bounce CVs. To this end, we constructed a literature catalog including both confirmed period-bouncers and candidates. The inclusion of confirmed period-bouncers allows us to use their reported parameters to rate how likely the other candidates are of being a period-bouncer. This catalog will also provide a reliable observational data set that could be used for any future theoretical modelling of advanced CV evolution.

Our literature catalog of period-bounce candidates is introduced in more detail in Sect. 2. We provide specific information in the selection of candidates, followed by an overview of the parameter values used from the literature and comments on the evolution of short-period CVs that can be derived from this information. We wrap up Sect. 2 with a discussion on the quality of the distance values used in the catalog. The process to obtain the photometry of the systems in the catalog is explained in Sect. 3. In Sect. 4 we introduce and explain in detail the scorecard we constructed in order to rate the likelihood a system has of being a period-bouncer. In Sect. 5, we discuss the eROSITA X-ray detections of period-bounce candidates from our catalog and we establish their X-ray characteristics. We present our conclusions in Sect. 6.

2. Literature catalog of period-bounce candidates

We have compiled a catalog of systems already reported in the literature that are characterized by being short-period CVs close to (or already past) the period minimum. This collection of CVs around the period-bounce constitutes an increase in the number of compiled systems of about an order of magnitude compared to earlier studies of period-bounce candidates (Littlefair et al. 2003; Knigge 2006; Gänsicke et al. 2009; Patterson 2011; Inight et al. 2023b). It also provides a comprehensive overview of what is currently known of CVs in the short-period regime.

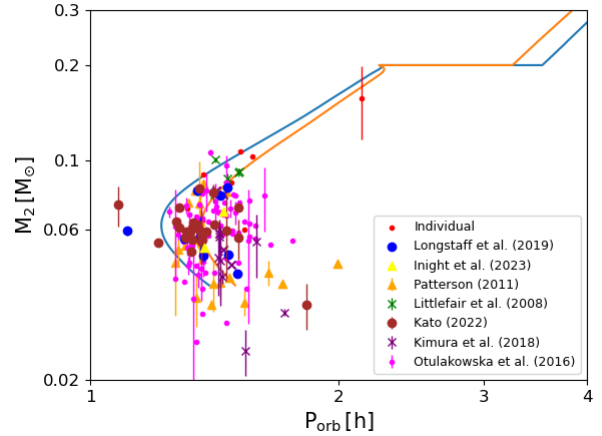


Fig. 1. Donor mass as a function of orbital period for the objects in our literature catalog of period-bounce candidates. The color and shape corresponds to the catalogs from which we took the system (and that are listed in the legend). Two CV evolution tracks from Knigge et al. (2011) are shown as reference: the standard track considering angular momentum loss only due to gravitational radiation (blue) and a revised track that considers enhanced angular momentum loss (orange).

2.1. Candidate selection

We manually went through different databases and individual papers in order to compile a “unified” catalog of potential members of the widely elusive subclass of CVs known as period-bouncers. To this end, we initially selected objects that had a very low donor mass with an orbital period placing them around the period minimum or in the post-bounce area. Additionally, we also included systems that were suggested as good period-bounce candidates even if they either had no reported orbital period/donor mass or their literature parameters did not match our above criteria on donor mass and system orbital period. Examples of this include systems resembling period-bouncers when analysing their spectrum (Inight et al. 2023b), optical light curve (Kimura et al. 2018), WD temperature (Pala et al. 2022), among others, even if their orbital period or donor mass could not be determined probably due to sparse or poor quality data.

The data sources we got most of the systems from are given here, in the order of their dates of publication: Littlefair et al. (2008), Patterson (2011), Otulakowska-Hypka et al. (2016), Kimura et al. (2018), Longstaff et al. (2019), Kato (2022), and Inight et al. (2023b). Henceforth, they are referred to as the “literature catalogs.” Additionally, we also considered systems that were studied individually in dedicated articles (see e.g., Savoury et al. 2012; Beuermann et al. 2021; Kawka et al. 2021; Wild et al. 2022 and Liu et al. 2023). This resulted in a literature catalog of 192 systems, by far the largest data base of period-bounce candidates studied to date.

The vast majority of the systems in our catalog, 133 out of 192 candidates, come from photometric studies of dwarf novae (both SU UMa and WZ Sge-type objects) specifically aimed at the study of superhumps in their superoutbursts (Otulakowska-Hypka et al. 2016, Kimura et al. 2018, Kato 2022). This type of photometric studies are specially relevant for us because they provide a superhump period for a large number of systems that can be used to obtain the mass ratio of the system (see Kato & Osaki 2013 for a comprehensive review of this method), and therefore yields the mass of the donor for a known WD mass.

The location of the 175 systems that have both orbital period and donor mass reported in the literature is presented in Fig. 1

with respect to the period-bounce area predicted from different tracks for the evolution of CVs by [Knigge et al. \(2011\)](#). The error bars presented in [Fig. 1](#) represent the range of donor masses measured for the systems if more than one value was found in the literature. All of the systems except for one, V1258 Cen, populate the area around the period minimum with a sizeable number of them located in the post-bounce area. V1258 Cen was proposed as a period-bouncer by [Pala et al. \(2022\)](#) due to its very low WD temperature, a key characteristic of this type of CV. However, detailed studies of V1258 Cen rule out this system as a period-bouncer, considering that it has an orbital period of 128 min ([McAllister et al. 2019](#)) and a donor mass of $0.198 \pm 0.029 M_{\odot}$ ([Savoury et al. 2012](#)) which are too large to belong to a system past the period minimum. We decided to keep this system in the catalog in order to compare its characteristics to other systems that are more likely to be period-bouncers. In particular, V1258 Cen may serve as a check to the scorecard that we define in [Sect. 4](#).

Our literature catalog contains 17 “bona fide” period-bouncers. These systems, shown in [Table 1](#), have been classified in the literature as such because they exhibit several key characteristics of period-bouncers in addition to a spectroscopic or photometric confirmation of a late-type donor. These confirmed period-bouncers will be used as a check to the scorecard. In [Col. 4](#) of [Table 1](#), we anticipate the final score for each of them according to the analysis we present in [Sect. 4](#). In our scoring system, a value of 100% is given to systems that have achieved the maximum possible score. Only two of the confirmed period-bouncers reach a 100% score, with a minimum score of 64%, which defines the lower boundary we applied to the full catalog, as described in [Sect. 4](#).

2.2. Literature values

We aimed to compile a catalog that has as much information on the period-bounce candidates as possible, including literature values on the following parameters: name, *Gaia*-DR3 ID, coordinates (J2000), orbital period (P_{orb}), temperature of the WD (T_{eff}), mass of the WD (M_{WD}), WD magnetism type, mass of the donor (M_{donor}), spectral type of the donor ($\text{SpT}_{\text{donor}}$), and the *Gaia*-DR3 distances given by [Bailer-Jones et al. \(2021\)](#). These parameters were drawn for the most part from the literature catalogs listed in [Sect. 2.1](#). In the case where no information was given on some parameters, or an updated value existed, we used additional references to supplement the catalog. A shortened version of our literature catalog is shown in [Table B.2](#) with a brief description of the columns in [Table B.1](#). In the following, we specify how we chose them from the literature.

Orbital period, available for 190 systems. The majority of orbital period values were derived through light curve analysis from optical surveys (see e.g., [Otulakowska-Hypka et al. 2016](#), [Kato 2022](#)), with a few of them coming from other methods like radial velocities from $H\alpha$ emission (see e.g., [Breedt et al. 2012](#), [Pala et al. 2018](#)) or X-ray light curves (see e.g., [Stelzer et al. 2017](#), [Muñoz-Giraldo et al. 2023](#)). In the specific instances where more than one source had a reported orbital period for a given system, the values were in all cases consistent with each other. In these cases, we chose to keep the value from the most recent derivation.

Donor mass, available for 175 systems. Considering that this parameter has the highest degree of uncertainty as it is rarely measured directly, when possible, we used two values for each

Table 1. Confirmed period-bouncers in the literature catalog.

Period-bouncer	Donor SpT	Ref	Score (%)
V379 Vir	L8 (S)	(1)	100
SDSS J15141+0744	L3 (P)	(2)	69
PM J12507+1549	M8 (P)	(2)	67
SDSS J10575+2759	L5 (P)	(3)	85
SDSS J14331+1011	L1 (S)	(4)	75
WZ Sge	L2 (S)	(5)	90
SDSS J10353+0551	L0 (P)	(6)	88
SMSS J16063–1000	L2 (P)	(7)	70
QZ Lib	T (S)	(8)	100
GD 552	BD (S)	(9)	79
MT Com	Very late (P)	(10)	76
V455 And	L2 (P)	(11)	88
V406 Vir	L3 (S)	(12)	64
BW Scl	T (S)	(13)	82
EZ Lyn	L2 (P)	(14)	94
CRTS J12222–3115	L0 (P)	(15)	77
V1108 Her	L1 (S)	(16)	82

Notes. We include the confirmation of a brown dwarf (BD) or late-type donor in the system through spectroscopy (S) or photometry (P) with the corresponding reference. The last column refers to the final score of each system defined in [Sect. 4](#) to estimate their likelihood of being a period-bouncer.

References. (1) [Farihi et al. \(2008\)](#), (2) [Breedt et al. \(2012\)](#), (3) [McAllister et al. \(2017\)](#), (4) [Santisteban et al. \(2016\)](#), (5) [Harrison \(2015\)](#), (6) [Southworth et al. \(2006\)](#), (7) [Kawka et al. \(2021\)](#), (8) [Pala et al. \(2018\)](#), (9) [Unda-Sanzana et al. \(2008\)](#), (10) [Patterson et al. \(2005b\)](#), (11) [Araujo-Betancor et al. \(2005\)](#), (12) [Pala et al. \(2019\)](#), (13) [Neustroev & Mäntynen \(2023\)](#), (14) [Zharikov et al. \(2013\)](#), (15) [Neustroev et al. \(2017\)](#), (16) [Ishioka et al. \(2007\)](#).

object, often determined from different methods. This allowed us to obtain a range for the expected mass of the secondary, illustrated by the error bars in [Fig. 1](#). The majority of the values come from using the WD mass together with the mass ratio ($q = M_{\text{donor}}/M_{\text{WD}}$) determined by either the superhump method ([Kato & Osaki 2013](#)) or the eclipse modeling method ([Savoury et al. 2011](#)). If no value for the WD mass was available, we used the value of $0.8 M_{\odot}$ determined by [Pala et al. \(2022\)](#) as the mean mass of WDs in CVs.

Spectral type of the donor, available for 38 systems. An accurate determination of the SpT is particularly relevant for the study of period-bouncers as the spectral type of the donor – together with its mass – is the parameter that is both the most important and the most difficult to determine precisely in a system with faint, very-low-mass donor. We used the classifications that preferably had a spectroscopic (see e.g., [Farihi et al. 2008](#); [Santisteban et al. 2016](#)) or, if not, a photometric confirmation (see e.g., [Amantayeva et al. 2021](#); [Kawka et al. 2021](#)).

White dwarf temperature, available for 80 systems. The majority of the values come from UV spectroscopy ([Pala et al. 2022](#)) and optical photometry ([Gentile Fusillo et al. 2021](#)). When no value was available from either of the methods, we considered temperatures derived from eclipse modeling or evolutionary status (see e.g., [McAllister et al. 2019](#); [Savoury et al. 2011](#)).

White dwarf mass, available for 47 systems. The majority of the values come from eclipse modeling (see e.g., [Savoury et al. 2011](#); [McAllister et al. 2019](#)) and UV spectroscopy

(Pala et al. 2022). When neither value was available, we considered masses derived from gravitational redshift (Neustroev & Mäntynen 2023) or optical spectroscopy (Muñoz-Giraldo et al. 2023).

White dwarf magnetism type, available for 94 systems. From broad sample studies (see e.g., Patterson 2011; Belloni et al. 2020; Pala et al. 2022), which commonly focus on non-magnetic CVs (as they are better understood and expected to follow standard evolution tracks), we categorized the systems present in these studies as non-magnetic. For magnetic CVs, we used individual references that in most cases identified the magnetic nature of the WD from the optical spectra (see, e.g., Breddt et al. 2012; Kawka et al. 2021).

2.3. Comments on short-period CVs

Considering that our catalog of short-period CVs has a large population of systems with information about key parameters in CV evolution, we have used this knowledge to comment on the observational characteristics of this type of systems.

2.3.1. Evolution tracks

The evolution of CVs, especially in the short-period regime, is still heavily debated, with theoretical models often clashing with results from observations. This has led to the development of several empirical (or semi-empirical) evolution tracks. Knigge et al. (2011) proposed a semi-empirical donor-based CV evolution track that, in the short-period regime, relies on a mechanism for angular momentum loss that is around 2.5 times stronger than pure gravitational radiation. The difference this change introduces can be easily observed in Fig. 1, where the revised model (orange line) is characterized by a period-bounce area associated with longer orbital periods when compared to the standard theoretical model (blue line). From the 175 systems in our catalog of period-bounce candidates that have a literature value for both the orbital period and the donor mass (shown in Fig. 1), we notice that short-period CVs seem to be located preferentially around the revised Knigge et al. (2011) evolution track. Only a few of the period-bounce candidates reach the short orbital periods associated with the period minimum of the standard evolution track, showing that for a given donor mass this track substantially underestimates the orbital period of the system. Previous CV studies have already noticed that a revised evolution model is necessary to reproduce observations (Littlefair et al. 2008; Pala et al. 2017, 2022; McAllister et al. 2019). However, it is important to note the considerable scatter in the distribution of the systems at or after the period minimum suggesting that the unique track of CV evolution might diverge around the bounce-back area. This scatter has been suggested to be related with the substantial range of masses that the WD may have (Howell et al. 2001) as the WD mass in CVs has been proven to not be constrained by the orbital period (Pala et al. 2022).

2.3.2. WD magnetism

The magnetism of the WD has been considered as a factor that may affect the evolution of CVs, leading to different evolution tracks depending on whether the WD is strongly magnetic or not (Gänsicke et al. 2009; Belloni et al. 2020). In magnetic CVs magnetic braking is expected to be reduced as the wind from the donor may be trapped within the magnetosphere of the WD, causing a difference in the rate of angular momentum loss between magnetic and non-magnetic CVs (Webbink

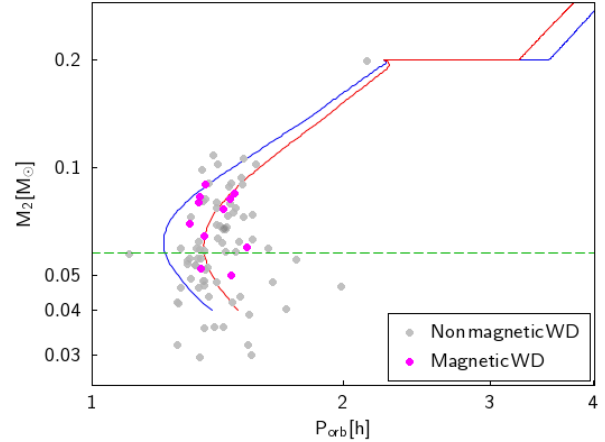


Fig. 2. Evolution for magnetic and non-magnetic CVs for the 94 systems in our literature catalog with information about the magnetism of the WD. Point of period reversal ($M_{\text{donor}} \approx 0.058 M_{\odot}$) is shown by the green dashed line. The two Knigge et al. (2011) CV evolution tracks from Fig. 1 are shown as reference.

& Wickramasinghe 2002). However, this difference is expected to be significantly reduced for short-period CVs as, in the standard model, gravitational radiation is believed to be the primary mechanism of angular momentum loss in the system with only a weak contribution by magnetic braking (Belloni et al. 2020; Schreiber et al. 2021). The distribution of the 94 systems in our catalog with information about the magnetism of the WD support this scenario, considering that we do not observe an evolution track in Fig. 2 being preferentially populated by either magnetic or non-magnetic CVs.

What we do observe from Fig. 2 is a clear difference between the pre- and post-bounce distribution of the magnetic and non-magnetic CVs. Only two out of the eleven magnetic systems are clearly past the point of period reversal ($M_{\text{donor}} \approx 0.058 M_{\odot}$; Knigge et al. 2011) corresponding to $\sim 20\%$ of this population. On the other hand 34 out of 82 non-magnetic systems are located in the period-bouncer area accounting for $\sim 40\%$ of this population. This implies that non-magnetic CVs are twice as likely to have evolved past the period minimum than magnetic CVs which might be taken as a hint for longer evolutionary times for magnetic CVs. This falls in line with expectations from simulations, where Belloni et al. (2020) observed a difference of $\sim 10\%$ between the number of period-bouncers in magnetic and non-magnetic population, with fewer magnetic CVs managing to become period-bouncers.

The lack of differentiation between evolution tracks of magnetic and non-magnetic CVs, as well as the overrepresentation of magnetic CVs in the pre-bounce area, could also be explained by the low number of observed short-period magnetic CVs, which leads to an incomplete representation of their evolution track. Magnetic CVs in our catalog account for 10% of the population, which is considerably fewer than the expected $\sim 30\%$ (Wickramasinghe & Ferrario 2000; Pretorius et al. 2013; Pala et al. 2020) obtained in previous CV population studies. Rather than showing the true picture of magnetic and non-magnetic short-period CVs, this result evidences a bias of our catalog towards non-magnetic systems. As already discussed in Sect. 2.1 the majority of our candidates are dwarf novae, a type of non-magnetic CV, selected from large photometric studies that provide both orbital period and mass of the systems. Such databases are not as readily available for magnetic systems making their inclusion into our catalog more challenging as we had to

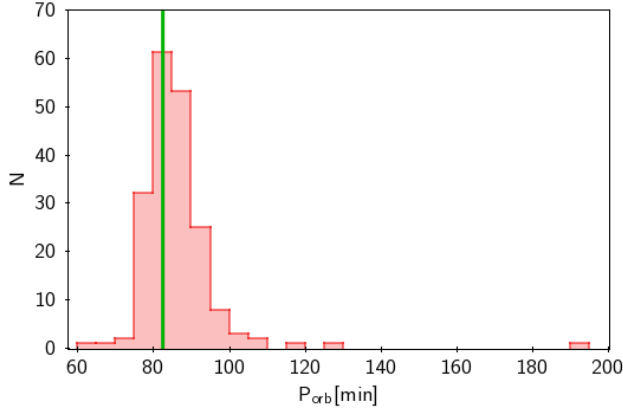


Fig. 3. Distribution of the orbital period for 190 systems in our literature catalog with values from the literature. The vertical green line is an estimate of P_{spike} using a Gaussian fit to the distribution of systems with orbital periods between 77 min and 87 min.

rely on individual papers that often did not include all the parameters required. This results in an underrepresentation of magnetic CVs in our catalog of period-bounce candidates.

2.3.3. Period spike and period minimum

The number density of CVs at a given period is inversely proportional to the rate at which the orbital period evolves (Kolb 1993; Kolb et al. 1998; Kolb & Baraffe 1999), making a pile-up or “spike” of systems at the period minimum an expected characteristic of CV evolution. This was observed for the first time by Gänsicke et al. (2009) using 137 CVs from SDSS. The period “spike” was established to be located in the orbital period range of 80 min to 86 min corresponding to a significant accumulation of CVs with $P_{\text{spike}} = 82.4 \pm 0.7$ min.

Figure 3 shows the orbital period distribution for 190 period-bounce candidates in our catalog with a literature value. The period “spike” is observed within the expected range of 80 min to 86 min. We estimated $P_{\text{spike}} = 82.4 \pm 2.7$ min (see green line in Fig. 3) following the description of McAllister et al. (2019) who used a Gaussian fit to the distribution of systems with orbital periods between 77 min and 87 min to obtain $P_{\text{spike}} = 82.7 \pm 0.4$ min. Both values are consistent with each other as well as with the Gänsicke et al. (2009) value. Our estimation for P_{spike} is also consistent with the 81.8 ± 0.9 min period minimum predicted by Knigge et al. (2011) in their revised donor track.

2.4. Distance estimates and limits

To determine the optical properties, and especially the distances, to the systems we performed a match between our literature catalog and the *Gaia*-DR3 catalog¹. Hereby we checked that the resulting match coincided with the *Gaia*-DR3 ID available in SIMBAD². Of the 192 systems in our catalog, 159 have available *Gaia*-DR3 data. 146 of our candidates have *Gaia* detections at different epochs meaning that they have an available parallax (Gaia Collaboration 2022) that can be used to estimate the distance to the systems.

¹ <https://cosmos.esa.int/web/gaia-users/archive>

² SIMBAD stands for Set of Identifications, Measurements and Bibliography for Astronomical Data, available at <http://simbad.cds.unistra.fr/simbad>

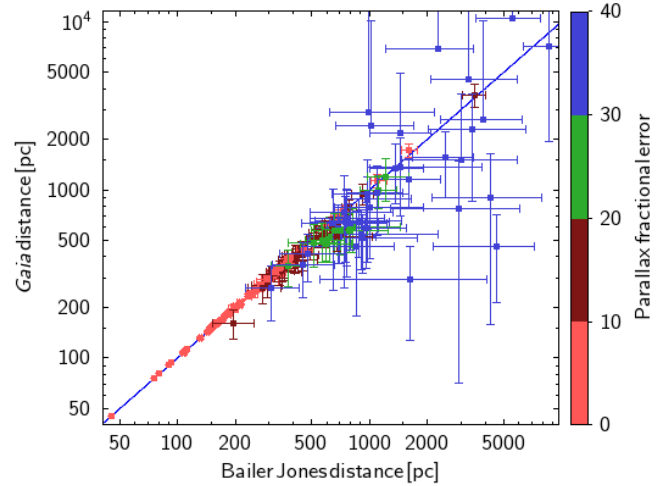


Fig. 4. Comparison between the distance obtained by Bailer-Jones et al. (2021) and by using the inverse of the parallax.

However, using parallaxes to estimate distances is not a trivial process considering that simply using the inverse of the parallax introduces biases in the distance estimate which affect especially systems with large fractional errors (Bailer-Jones 2015; Luri et al. 2018). As can be seen in Fig. 4, the more distant among the systems from our catalog present large fractional errors, which are greater than 20% for 49 of our period-bounce candidates. This is not an unexpected result considering that these systems have on average $G \sim 20.1$ mag, making their intrinsic faintness, which is characteristic of period-bouncers, the most likely cause for the large uncertainties of their parallaxes (see Fig. 7 from Lindgren et al. 2021).

In order to avoid the introduction of bias into our calculation, which would affect 49 of our candidates with a *Gaia* parallax value, we chose to use the distance estimates obtained by Bailer-Jones et al. (2021), specifically the geometric distance which takes a probabilistic approach that uses a prior constructed from a three-dimensional (3D) model of our Galaxy to estimate the distances (see Bailer-Jones 2015 for more information on this method). Figure 4 illustrates the difference between both methods used to estimate the distance, showing a significant disagreement for systems at large distances, where the distance from the parallax is underestimated with respect to the distances obtained by Bailer-Jones et al. (2021).

Having an accurate value for the distance is especially relevant for studies like ours considering that many system parameters depend on distance. One example is the magnetic CV EF Eri, which was considered a good period-bounce candidate because at an estimated distance of 111 pc the photometry suggested a brown dwarf donor in the system (Schwope & Christensen 2010). However, once the distance was revised to 160 pc (Bailer-Jones et al. 2021), this argument was not valid anymore disqualifying EF Eri from being a good period-bounce candidate. As EF Eri is included in our literature catalog, we used it similarly to V1258 Cen, namely, as a check of our score card (in Sect. 4).

3. Photometry

One possible discriminator between period-bouncers and other CVs regards the IR excess in the composite spectral energy distribution (SED) of the binary system. We include the IR excess

as one of the parameters that define our period-bouncer scorecard (Sect. 4). Therefore, we first had to construct the SEDs for the systems from our literature catalog of period-bounce candidates. We used the *Tool for Operations on Catalogues And Tables* (TOPCAT³; Taylor 2005) in order to handle our extensive catalog. TOPCAT is a JAVA-based interactive graphical viewer and editor for tabular data that facilitates the analysis and manipulation of source catalogues, specially the cross-match between catalogs.

We performed a cross-match in TOPCAT between our catalog and different photometric surveys covering a wide range of wavelengths from ultraviolet (UV) to infrared (IR). When performing the match with the algorithm “sky” we used the right ascension (RA) and declination (DEC) of each system in coordinates J2000, allowing for a match radius of 30”.

We used the following surveys with the latest catalog version available in TOPCAT: Galaxy Evolution Explorer (GALEX) general release GR6+7 (Bianchi et al. 2017); Sloan Digital Sky Survey (SDSS) data release DR16 (Ahumada et al. 2022); UKIRT Infrared Deep Sky Survey (UKIDSS) Large Area Survey data release DR9 (Lawrence et al. 2007); Two Micron All Sky Survey (2MASS) (Skrutskie et al. 2006); VISTA Hemisphere Survey (VHS) data release DR5 (McMahon et al. 2021); Wide-field Infrared Survey Explorer mission (WISE) (Cutri et al. 2021). After obtaining the best matches for each system using a 30” radius, we carried out a visual check to make sure that there were no other *Gaia* sources in the vicinity. We discarded those multiwavelength matches that most likely do not belong to our candidate, as they are associated with another *Gaia* source. This allowed us to obtain an optimal radius with which at least 94% of the correct matches were retrieved and at maximum one incorrect match: 4” for GALEX (103 correct associations), 4” for SDSS (82 correct associations), 1” for UKIDSS (27 correct associations), 2” for 2MASS (32 correct associations), 3” for VHS (46 correct associations), and 4” for WISE (94 correct associations). The multiwavelength photometry we collected this way can be found in the online version of our catalog, with the column descriptions listed in Table B.1.

Using the available photometry for each system, we constructed their individual spectral energy distributions (SEDs), ideally covering wavelengths from UV to IR. These SEDs are used in Sect. 4 to search for an IR excess and to evaluate whether it could be attributed to the presence of a very late-type donor.

4. Period-bouncer likelihood

We used the parameters of the candidates reported in the literature catalog to rate how likely a system is to be a period-bouncer. In this evaluation we considered ten parameters: spectral type of the donor, donor mass, orbital period, WD temperature, photometric colors (UV, optical and IR), optical variability, and IR excess. We compiled them into a scorecard in which we assigned different weights to the parameters depending on how relevant we judged them for confirming a candidate as a period-bouncer. A summary of the parameters and their respective scores is presented in Table 2 and is described in detail below.

4.1. Defining the scoring system

To analyze the likelihood of a system being a true period-bouncer, we assigned numerical scores to each individual parameter that we then combined into a final numerical score for

³ <https://www.star.bristol.ac.uk/mbt/topcat/>

Table 2. Scores assigned for the different parameters.

	Points	
Spectral type		
Spectroscopic	T/L donor	9
	M5 or later donor	5
	Very late donor	2
Non-spectroscopic	T/L donor	7
	M5 or later donor	3
	Very late donor	1
	Other	0
Donor mass		
	$M_{\text{donor}} \leq 0.058 M_{\odot}$	3
	$0.058 M_{\odot} < M_{\text{donor}} \leq 0.07 M_{\odot}$	1
	$M_{\text{donor}} > 0.07 M_{\odot}$	0
Orbital period		
$M_{\text{donor}} \leq 0.058 M_{\odot}$	For any P_{orb}	3
$M_{\text{donor}} \leq 0.07 M_{\odot}$	$P_{\text{orb}} \approx 80$ min	2
	$P_{\text{orb}} > 85$ min	1
	$P_{\text{orb}} > 90$ min	0
$M_{\text{donor}} > 0.07 M_{\odot}$	$P_{\text{orb}} \approx 80$ min	1
	$P_{\text{orb}} > 85$ min	0
No mass	$P_{\text{orb}} \leq 90$ min	1
	$P_{\text{orb}} > 90$ min	0
WD temperature		
	$T_{\text{eff}} \leq 12\,500$ K	3
	$12\,500 \text{ K} < T_{\text{eff}} \leq 14\,000$ K	1
	$T_{\text{eff}} > 14\,000$ K	0
<i>Gaia</i> variability		
	$G_{\text{var}} \leq 0.2$	3
	$0.2 < G_{\text{var}} \leq 0.3$	1
	$G_{\text{var}} > 0.3$	0
<i>Gaia</i> colors		
	In WD locus	3
	Broad WD locus	2
	Around main-sequence	0
SDSS colors		
$u - g \leq 0.5$	$u - g \geq 1.25(g - r) - 0.1$	3
	$u - g \geq 1.25(g - r) - 0.4$	1
	Other	0
GALEX colors		
	FUV-NUV ≥ 1	3
	$1 > \text{FUV-NUV} \geq 0.25$	1
	FUV-NUV < 0.25	0
IR Colors		
	T or L donor	3
	M donor	1
	Other	0
IR excess		
	No excess/at K-band or longer	3
	At J-band or longer	1
	Other	0

Notes. See text for full descriptions of each parameter.

each period-bounce candidate. The values obtained from all individual parameters considered in the scorecard (described in Sect. 4.2) and the final score are reported in Table 3. The maximum number of achievable score points is 36, corresponding to an object that has the highest score in all ten parameters, and hence a final score of 100%. However, a considerable number of candidates did not have enough data to be scored in all of the parameters making direct comparison between systems

Table 3. Scorecard for the period-bounce candidates in the literature catalog.

System	Parameters from Sect. 4										(%)
	SpT	M_{Donor}	P_{orb}	T_{WD}	G_{var}	<i>Gaia</i>	SDSS	UV	IR	Excess	
V379 Vir	9	3	3	3	3	3	3	3	3	3	100
SDSS J15141+0744	7	0	0	3	1	2	3	3	3	3	69
PM J12507+1549	3	0	0	3	3	3	3	3	3	3	67
⋮	⋮	⋮	⋮	⋮	⋮	⋮	⋮	⋮	⋮	⋮	⋮
EF Eri	0	0	1	3	3	3	–	1	0	1	36
V1258 Cen	0	0	0	3	0	0	–	–	0	1	13

Notes. See text for explanations on the different parameters and scores. The full table is available at the CDS.

difficult. To solve this problem, for each individual object, we re-define the final score of 100% as the maximum number of points that it would have received if it had the highest likelihood of being a period-bouncer in every parameter for which it has available data. We then calculated the percentage score as the ratio between the actual points the system has and its maximum achievable points. The objects without a percentage value in Table 3 only had available information for three or fewer parameters, which was not enough to characterize such an object as a period-bouncer.

4.2. Defining the scorecard parameters & their scores

We present in Table 2 a summary of the scoring system for each parameter and we illustrate this point system with Figs. 5 and 6. Here, the final score achieved by the systems is presented as a color scale and candidates without enough information to have received a final score are presented in yellow. To further enhance the clarity, areas of likelihood are marked by different shape styles: filled circles for high likelihood (three points), crosses for medium high likelihood (two points), triangles for medium likelihood (one point), and squares for low likelihood (zero points). The 17 confirmed period-bouncers from Table 1 are highlighted with black boxes. The assignment of the scores to each parameter is described here in descending order of relevance:

Spectral type of donor. This parameter holds the most weight as spectroscopic detection of a late-type donor in the system is the ultimate confirmation needed to confidently classify a system as a period-bouncer. Period-bouncers are characterized as being CVs with degenerate donors, composed by a WD and either a T dwarf or a L dwarf companion. We also take into account systems with a late M type (M5 or later) as this is indicative of a CV slightly before or just at the bouncing point (Knigge et al. 2011, Kirkpatrick & McCarthy Jr 1994). As was mentioned before, the spectral type of the donor is probably the hardest system parameter to determine in short-period faint CVs. Because of this we decided to award relatively high partial points to systems with a late-M type donor, especially considering that most of them were presented in the literature as a lower limit of the donor spectral type. Even though a spectroscopic detection is the preferred confirmation method for a late-type companion in the system, we also consider photometric data that suggests the presence of a late-type donor in the system.

Donor mass. A very low donor mass is indicative of a highly evolved CV even if there is no direct detection of the donor. In both their standard and revised evolution tracks for CVs, Knigge et al. (2011) obtained a post-bounce area for CVs

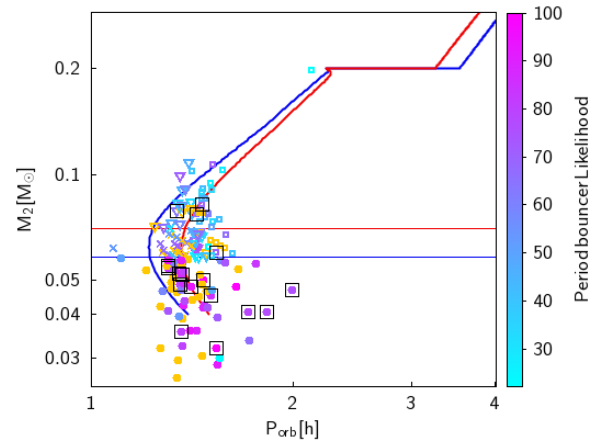


Fig. 5. Donor mass as a function of orbital period for 175 systems in our literature catalog with available values for both orbital period and donor mass. The two Knigge et al. (2011) CV evolution tracks from Fig. 1 are shown as reference. See Sect. 4.2 for explanation of markers and color scale, as well as the justification of the selection cut lines.

with a donor mass lower than $0.058 M_{\odot}$, this limit is shown as the blue horizontal line in Fig. 5. Systems with slightly higher donor masses (up to a donor mass of $0.07 M_{\odot}$ marked by the red line in Fig. 5) would be placed right in the bounce area, meaning that these systems are just within range of being called a potential period-bouncer. When assigning a score to this parameter we considered both possible values for the donor mass if available (see Sect. 2.2 for more information), giving each of the two donor mass values an individual score. For the overall score assigned to a system with two reported values for the donor mass, we considered the average of the two individual scores.

Orbital period. Near the period minimum the orbital period by itself is not a good diagnostic for evolution in CVs. To use P_{orb} as a parameter in the scorecard we consider also the score that each system was given for the donor mass. The clearest example of this are systems with very low donor masses ($\leq 0.058 M_{\odot}$; Knigge et al. 2011) for which the orbital period does not have significant incidence as they are all clearly located in the post-bounce area (see filled circles in Fig. 5). For all other systems, their scores are assigned judging their proximity to the observed period minimum of CVs (≈ 80 min; Gänsicke et al. 2009).

WD temperature. Considering that period-bouncers are the most evolved systems among CVs, a cool WD temperature (when not in outburst) is expected with temperatures $\leq 12\,500$ K (blue line in Fig. 6a; Pala et al. 2022). A temperature higher

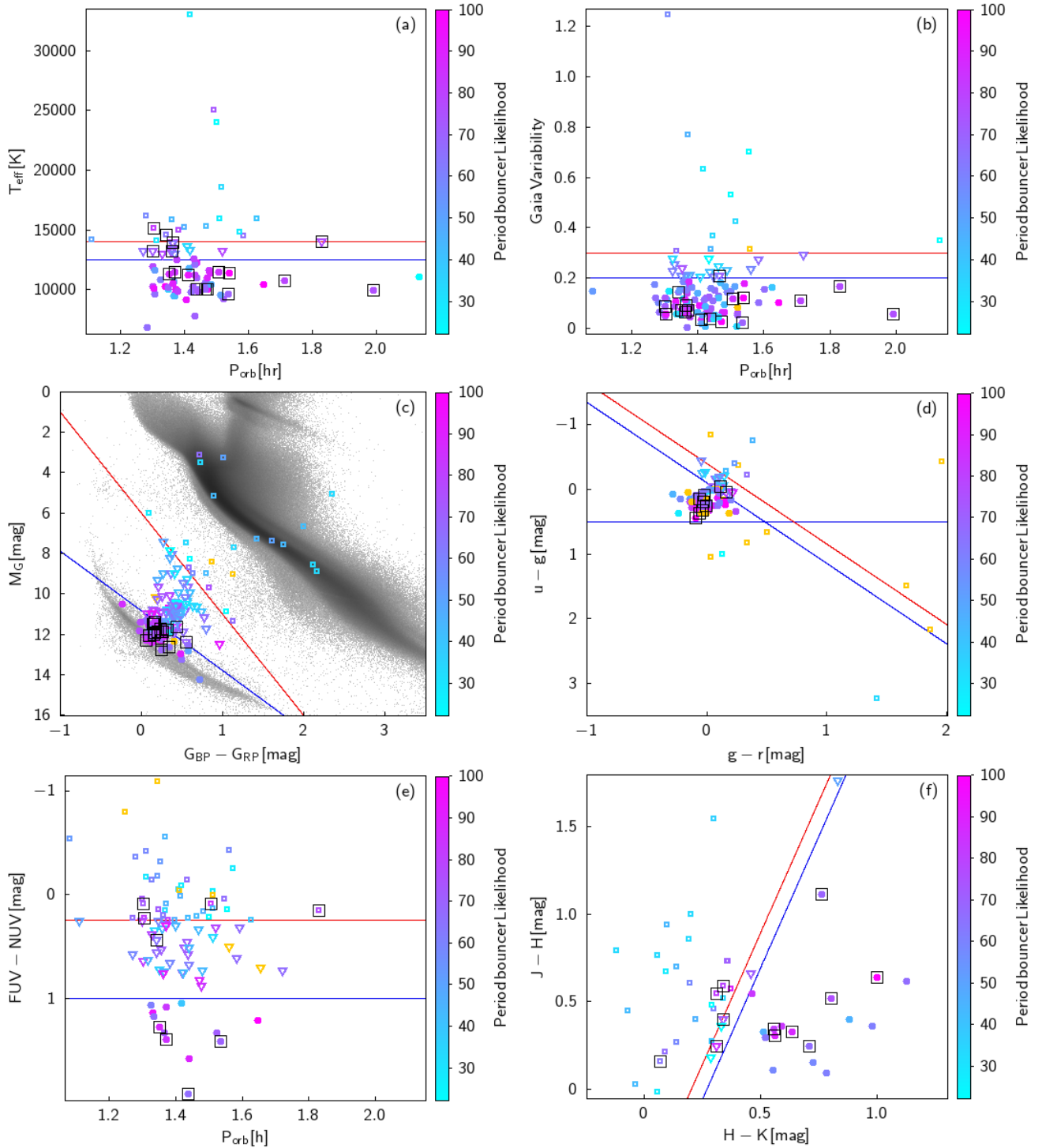


Fig. 6. Parameters used in the scorecard to rate the likelihood of a system of being a period-bouncer. See Sect. 4.2 for explanation of markers and color scale, as well as the justification of the selection cut lines. *Panel a:* WD effective temperature as a function of orbital period for 80 systems in our literature catalog with available information. *Panel b:* *Gaia* variability as a function of orbital period for 159 systems in our literature catalog with available information. *Panel c:* *Gaia* color–magnitude diagram showing the position of the 145 systems in our literature catalog with available information. The *Gaia*-DR3 sources with Bailer-Jones et al. (2021) distances and a parallax error of less than 1% of the parallax value are shown in gray as a reference. *Panel d:* SDSS color–color diagram showing the position of the 83 systems in our literature catalog with available information. *Panel e:* FUV-NUV color as a function of orbital period for 91 systems in our literature catalog with available information. *Panel f:* IR color–color diagram showing the position of the 45 systems in our literature catalog with available information.

than 14000K (red line in Fig. 6a) is no longer reflective of the cool temperature that WDs in period-bouncers are expected to exhibit, and in the rare cases when the measurement was carried out during an outburst, it should not be considered representative of the true WD temperature.

Gaia variability. As period-bouncers are in the last stage of CV evolution they are expected to be inactive systems with very large recurrence times for both outbursts and superoutbursts in the range of ~ 10000 days (Patterson 2011). For this reason, unless the period-bouncer is caught in a very rare burst episode, we expect a lack of optical variability. We used the *Gaia* G-band variability defined in Eq. (1) of Guidry et al. (2021), and defined the selection limits based on the results of Inight et al. (2023a) for WZ Sge-type CVs. According to their Fig. 36 the *Gaia* variability is ≤ 0.2 for 90% of the objects categorized as WZ Sge in their sample. This threshold is marked by the blue line in Fig. 6b. The *Gaia* variability of ≤ 0.3 , found for 98% of the objects categorized as WZ Sge in Inight et al. (2023a), are marked by the red line in Fig. 6b. Similar to the WD temperature, this parameter can be affected if the system was undergoing an outburst at the moment of the measurement. For this reason, we also calculated the G-band variability for *Gaia*-DR2 and assigned a score only for the candidates that received the same score points in *Gaia*-DR2 and *Gaia*-DR3, ensuring that their low or high variability is consistent through time and not reflective of sporadic events.

Gaia colors. In optical wavelengths the highly evolved secondary of period-bouncers is not expected to be observable. Therefore, these systems will appear almost identical to an isolated WD (Santisteban et al. 2018). We divided Fig. 6c in the following sectors: a WD locus limited by the blue line ($M_G \geq 2.95 \times (G_{BP} - G_{RP}) + 10.83$; Jiménez-Esteban et al. 2018), a more broadly defined WD locus limited by the blue and red lines ($M_G \geq 5 \times (G_{BP} - G_{RP}) + 6$; Gentile Fusillo et al. 2021), and an area around the main-sequence limited by the red line.

SDSS colors. We aimed to select areas where isolated WDs are expected to be found as the preferential location for period-bouncers. Inight et al. (2023a) plotted a color-color diagram for CVs with SDSS data and reliable photometry (see their Fig. 16) which shows the location of different CV types. We selected the areas where the majority of the Inight et al. (2023a) WZ Sge-type systems were found with 80% of them located between the blue horizontal line ($u - g \leq 0.5$) and the blue diagonal line ($u - g \geq 1.25(g - r) - 0.1$) represented by the filled circles in Fig. 6d. 90% of WZ Sge-type CVs are located between the blue horizontal line and the red diagonal line ($u - g \geq 1.25(g - r) - 0.4$) represented by the triangles in Fig. 6d.

UV colors. For systems in quiescence, GALEX colors are a sensitive probe of the effective WD temperature. Patterson (2011) plotted a sample of dwarf novae (see their Fig. 2) and determined areas where period-bounce candidates are most likely to be found. The area occupied exclusively by period bounce candidates is limited by $FUV - NUV \geq 1$ (blue line in Fig. 6e), while the area up to $FUV - NUV \geq 0.25$ (red line in Fig. 6e) is populated by period-bounce candidates and other types of CVs. Above the red line in Fig. 6e, Patterson (2011) found no period-bounce candidates.

IR colors. Several regions in the near-IR color-color diagram were identified by Littlefair et al. (2003) depending on the donor type that the population of CVs had (see their Fig. 2).

The right part of Fig. 6f is populated by systems with donors identified as either T-type (bottom right) or L-type (top right), while M-type donors are found towards the center (see triangles in Fig. 6f). Earlier type donors and other unidentified donor types are found towards the left part of Fig. 6f, limited by $J - H \leq 3(H - K) - 0.6$ (red line in Fig. 6f). Littlefair et al. (2003) selected systems with $J - H \leq 3(H - K) - 0.8$ (blue line in Fig. 6f) as candidates for having a degenerate donor.

IR excess. Throughout the evolution of a CV, the companion star loses so much mass that an originally early-type donor, with larger IR contributions, develops into a late-type or degenerate donor that barely contributes to the IR emission of the system. Due to the evolved nature of the secondary in period-bouncers, this very low mass donor is expected to appear as a very slight or no excess in the IR. We constructed SEDs for the 98 candidates that have enough photometric data, and compared them to WD models of spectral type DA with pure hydrogen atmosphere (Koester 2010) using the Virtual Observatory SED Analyzer (VOSA, Bayo et al. 2008). The main takeaway from this comparison is the wavelength at which the IR excess sets in. From the population of 17 confirmed period-bouncers we can establish that this type of CVs, especially the systems that have evolved back to periods larger than 90 min, presents IR excess (from the donor) that starts at relatively long wavelengths associated with the K-band or the WISE bands, if they present an excess at all. Systems close or at the bounce point will have an excess starting at shorter wavelengths associated with the J-band (Owens et al. 2023). Pre-bounce CVs are characterized by larger excess starting at shorter wavelengths (Girven et al. 2011). In Appendix C we show three SEDs that are representative of the different types of IR excess described above.

In Table 3, we show the scorecard ratings for the period-bounce candidates in the literature catalog. Overall, 49 of the 192 systems had information for only three or fewer parameters. As explained above, we did not assign a score to them and we exclude them from the following analysis.

Using the final scores of the 17 systems that have been confidently categorized as period-bouncers and have a spectroscopically confirmed late-type donor (see Table 1), we establish that an object has a high likelihood of being a period-bouncer if its final score is higher than 60%, considering that the confirmed period-bouncer with the lowest score is V406 Vir with 64%. We further divided the remaining candidates as having: medium-high likelihood (between 45% and 60%), medium-low likelihood (between 30% and 45%) and low likelihood (lower than 30%). With scores of 13% for V1258 Cen and 36% for EF Eri these systems are correctly categorized as objects with low and medium-low likelihood of being a period-bouncer respectively. This confirms that our scorecard is functioning satisfactorily as it not only returns high final scores for already confirmed period-bouncers, but it also returns low values for potential period-bouncers that have been previously discarded as good candidates. Additionally, this result shows that a system cannot be classified as a period-bouncer with only one parameter, and that a multiwavelength approach is necessary to produce a confident classification.

The differentiation of the candidates according to their final score results in 103 candidates with a high or medium high likelihood of being a period-bouncer, this subsample forms a group of strong period-bounce candidates. Considering that 17 of these candidates have already been confidently categorized as period-bouncers in the literature, this means that there are 86 strong period-bounce candidates present in the literature without having

been classified as such. Final confirmation of these systems as period-bouncers would greatly contribute to the sample size for this still under-represented class of CVs.

5. eROSITA data

To this day, eROSITA has carried out four full-sky surveys, named eRASS 1 to eRASS 4. Source catalogs from eRASS data are produced at Max Planck Institut für extraterrestrische Physik (MPE) in Garching, Germany, with the eROSITA Science Analysis Software System (eSASS) described by Brunner et al. (2022). These catalogs comprise all eRASS sources in the western half of the sky in terms of Galactic coordinates (Galactic longitude $l \geq 180^\circ$), which is the sky area with German data rights. Out of the 192 sources in the literature catalog 80 are located in the German eROSITA sky, eight of which are confirmed period-bouncers listed in Table 1.

5.1. X-ray parameters for the literature sample

To obtain the highest sensitivity for detecting the presumably faint sources from our literature catalog, we used the merged catalog eRASS:3 which was generated from summing data from the first three all-sky surveys. The latest version of the eRASS:3 catalog available to us in December 2023 was produced with the data processing version 020⁴. Source detection was performed in this catalog for a single eROSITA energy band, 0.2–2.3 keV.

We choose to work with this eRASS:3 catalog as this was the version used to compile a catalog of CV candidates, which we use as a point of comparison with our work. This catalog of CV candidates (Schwope et al., in prep.) was produced from matching eRASS:3 and *Gaia* sources using *NWAY*, a software for probabilistic cross-matching of catalogs (Salvato et al. 2018). It makes use of a Bayesian prior. This was trained on a set of 624 known CVs with well-known X-ray and optical properties. The optical properties used in characterizing the sample are brightness, color, coordinates, parallax, proper motion, and variability. The X-ray properties used are position and flux, and thus implicitly the optical to X-ray flux ratio. The *NWAY* match applied to eRASS:3 using the CV prior revealed 11 113 candidates with a CV probability $>50\%$, which are used in this paper for comparison to the period-bouncer sample. Full details on the construction of the eRASS:3 sample of CV candidates will be given by Schwope et al. (in prep.).

We corrected the coordinates of the period-bounce candidates in the literature catalog to the mean observing date of eRASS:3 using their *Gaia*-DR3 proper motions. We then matched them with the eRASS:3 catalog, allowing for a maximum separation of $30''$ and enforcing for the separation between optical and X-ray coordinates the condition $\text{sep}_{\text{ox}} < 3 \times \text{RADEC_ERR}$, where *RADEC_ERR* is the positional error of the X-ray coordinates in units of arcseconds. This way we found that 51 of the 80 period-bounce candidates from the literature catalog that are in the German eROSITA sky are detected in the eRASS:3 catalog.

This process was performed allowing for all possible matches within $30''$. However, each of the 51 detected period-bounce candidates had only one eRASS:3 match within that radius. We then carried out a visual inspection using *ESASky*⁵ in a $30''$ radius region around the X-ray source to assure that

there were no other potential optical counterparts. Out of the 51 period-bounce candidates detected in the eRASS:3 catalog, 45 have no other optical source closer to the eRASS X-ray position than our target and can therefore be confidently categorized as a correct match. Two additional eRASS:3 detections were confirmed as the correct match thanks to previous X-ray detections (*XMM-Newton* and *Chandra*) clearly associated with our targets. Out of the remaining four eRASS:3 detections, for one of them the visual inspection revealed an eRASS source at a sep_{ox} that is larger than the maximum of $3 \times \text{RADEC_ERR}$ that we allowed in the automatic match. For the last three there is another object closer to the eRASS source than our target, such that the X-ray source could not be securely associated with the period-bounce candidate. We present in Table A.1 the 51 sources with an eROSITA detection, where we do not report X-ray parameters for the four sources without a reliable association. These four sources are not considered in the following analysis.

We note in passing that of the 47 systems with safe eRASS:3 detection 31 are detected when using exclusively the first all-sky survey catalog eRASS 1⁶. The use of the combined catalog from three surveys, thus, constitutes a significant improvement, which is not unexpected as our targets are faint and substantially benefit from deeper X-ray exposure.

We proceeded with our analysis for the 47 systems with safe eRASS:3 detection, referred to as “eROSITA subsample”, which includes all eight confirmed period-bouncers located in the German eROSITA sky. In Table A.1 we present their X-ray parameters from eROSITA. In Cols. 2–5, we present the separation sep_{ox} , the detection likelihood value (the eRASS:3 catalog has a minimum detection likelihood of 5.0), the number of net source counts, and the count rate. The latter two refer to the 0.2–2.3 keV band used in eRASS:3. The catalogue uses a power-law model in order to obtain the flux from the count rate. This is not suitable for CVs which are characterized by a thermal plasma. Therefore, we converted the catalog flux from a power-law model to an APEC model using a conversion factor of 1.04 (see Muñoz-Giraldo et al. 2023 for a more detailed description). Using the APEC flux (Col. 6 of Table A.1) together with the *Gaia* DR3 distances given by Bailer-Jones et al. (2021) we obtained the X-ray luminosity, which was converted into bolometric X-ray luminosity ($L_{\text{x,bol}}$) in the band 0.1–12 keV (given in Col. 7) by multiplication with a factor of 1.6 (Muñoz-Giraldo et al. 2023). We then calculated the mass accretion rate for each system taking into consideration if it has a reported value for the WD mass (see Table B.2). For those systems with a reported WD mass we used this value together with the WD radius obtained with the Nauenberg (1972) mass-radius relation. For the systems without a WD mass we used $0.8 M_{\odot}$, which is the mean mass of WDs in CVs (Pala et al. 2022), and the corresponding radius of 7×10^8 cm from the Nauenberg (1972) mass-radius relation. Only one system, TCP 1537, does not have a reported *Gaia* DR3 distance, which prevents us from calculating an X-ray luminosity and mass accretion rate for this period-bounce candidate.

5.2. X-ray parameter space of period-bouncers

Using the final scores assigned to the confirmed period-bouncers (see Table 3) together with the X-ray results from eROSITA (see Table A.1) we can establish two new parameters, X-ray-to-optical flux ratio ($F_{\text{x}}/F_{\text{opt}}$) and bolometric X-ray luminosity, that will aid in the future identification of highly likely

⁴ The source catalog used in our work is all_s3_SourceCat1B_221007_poscorr_mpe_clean.fits (for eRASS:3).

⁵ <https://sky.esa.int/>

⁶ The source catalog used in our work is the 020 version of all_e1_SourceCat3B_221031_poscorr_mpe_clean.fits (for eRASS1).

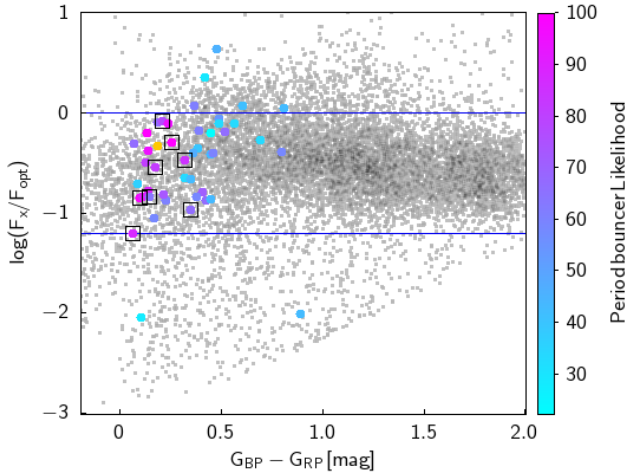


Fig. 7. X-ray-to-optical flux ratio as a function of *Gaia* colors showing the position of the 46 systems in our literature catalog found in eRASS:3. We show in grey as reference a population of CV candidates found in eRASS:3.

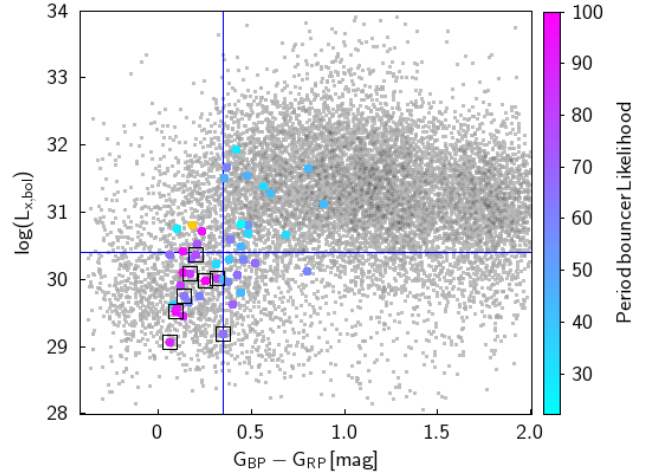


Fig. 8. Bolometric X-ray luminosity as a function of *Gaia* colors showing the position of the 46 systems in our literature catalog found in eRASS:3. We show in grey as reference a population of CV candidates found in eRASS:3. See text for the justification of the selection cut lines.

period-bounce candidates from eROSITA data. A possible third new parameter, the mass accretion rate (\dot{M}_{acc}), could be used for cases with known WD mass, considering that using the mean WD mass and radius gives a distribution indistinguishable from the one obtained using the X-ray luminosity. As less than half of the period-bounce candidates with eROSITA data have an individually determined WD mass, \dot{M}_{acc} would not yield additional information on the sample and we do not use it to define selection cuts for period-bouncers.

In Figs. 7 and 8, we have placed the eROSITA subsample in two diagrams combining X-ray and optical data. We compare the position of this sample with the overall catalog of eROSITA selected CV candidates (Schwope et al., in prep) introduced in Sect. 5.1. The eROSITA detected confirmed period-bouncers from Table 1 are highlighted using black boxes.

Figure 7 presents the X-ray-to-optical flux ratio versus *Gaia* color, where the majority of both the overall eROSITA CV candidate population and our eROSITA subsample display $-1 \leq \log(F_x/F_{\text{opt}}) \leq 0$. This is to be expected in systems with low mass transfer rate including different CV types such as dwarf novae, polars and intermediate polars, which make up the bulk of the observed CV population. Even though this parameter is not meant to be used on its own to determine new period-bounce candidates, it serves as an important check that the system does not display very small values of X-ray-to-optical flux ratio, that would indicate a system with a very high mass transfer rate (e.g., nova-like variables) and thus disqualify the system from being a period-bouncer.

Figure 8 shows the bolometric X-ray luminosity versus *Gaia* color, where we identify a region preferably dominated by highly likely period-bouncers. In this diagram, the highly likely period-bouncers from the eROSITA subsample are considerably differentiated from the overall eROSITA CV candidate population displaying a lower bolometric X-ray luminosity of $L_{x,\text{bol}} \approx 10^{30} \text{ erg s}^{-1}$. Together with their relatively blue *Gaia* color $L_{x,\text{bol}}$ proves to be a powerful tool for identifying new period-bounce candidates from eROSITA data, as, compared to most other CV candidates, probable period-bouncers present both bluer colors (because they are WD dominated) and lower X-ray luminosities (because of their low mass accretion rate). Applying

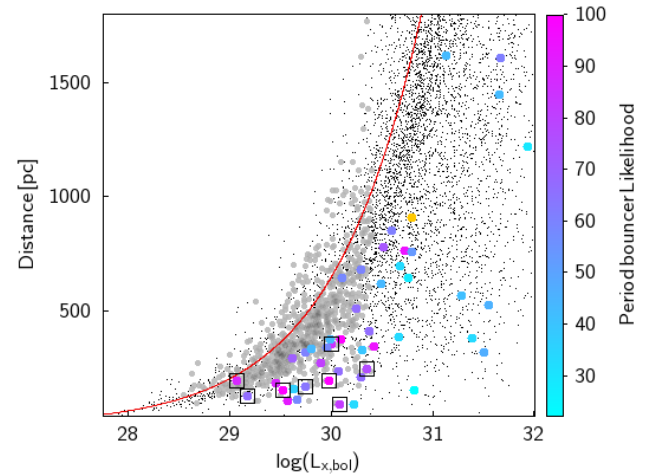


Fig. 9. Distance from Bailer-Jones et al. (2021) versus bolometric X-ray luminosity showing the position of the 46 systems in our literature catalog detected in eRASS:3 with respect to the average eRASS:3 sensitivity limit marked by the red line. We show in black the population of CV candidates found in eRASS:3, and in grey a subsample of 775 CV candidates of them that we have selected as period-bounce candidates.

selection cuts based on the upper limits for the X-ray luminosity ($\log(L_{x,\text{bol}}) \leq 30.4$ [erg s^{-1}]) and *Gaia* color ($G_{\text{BP}} - G_{\text{RP}} \leq 0.35$) exhibited by systems from our catalog that have already been confirmed as being period-bouncers (see lower left rectangle in Fig. 8) separates 971 CV candidates from the rest of the overall eROSITA CV candidate population. Additionally, we checked that they are low mass transfer rate systems using the X-ray-to-optical flux ratio ($-1.21 \leq \log(F_x/F_{\text{opt}}) \leq 0$) exhibited by the confirmed period-bouncers in our catalog, finding that 775 of them fulfill both X-ray criteria defined for confirmed period-bouncers from eROSITA.

We show in Fig. 9 the relationship between X-ray luminosity and distance. The red line gives the lower limit for the eRASS:3 luminosity calculated for the limiting X-ray flux of $2 \times 10^{-14} \text{ erg cm}^{-2} \text{ s}^{-1}$ (Muñoz-Giraldo et al. 2023). Two things

are immediately apparent from Fig. 9. First, at a given luminosity period-bounce candidates tend to have smaller distances than the majority of CV candidates. This is expected as period-bouncers are intrinsically faint. Secondly, for a given distance, our period-bounce candidates are among the sources with the highest X-ray luminosity, probably due to (non-X-ray) selection effects of the literature catalogs they were pulled from. This means that there might be a significant population of period-bouncers at short distances with X-ray luminosities lower than the period-bounce candidates identified in this work but higher than the eRASS:3 limit. These systems have yet to be singled out and studied.

In order to select this missing population of period-bouncers in eROSITA data we should look into the 775 selected CV candidates that are systems with low mass transfer rates as well as fulfill the selection cuts shown in Fig. 8. These systems are shown as grey dots in Fig. 9 located fairly close to the luminosity limit in eRASS:3 for period-bouncers (see red line in Fig. 9).

6. Conclusions

One of our main goals in this work has been to establish the X-ray properties of the class of period-bounce CVs, specifically using new data from the eROSITA all-sky surveys. We explored the eRASS:3 catalog with a sample of 17 confirmed period-bouncers and 175 additional candidates that we compiled from the literature. We established two selection cuts based on the X-ray-to-optical flux ratio and the X-ray luminosity observed from the already confirmed period-bouncers. We found seven candidates with high likelihood of being a period-bounce system according to our multiparameter scorecard within these X-ray selection cuts (see Cols. 10–12 in Table A.1). This means that they appear very similar to known period-bouncers in our multiwavelength study including X-rays. On this basis, we can confidently suggest seven systems in our literature catalog as new period-bouncers. Four of these seven systems (LP 731-60, EG Cnc, SDSS J12160+0520, and HV Vir) had already been suggested as potential period-bouncers, however, a confident classification was not evident to us from the literature. The remaining three systems (1RXS J02323-3718, PM J12192+2049, and CRTS J10441+2113) were only mentioned in the literature as WZ Sge-type objects. None of the new period-bouncers have a detected late-type donor mainly due to the lack of in-depth studies of these sources. Future detailed spectroscopic studies will shed more light on their status as period-bouncers.

This new addition of confirmed period-bouncers represents an increase in the population of some 40%, bringing the number of this elusive class of CVs to 24 and establishing eROSITA as a powerful tool for the characterization and identification of period-bouncers. However, despite this substantial increase of the known population of period-bounce CVs, it still remains well below the numbers expected by theoretical models. We foresee that a further exploitation of eROSITA data might boost the population number to the predicted levels, especially considering that the X-ray faint period-bounce population has yet to be adequately discovered.

In an exploratory study, we tentatively identified a 500 pc volume-limited sample of potential period-bouncers from the overall CV population presented in a new eROSITA-selected catalog (Schwope et al., in prep.). The 500 pc boundary is motivated by the limitation on the accuracy of distance measurements that can be achieved with *Gaia* for faint objects (see Fig. 4) and the eRASS sensitivity limit (Fig. 9).

First, in our catalog of period-bounce candidates, 77 of the 81 systems within 500 pc have a fractional distance error smaller

than 20%, including all 17 confirmed period-bouncers from Table 1 and all 7 new eROSITA-confirmed period-bouncers. Secondly, when we take the mean X-ray luminosity of the 8 confirmed period bouncers detected in eRASS:3 ($\log(L_{x,\text{bol}}) = 29.74$ [erg s^{-1}]) as a typical X-ray luminosity for this class of objects the average eRASS:3 flux limit yields a distance limit of 480 pc. Thus, a rough distance limit of 500 pc seems appropriate for a meaningful period-bouncer population study.

Within 500 pc, the population of CV candidates from eRASS:3 is made up of 1770 systems, of which 543 have been selected as potential period-bounce candidates using our eROSITA X-ray selection cuts, representing 31% of the overall CV candidate population. Even though this result would only place the population of period-bouncers towards the lower end of the expected by evolutionary CV models (40% to 80%), it would be an encouraging indicator that more period-bouncers have not been discovered mainly due to observational constraints rather than overestimation from CV evolution models.

In the near future, we will seek to systematically uncover the 500 pc sample of period-bouncers. We aim to carry out an in-depth study of the 81 candidates from the catalog presented in this work and the 543 new eROSITA CV candidates we selected as potential period-bouncers using the X-ray selection cuts.

The confirmation or rejection of the systems from this sample will provide a benchmark for population studies of CVs around the period-bounce region.

Acknowledgements. We thank an anonymous referee for reviewing the original manuscript and giving helpful comments and useful advice. Daniela Muñoz-Giraldo acknowledges financial support from Deutsche Forschungsgemeinschaft (DFG) under grant number STE 1068/6-1. This work is based on data from eROSITA, the primary instrument aboard SRG, a joint Russian-German science mission supported by the Russian Space Agency (Roskosmos), in the interests of the Russian Academy of Sciences represented by its Space Research Institute (IKI), and the Deutsches Zentrum für Luft- und Raumfahrt (DLR). The SRG spacecraft was built by Lavochkin Association (NPOL) and its subcontractors, and is operated by NPOL with support from the Max Planck Institute for Extraterrestrial Physics (MPE). The development and construction of the eROSITA X-ray instrument was led by MPE, with contributions from the Dr. Karl Remis Observatory Bamberg and ECAP (FAU Erlangen-Nürnberg), the University of Hamburg Observatory, the Leibniz Institute for Astrophysics Potsdam (AIP), and the Institute for Astronomy and Astrophysics of the University of Tübingen, with the support of DLR and the Max Planck Society. The Argelander Institute for Astronomy of the University of Bonn and the Ludwig Maximilians Universität München also participated in the science preparation for ero. The eROSITA data shown here were processed using the eSASS/NRTA software system developed by the German eROSITA consortium. This work has made use of data from the European Space Agency (ESA) mission *Gaia* (<https://www.cosmos.esa.int/gaia>), processed by the *Gaia* Data Processing and Analysis Consortium (DPAC, <https://www.cosmos.esa.int/web/gaia/dpac/consortium>). Funding for the DPAC has been provided by national institutions, in particular the institutions participating in the *Gaia* Multilateral Agreement. This publication makes use of VOSA, developed under the Spanish Virtual Observatory (<https://svo.cab.inta-csic.es>) project funded by MCIN/AEI/10.13039/501100011033/ through grant PID2020-112949GB-I00. VOSA has been partially updated by using funding from the European Union's Horizon 2020 Research and Innovation Programme, under Grant Agreement n° 776403 (EXOPLANETS-A).

References

- Ahumada, R., Allende Prieto, C., Almeida, A., et al. 2022, *VizieR On line Data Catalog*: V/154
 Amantayeva, A., Zharikov, S., Page, K., et al. 2021, *ApJ*, **918**, 58
 Araujo-Betancor, S., Gänsicke, B., Hagen, H.-J., et al. 2005, *A&A*, **430**, 629
 Audard, M., Osten, R., Brown, A., et al. 2007, *A&A*, **471**, L63
 Bailer-Jones, C. A. 2015, *PASP*, **127**, 994
 Bailer-Jones, C. A. L., Rybizki, J., Fouesneau, M., Demleitner, M., & Andrae, R. 2021, *AJ*, **161**, 147
 Bayo, A., Rodrigo, C., Barrado Y Navascués, D., et al. 2008, *A&A*, **492**, 277
 Belloni, D., Schreiber, M. R., Pala, A. F., et al. 2020, *MNRAS*, **491**, 5717

- Beuermann, K., Burwitz, V., Reinsch, K., Schwöpe, A., & Thomas, H.-C. 2021, *A&A*, **645**, A56
- Bianchi, L., Shiao, B., & Thilker, D. 2017, *ApJS*, **230**, 24
- Breedt, E., Gänsicke, B. T., Girven, J., et al. 2012, *MNRAS*, **423**, 1437
- Brunner, H., Liu, T., Lamer, G., et al. 2022, *A&A*, **661**, A1
- Burleigh, M. R., Marsh, T., Gänsicke, B., et al. 2006, *MNRAS*, **373**, 1416
- Cropper, M. 1990, *Space Sci. Rev.*, **54**, 195
- Cutri, R. M., Wright, E. L., Conrow, T., et al. 2021, VizieR Online Data Catalog: *II/328*
- De Luca, A., Stelzer, B., Burgasser, A. J., et al. 2020, *A&A*, **634**, A13
- Echevarría, J., Zharikov, S., & Mora Zamora, I. 2023, *MNRAS*, **526**, 5110
- Farihi, J., Burleigh, M., & Hoard, D. 2008, *ApJ*, **674**, 421
- Gaia Collaboration 2022, VizieR Online Data Catalog: *I/355*
- Gänsicke, B., Dillon, M., Southworth, J., et al. 2009, *MNRAS*, **397**, 2170
- Gentile Fusillo, N., Tremblay, P., Cukanovaite, E., et al. 2021, *MNRAS*, **508**, 3877
- Girven, J., Gänsicke, B., Steeghs, D., & Koester, D. 2011, *MNRAS*, **417**, 1210
- Goliäsch, J., & Nelson, L. 2015, *ApJ*, **809**, 80
- Guidry, J. A., Vanderbosch, Z. P., Hermes, J., et al. 2021, *ApJ*, **912**, 125
- Harrison, T. E. 2015, *ApJ*, **816**, 4
- Howell, S. B., Nelson, L. A., & Rappaport, S. 2001, *ApJ*, **550**, 897
- Howell, S. B., Walter, F. M., Harrison, T. E., et al. 2006, *ApJ*, **652**, 709
- Inight, K., Gänsicke, B. T., Breedt, E., et al. 2021, *MNRAS*, **504**, 2420
- Inight, K., Gänsicke, B. T., Breedt, E., et al. 2023a, *MNRAS*, **524**, 4867
- Inight, K., Gänsicke, B. T., Schwöpe, A., et al. 2023b, *MNRAS*, **525**, 3597
- Ishioaka, R., Sekiguchi, K., & Maehara, H. 2007, *PASJ*, **59**, 929
- Jiménez-Esteban, F., Torres, S., Rebassa-Mansergas, A., et al. 2018, *MNRAS*, **480**, 4505
- Kato, T. 2015, *PASJ*, **67**, 108
- Kato, T. 2022, arXiv e-prints [arXiv:2201.02945]
- Kato, T., & Osaki, Y. 2013, *PASJ*, **65**, 115
- Kato, T., Imada, A., Uemura, M., et al. 2009, *PASJ*, **61**, S395
- Kawka, A., Vennes, S., Ferrario, L., et al. 2021, *MNRAS*, **507**, L30
- Kimura, M., Isogai, K., Kato, T., et al. 2018, *PASJ*, **70**, 47
- King, A. 1988, *Q. J. Roy. Astron. Soc.*, **29**, 1
- Kirkpatrick, J. D., & McCarthy Jr, D. W. 1994, *AJ*, **107**, 333
- Knigge, C. 2006, *MNRAS*, **373**, 484
- Knigge, C., Baraffe, I., & Patterson, J. 2011, *ApJS*, **194**, 28
- Koester, D. 2010, *Mem. Soc. Astron. Italiana*, **81**, 921
- Kolb, U. 1993, *A&A*, **271**, 149
- Kolb, U., & Baraffe, I. 1999, *MNRAS*, **309**, 1034
- Kolb, U., King, A., & Ritter, H. 1998, *MNRAS*, **298**, L29
- Kruckow, M. U., Neunteufel, P. G., Di Stefano, R., Gao, Y., & Kobayashi, C. 2021, *ApJ*, **920**, 86
- Lawrence, A., Warren, S., Almaini, O., et al. 2007, *MNRAS*, **379**, 1599
- Lindegren, L., Klioner, S., Hernández, J., et al. 2021, *A&A*, **649**, A2
- Littlefair, S., Dhillon, V., & Martin, E. 2003, *MNRAS*, **340**, 264
- Littlefair, S., Dhillon, V., Marsh, T., et al. 2008, *MNRAS*, **388**, 1582
- Liu, Y., Hwang, H.-C., Zakamska, N. L., & Thorstensen, J. R. 2023, *MNRAS*, **522**, 2719
- Longstaff, E., Casewell, S., Wynn, G., et al. 2019, *MNRAS*, **484**, 2566
- Luri, X., Brown, A., Sarro, L., et al. 2018, *A&A*, **616**, A9
- McAllister, M., Littlefair, S., Dhillon, V., et al. 2017, *MNRAS*, **467**, 1024
- McAllister, M., Littlefair, S., Parsons, S., et al. 2019, *MNRAS*, **486**, 5535
- McMahon, R. G., Banerji, M., Gonzalez, E., et al. 2021, VizieR Online Data Catalog: *II/367*
- Mestel, L. 1968, *MNRAS*, **138**, 359
- Meyer, F., & Meyer-Hofmeister, E. 1984, *A&A*, **132**, 143
- Muñoz-Giraldo, D., Stelzer, B., de Martino, D., & Schwöpe, A. 2023, *A&A*, **676**, A7
- Nauenberg, M. 1972, *ApJ*, **175**, 417
- Neustroev, V. V., & Mäntynen, I. 2023, *MNRAS*, **523**, 6114
- Neustroev, V., Marsh, T. R., Zharikov, S., et al. 2017, *MNRAS*, **467**, 597
- Osaki, Y. 1989, *PASJ*, **41**, 1005
- Otulakowska-Hypka, M., Olech, A., & Patterson, J. 2016, *MNRAS*, **460**, 2526
- Owens, D., Xu, S., Manjavacas, E., et al. 2023, *AJ*, **166**, 5
- Paczynski, B. 1976, in *IAU Symp.*, 73 (Cambridge University Press), 75
- Paczynski, B., & Sienkiewicz, R. 1983, *ApJ*, **268**, 825
- Pala, A. F., Gänsicke, B., Townsley, D., et al. 2017, *MNRAS*, **466**, 2855
- Pala, A. F., Schmidtobreick, L., Tappert, C., Gänsicke, B. T., & Mehner, A. 2018, *MNRAS*, **481**, 2523
- Pala, A. F., Gänsicke, B. T., Marsh, T., et al. 2019, *MNRAS*, **483**, 1080
- Pala, A., Gänsicke, B., Breedt, E., et al. 2020, *MNRAS*, **494**, 3799
- Pala, A., Gänsicke, B., Belloni, D., et al. 2022, *MNRAS*, **510**, 6110
- Patterson, J. 1994, *PASP*, **106**, 209
- Patterson, J. 1998, *PASP*, **110**, 1132
- Patterson, J. 2011, *MNRAS*, **411**, 2695
- Patterson, J., Masi, G., Richmond, M. W., et al. 2002, *PASP*, **114**, 721
- Patterson, J., Kemp, J., Harvey, D. A., et al. 2005a, *PASP*, **117**, 1204
- Patterson, J., Thorstensen, J. R., & Kemp, J. 2005b, *PASP*, **117**, 427
- Politano, M. 1996, *ApJ*, **465**, 338
- Predehl, P., Andritschke, R., Arefiev, V., et al. 2021, *A&A*, **647**, A1
- Pretorius, M. L., Knigge, C., & Schwöpe, A. D. 2013, *MNRAS*, **432**, 570
- Rappaport, S., Joss, P. C., & Webbink, R. F. 1982, *ApJ*, **254**, 616
- Ritter, H. 1991, in *High Energy Astrophysics: Compact Stars and Active Galaxies (Proc. 3rd Chinese Academy of Sciences and Max-Planck-Society Workshop, Huangshan, China, 1990)*, ed. Q. B. Li (Singapore: World Scientific), 107
- Salvato, M., Buchner, J., Budavári, T., et al. 2018, *MNRAS*, **473**, 4937
- Santisteban, J. V. H., Knigge, C., Littlefair, S. P., et al. 2016, *Nature*, **533**, 366
- Santisteban, J. H., Knigge, C., Pretorius, M., Sullivan, M., & Warner, B. 2018, *MNRAS*, **473**, 3241
- Savourey, C., Littlefair, S., Dhillon, V., et al. 2011, *MNRAS*, **415**, 2025
- Savourey, C., Littlefair, S. P., Marsh, T. R., et al. 2012, *MNRAS*, **422**, 469
- Schmidt, G. D., Szkody, P., Silvestri, N. M., et al. 2005, *ApJ*, **630**, L173
- Schreiber, M., Zorotovic, M., & Wijnen, T. 2016, *MNRAS*, **455**, L16
- Schreiber, M. R., Belloni, D., Gänsicke, B. T., Parsons, S. G., & Zorotovic, M. 2021, *Nat. Astron.*, **5**, 648
- Schreiber, M. R., Belloni, D., & van Roestel, J. 2023, *A&A*, **679**, A8
- Schwöpe, A., & Christensen, L. 2010, *A&A*, **514**, A89
- Schwöpe, A., Worpel, H., & Traulsen, I. 2021, *A&A*, **646**, A181
- Skrutskie, M., Cutri, R., Stiening, R., et al. 2006, *AJ*, **131**, 1163
- Southworth, J., Gänsicke, B., Marsh, T., et al. 2006, *MNRAS*, **373**, 687
- Spruit, H. C., & Ritter, H. 1983, *A&A*, **124**, 267
- Stelzer, B., de Martino, D., Casewell, S., Wynn, G., & Roy, M. 2017, *A&A*, **598**, L6
- Sunyaev, R., Arefiev, V., Babyshkin, V., et al. 2021, *A&A*, **656**, A132
- Taylor, M. B. 2005, in *Astronomical Data Analysis Software and Systems XIV*, 347, 29
- Unda-Sanzana, E., Marsh, T., Gänsicke, B. T., et al. 2008, *MNRAS*, **388**, 889
- Uemura, M., Kato, T., Nogami, D., & Ohsugi, T. 2010, *PASJ*, **62**, 613
- Verbunt, F., & Zwaan, C. 1981, *A&A*, **100**, L7
- Vogt, N. 1980, *A&A*, **88**, 66
- Warner, B. 1995, *Cataclysmic Variable Stars*, 28 (Cambridge University Press)
- Webbink, R., & Wickramasinghe, D. 2002, *MNRAS*, **335**, 1
- Whitehurst, R. 1988, *MNRAS*, **232**, 35
- Wickramasinghe, D. T. 1988, in *Polarized Radiation of Circumstellar Origin*, eds. G. V. Coyne, A. M. Magalhaes, A. F. Moffat, R. E. Schulte-Ladbeck, & S. Tapia, 199
- Wickramasinghe, D., & Ferrario, L. 2000, *PASP*, **112**, 873
- Wijnen, T., Zorotovic, M., & Schreiber, M. 2015, *A&A*, **577**, A143
- Wild, J., Littlefair, S., Ashley, R., et al. 2022, *MNRAS*, **509**, 5086
- Zharikov, S., Tovmassian, G., Aviles, A., et al. 2013, *A&A*, **549**, A77
- Zorotovic, M., Schreiber, M. R., & Gänsicke, B. 2011, *A&A*, **536**, A42

Appendix A: X-ray parameters for eROSITA detected systems

Table A.1 gives the X-ray parameters from the eROSITA merged catalog eRASS:3 for the detected sources from the literature catalog, known as the eROSITA subsample, including the distance used to calculate the X-ray luminosity and the final period-bouncer score. Values are given for the eROSITA single band (0.2-2.3 keV).

Table A.1. X-ray parameters for the sources in the eROSITA subsample. We use a checkmark to show which sources fulfill the selection cuts presented in Sect. 5.2 and displayed as blue lines in Figs. 7 and 8.

Name	Detection likelihood	sep _{90%} ["]	Counts [cts]	Count rate [cts/s]	Flux (APEC) × 10 ⁻¹³ [erg cm ⁻² s ⁻¹]	Distance [pc]	X-ray luminosity ¹ log(L _{bol}) [erg s ⁻¹]	M _{acc} × 10 ⁻¹⁴ [M _⊙ yr ⁻¹]	Selection cuts	Period-bouncer final score [%]
V379 Vir [†]	44.5	2.2	30.1±6.3	0.08±0.02	0.75±0.16	153	29.5	2.2	✓	100
PM J12507+1549 [†]	19.9	2.9	16.5±4.9	0.05±0.02	0.46±0.14	131	29.2	1.0	✓	67
EF Eri	100.3	6.2	55.0±8.2	0.10±0.01	0.86±0.13	160	29.6	2.7	✓	36
SDSS J10575+2759 [†]	15.5	6.0	10.7±3.7	0.05±0.02	0.42±0.14	355	30.0	6.5	✓	85
SDSS J10353+0551 [†]	5.0	13.3	3.8±2.1	0.02±0.01	0.16±0.09	197	29.1	0.8	✓	88
QZ Lib [†]	107.1	1.6	64.6±9.2	0.14±0.02	1.26±0.18	198	30.0	6.1	✓	100
LP 731-60*	131.9	2.1	52.3±7.7	0.18±0.03	1.64±0.24	109	29.6	2.4	✓	92
AL Com	20.6	7.3	14.7±4.5	0.05±0.01	0.42±0.13	621	30.5	20.2	x	44
EG Cnc*	14.0	8.8	9.4±3.5	0.05±0.02	0.42±0.16	188	29.5	1.8	✓	89
IL Leo	595.3	2.1	162.4±13.4	0.75±0.06	6.71±0.55	525	31.6	227.9	x	45
GW Lib	182.4	3.2	85.8±10.1	0.21±0.02	1.89±0.22	113	29.7	3.0	✓	58
V406 Vir [†]	83.0	0.9	36.5±6.5	0.11±0.02	1.01±0.18	171	29.8	3.6	✓	64
SDSS J12160+0520*	22.4	3.0	15.2±4.6	0.05±0.02	0.46±0.14	377	30.1	8.1	✓	100
BW Sel [†]	766.5	0.7	204.1±14.9	0.82±0.06	7.33±0.54	93	30.1	7.9	✓	82
IRXS J02323-3718*	363.3	1.7	120.6±11.6	0.25±0.02	2.26±0.22	214	30.3	12.7	✓	67
CRTS J09035+3300	53.3	4.6	25.2±5.4	0.11±0.02	0.96±0.20	331	30.3	12.9	x	39
CRTS J12222-3115 [†]	199.8	1.9	84.6±9.8	0.22±0.03	1.93±0.22	248	30.4	14.6	✓	77
GALEX J09040+0355	6.5	11.5	6.1±2.9	0.03±0.01	0.25±0.12	295	29.6	2.7	x	71
PM J12192+2049*	32.1	2.6	18.6±4.8	0.06±0.02	0.56±0.15	274	29.9	5.2	✓	81
PNV J06000+1426	19.1	4.7	12.1±3.9	0.04±0.01	0.40±0.13	911	30.8	40.5	x	-
HV Vir*	11.7	11.6	11.1±4.0	0.03±0.01	0.29±0.10	320	29.7	3.6	✓	61
PHL 1445	129.4	1.5	58.6±8.3	0.12±0.02	1.09±0.15	239	30.1	7.6	✓	67
OY Car	5833.9	0.5	1418.7±39.4	1.21±0.03	10.76±0.30	90	30.2	10.8	✓	33
XZ Eri	25.9	8.1	18.4±4.9	0.04±0.01	0.37±0.10	377	30.0	6.4	✓	43
AQ CMi	265.5	1.9	87.2±9.9	0.35±0.04	3.09±0.35	567	31.3	122.5	x	42
AQ Eri	1488.0	1.3	381.8±20.5	0.99±0.05	8.84±0.47	379	31.4	156.9	x	33
DT Pyx	12.8	0.7	9.4±3.5	0.03±0.01	0.30±0.11	336	29.8	4.1	x	43
IK Leo	14.0	1.6	11.8±4.1	0.05±0.02	0.47±0.16	766	30.7	33.9	x	94
2MASS J07341+2713	70.5	4.1	29.2±5.8	0.13±0.03	1.13±0.23	1446	31.7	291.5	x	43
SDSS J09475+0610	25.3	3.9	13.9±4.1	0.06±0.02	0.57±0.17	761	30.8	40.6	x	53
CRTS J10441+2113*	38.6	0.2	18.0±4.7	0.08±0.02	0.73±0.19	411	30.4	15.2	✓	67
CRTS J10583+0547	21.4	2.4	11.8±3.7	0.06±0.02	0.52±0.16	697	31.1	31.1	x	33
CRTS J12590+2426	7.0	6.4	6.4±3.0	0.02±0.01	0.16±0.08	646	30.1	8.3	x	58
TCP J15375-2440	17.8	5.8	15.5±4.9	0.04±0.01	0.36±0.11	-	-	-	x	-
KK Cnc	11.4	5.2	7.4±3.1	0.03±0.01	0.29±0.12	853	30.6	25.6	x	61
MM Hya	18.6	7.6	10.8±3.7	0.05±0.02	0.41±0.14	341	30.0	5.8	x	58
MM Sco	117.6	2.0	60.1±8.6	0.18±0.03	1.62±0.23	388	30.7	30.1	x	33
RX Vol	269.8	1.6	127.2±12.2	0.10±0.01	0.93±0.09	1607	31.7	297.1	x	61
RZ LMi	34.3	4.6	18.4±4.8	0.08±0.02	0.71±0.19	647	30.8	36.8	x	28
V436 Cen	2651.2	1.0	658.3±26.7	1.62±0.07	14.41±0.59	154	30.8	42.1	x	35

Table A.1. (continued)

Name	Detection likelihood	sep _{ox} ["]	Counts [cts]	Count rate [cts/s]	Flux (APEC) ×10 ⁻¹³ [erg cm ⁻² s ⁻¹]	Distance [pc]	X-ray luminosity ¹ log(L _{bol}) [erg s ⁻¹]	M _{acc} ×10 ⁻¹⁴ [M _⊙ yr ⁻¹]	Selection cuts Fig. 7	Fig. 8	Period-bouncer final score [%]
V591 Cen	15.6	6.3	13.9±4.4	0.03±0.01	0.27±0.09	1615	31.1	86.7	x	x	43
VX For	41.2	3.3	27.5±6.0	0.04±0.01	0.35±0.08	513	30.3	11.5	x	✓	67
RX J0154.0-5947	3488.2	0.9	785.3±29.1	1.80±0.07	16.04±0.59	321	31.5	203.8	x	✓	47
IRXS J06003-2709	445.8	1.6	141.6±12.6	0.34±0.03	3.05±0.27	1219	31.9	559.1	x	x	29
ASASSN -14jf	69.0	1.6	57.2±8.9	0.02±0.01	0.22±0.03	681	30.3	12.6	x	✓	60
ASASSN -17el	188.2	2.6	93.0±10.6	0.13±0.01	1.16±0.13	344	30.4	17.0	x	✓	94
CRTS J05220-3505	25.2	5.2	20.3±5.3	0.03±0.01	0.28±0.07	780	30.5	21.2	x	✓	73
V436 Cen	2651.2	1.0	658.3±26.7	1.62±0.07	14.41±0.59	154	30.8	42.1	x	✓	35
V591 Cen	15.6	6.3	13.9±4.4	0.03±0.01	0.27±0.09	1615	31.1	86.7	x	x	43
VX For	41.2	3.3	27.5±6.0	0.04±0.01	0.35±0.08	513	30.3	11.5	x	✓	67
RX J0154.0-5947	3488.2	0.9	785.3±29.1	1.80±0.07	16.04±0.59	321	31.5	203.8	x	✓	47
IRXS J06003-2709	445.8	1.6	141.6±12.6	0.34±0.03	3.05±0.27	1219	31.9	559.1	x	x	29
ASASSN -14jf	69.0	1.6	57.2±8.9	0.02±0.01	0.22±0.03	681	30.3	12.6	x	✓	60
ASASSN -17el	188.2	2.6	93.0±10.6	0.13±0.01	1.16±0.13	344	30.4	17.0	x	✓	94
CRTS J05220-3505	25.2	5.2	20.3±5.3	0.03±0.01	0.28±0.07	780	30.5	21.2	x	✓	73
OT 1112	-	7.1	-	-	-	571	-	-	-	-	94
PNV 1714	-	2.0	-	-	-	176	-	-	-	-	80
V1258 Cen	-	15.1	-	-	-	367	-	-	-	-	13
FL TrA	-	5.5	-	-	-	8651	-	-	-	-	50

¹ The X-ray luminosity refers to the bolometric band from 0.1-12 keV.[†] System is a confirmed period-bouncer.

* System has been confirmed as a new period-bouncer using eROSITA selection cuts. See Sect. 6 for a discussion of these 7 systems.

Appendix B: Abridged literature catalog table

Table B.1 gives a brief description of the columns available in the complete version of our literature catalog. Selected columns showing system parameters from the literature are given in Table B.2.

Table B.1. Content of the 66 columns in our literature catalog of period-bounce candidates, corresponding to values obtained from the literature and from photometry.

#	Name	Unit	Description
1	System		Object name more commonly used in literature.
2	GaiaDR3		<i>Gaia</i> ID from data release 3.
3	RA	deg	Right Ascension (J200).
4	DEC	deg	Declination (J200).
5	Porb	h	Orbital period of the system.
6	Mdonor_1	M_{\odot}	Donor mass.
7	Method_1		Method used to determine the donor mass: SH - Superhumps EM - Eclipse modelling RV - Radial velocity GR - Gravitational redshift SED - SED fitting
8	MassRatio_1		Indicates if the donor mass was obtained from a mass ratio
9	Mdonor_2	M_{\odot}	Donor mass.
10	Method_2		Method used to determine the donor mass.
11	MassRatio_2		Indicates if the donor mass was obtained from a mass ratio
12	SpTdonor		Donor spectral type.
13	Method		Method used to determine the donor spectral type: S - Spectroscopic P - Photometric M - Assumed from mass value
14	Distance	pc	Distance to the system from Bailer-Jones et al. (2021) .
15	T_WD	K	WD temperature.
16	M_WD	M_{\odot}	WD mass.
17	WDmagnetism		Magnetism of the WD.
18	References		Literature references for the system.
19	WISE1	mag	IR magnitude in WISE1-band.
20	e_WISE1	mag	Corresponding magnitude error in WISE1-band.
21	WISE2	mag	IR magnitude in WISE2-band.
22	e_WISE2	mag	Corresponding magnitude error in WISE2-band.
23	WISE3	mag	IR magnitude in WISE3-band.
24	e_WISE3	mag	Corresponding magnitude error in WISE3-band.
25	WISE4	mag	IR magnitude in WISE4-band.
26	e_WISE4	mag	Corresponding magnitude error in WISE4-band.
27	2MASSJ	mag	IR magnitude in 2MASS J-band.
28	e_2MASSJ	mag	Corresponding magnitude error in 2MASS J-band.
29	2MASSH	mag	IR magnitude in 2MASS H-band.
30	e_2MASSH	mag	Corresponding magnitude error in 2MASS H-band.
31	2MASSK	mag	IR magnitude in 2MASS K-band.
32	e_2MASSK	mag	Corresponding magnitude error in 2MASS K-band.
33	UKIDSSY	mag	IR magnitude in UKIDSS Y-band.
34	e_UKIDSSY	mag	Corresponding magnitude error in UKIDSS Y-band.
35	UKIDSSJ	mag	IR magnitude in UKIDSS J-band.
36	e_UKIDSSJ	mag	Corresponding magnitude error in UKIDSS J-band.
37	UKIDSSH	mag	IR magnitude in UKIDSS H-band.
38	e_UKIDSSH	mag	Corresponding magnitude error in UKIDSS H-band.
39	UKIDSSK	mag	IR magnitude in UKIDSS K-band.
40	e_UKIDSSK	mag	Corresponding magnitude error in UKIDSS K-band.
41	VHSY	mag	IR magnitude in VHS Y-band.
42	e_VHSY	mag	Corresponding magnitude error in VHS Y-band.
43	VHSJ	mag	IR magnitude in VHS J-band.
44	e_VHSJ	mag	Corresponding magnitude error in VHS J-band.
45	VHSH	mag	IR magnitude in VHS H-band.
46	e_VHSH	mag	Corresponding magnitude error in VHS H-band.

Table B.1. Content of the 66 columns in our literature catalog of period-bounce candidates, corresponding to values obtained from the literature and from photometry.

#	Name	Unit	Description
47	VHSKs	mag	IR magnitude in VHS Ks-band.
48	e_VHSKs	mag	Corresponding magnitude error in VHS Ks-band.
49	GaiaG	mag	Optical magnitude in <i>Gaia</i> G-band.
50	e_GaiaG	mag	Corresponding magnitude error in <i>Gaia</i> G-band.
51	GaiaBP	mag	Optical magnitude in <i>Gaia</i> BP-band.
52	e_GaiaBP	mag	Corresponding magnitude error in <i>Gaia</i> BP-band.
53	GaiaRP	mag	Optical magnitude in <i>Gaia</i> RP-band.
54	e_GaiaRP	mag	Corresponding magnitude error in <i>Gaia</i> RP-band.
55	SDSSu	mag	Optical magnitude in SDSS u-band.
56	e_SDSSu	mag	Corresponding magnitude error in SDSS u-band.
57	SDSSg	mag	Optical magnitude in SDSS g-band.
58	e_SDSSg	mag	Corresponding magnitude error in SDSS g-band.
59	SDSSr	mag	Optical magnitude in SDSS r-band.
60	e_SDSSr	mag	Corresponding magnitude error in SDSS r-band.
61	SDSSi	mag	Optical magnitude in SDSS i-band.
62	e_SDSSi	mag	Corresponding magnitude error in SDSS i-band.
63	SDSSz	mag	Optical magnitude in SDSS z-band.
64	e_SDSSz	mag	Corresponding magnitude error in SDSS z-band.
65	GALEXFUV	mag	UV magnitude in GALEX FUV-band.
66	e_GALEXFUV	mag	Corresponding magnitude error in GALEX FUV-band.
67	GALEXNUV	mag	UV magnitude in GALEX NUV-band.
68	e_GALEXNUV	mag	Corresponding magnitude error in GALEX NUV-band.

Table B.2. Shortened version of our period-bounce candidates catalog showing relevant properties of the systems.

System	P_{orb} [h]	M_{donor} [M_{\odot}]	SpT _{donor}	Distance [pc]	WD T_{eff} [K]	M_{WD} [M_{\odot}]	WD type	References
V379 Vir	1.47	0.050	L8	153	10000	0.64	Magnetic	1, 2, 3, 4, 5
SDSS J151415.65+074446.4	1.47	0.082	L3	182	10000	0.80	Magnetic	3, 6
PM J12507+1549	1.44	0.077	M8	131	10000	0.64	Magnetic	6, 3
EF Eri	1.35	0.083	Not late	160	10000	0.90	Magnetic	7, 8
SDSS J105754.25+275947.5	1.51	0.044	L5	355	11500	0.83	Non-magnetic	9, 10
⋮	⋮	⋮	⋮	⋮	⋮	⋮	⋮	⋮

References. (1) Stelzer et al. (2017), (2) Burleigh et al. (2006), (3) Muñoz-Giraldo et al. (2023), (4) Kruckow et al. (2021), (5) Farihi et al. (2008), (6) Breedt et al. (2012), (7) Schwöpe & Christensen (2010), (8) Howell et al. (2006), (9) McAllister et al. (2017), (10) Echevarría et al. (2023).

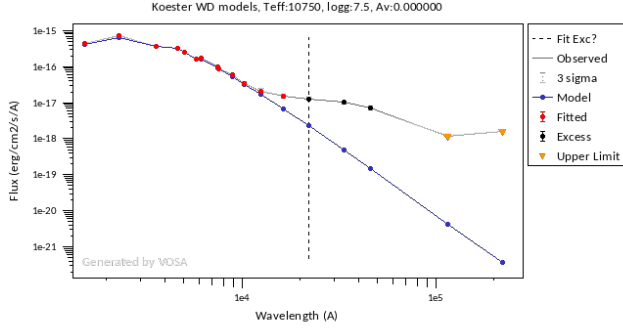


Fig. C.1. WD fit to the SED of V379 Vir. VOSA marks the excess starting at *K*-band.

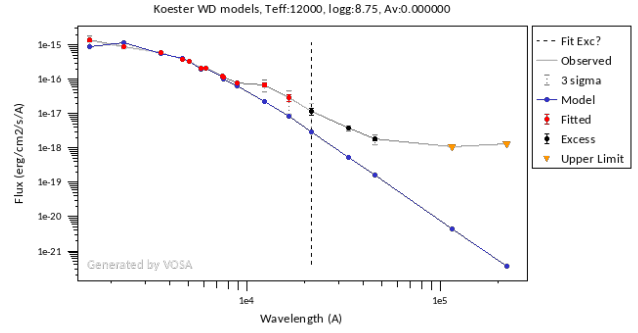


Fig. C.2. WD fit to the SED of V406 Vir. VOSA marks the excess starting at *K*-band.

Appendix C: Examples for SED types

We define 3 typical cases for SEDs of pre-bounce CVs, CVs at the period minimum and post-bounce CVs with the following criteria: excess setting in at wavelengths shorter than 12483\AA (*J*-band) for CVs before the period-bounce, excess setting in at wavelengths between 12483\AA and 22010\AA (*K*-band) for CVs around the period-bounce, and excess setting in at wavelengths longer than 22010\AA for CVs significantly after the period-bounce.

To determine the onset wavelength of the excess in the SED we used VOSA, where we fitted a WD model (Koester 2010) to the SED of each period-bounce candidate in our literature catalog initially giving as input a range of $\pm 1000\text{ K}$ around the WD temperature found in the literature. When necessary, we adjusted the temperature range to obtain a better fit specifically for the GALEX points considering that it is in the UV bands where we get the best constraints on the WD. The final WD temperature and $\log(g)$ values used in the fit are reported in the top part of each figure. We did not consider extinction. VOSA suggests a point for the beginning of the excess (vertical dashed line in Figs. C.1, C.2, C.3 and C.4) which, in most cases, we used to assign the corresponding points in our scorecard. There were a few cases (see Fig. C.4) where it was clear that the excess starts at a shorter wavelength, in which case we selected ourselves the shorter band as the point of beginning of the excess.

We use 4 different systems from our catalog to illustrate different SED cases. V379 Vir (Fig. C.1), with an excess starting at the *K*-band, is a confirmed magnetic period-bouncer with a spectroscopically detected L8 donor (Farihi et al. 2008). V406 Vir (Fig. C.2), with an excess starting at the *K*-band, is a confirmed non-magnetic period-bouncer with a spectroscopically detected L3 donor (Pala et al. 2019). CRTS J122221.6-311525 (Fig. C.3), with an excess starting at the WISE1-band, is a confirmed non-magnetic period-bouncer with a photometrically detected L0 donor (Neustroev et al. 2017). EF Eri is an already confirmed pre-bounce magnetic system with an excess starting in the *J*-band (Fig. C.4).

Magnetic systems, like V379 Vir and EF Eri, are expected to present cyclotron humps (Wickramasinghe 1988). From comparing Figs C.1 and C.2, a clear increased emission between 21000\AA and 46000\AA can be observed in the SED of V379 Vir most likely due to cyclotron humps. However, even when considering this additional feature, the IR excess in V379 Vir still starts at the *K*-band as expected for period-bouncers. EF Eri, a known magnetic pre-bounce systems, also presents cyclotron humps in the SED but associated with shorter wavelengths that lead to IR

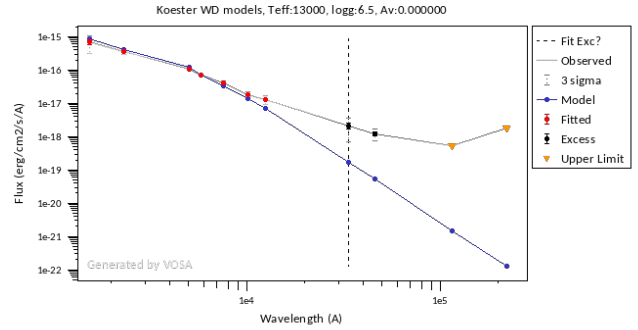


Fig. C.3. WD fit to the SED of CRTS J122221.6-311525. VOSA marks the excess starting at WISE 1 band.

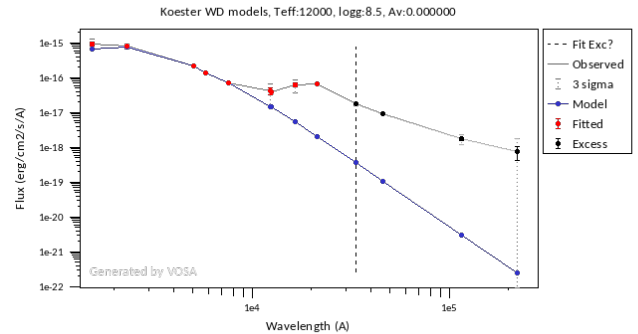


Fig. C.4. WD fit to the SED of EF Eri. VOSA marks the excess starting at WISE 1 band, but it is clear to us that it starts at *J*-band.

excess starting at *J*-band, marking the system as not a period-bouncer.